NTNU – Trondheim
Norwegian University of
Science and Technology

Optical Properties of Silicon Microwire Arrays for Photovoltaic Applications

Benjamin Smeltzer

MSc in Physics
Submission date: May 2015
Supervisor: Ursula Gibson, IFY

Norwegian University of Science and Technology
Department of Physics

Optical Properties of Silicon Microwire Arrays for Photovoltaic Applications

Benjamin K. Smeltzer

May 15, 2015

Abstract

Silicon microwire-based solar cells represent a potential design strategy to reduce wafer related costs through reduced material usage and relaxed purity requirements. In this work we investigate the absorption of incident solar radiation achievable in two designs using microwires produced from a molten core fiber drawing method. The first consists of vertically aligned wires each surrounded by an etched conical cavity that served as a light trapping structure, while the second consists of horizontally-aligned wires on a substrate. Modeling explored the absorption of both designs as a function of various geometrical and optical parameters relevant to cell design, while experimental absorption measurements were conducted on horizontal arrays using a home-built integrating sphere setup. The results demonstrated over 70% absorption of the solar spectrum in both these designs despite reduced silicon per unit cell area and without anti-reflection coatings. The results highlight the potential of silicon microwire-based solar cells to reduce costs while maintaining high absorption, as well as other potential uses as semi-transparent cells in the case of the horizontal design.

Preface

This work was conducted at the Department of Physics at the Norwegian University of Science and Technology (NTNU) during the Fall of 2014 and Spring of 2015 for the partial fulfillment of a masters degree in Physics. The project was carried out under the supervision of Professor Ursula Gibson.

In addition to the results presented here, the results of the project contributed to one publication as well as another manuscript to be submitted (included in appendices):

- F. A. Martinsen, B. K. Smeltzer, M. Nord, T. Hawkins, J. Ballato, & U. J. Gibson. Silicon-core glass fibers as microwire radial-junction solar cells. Sci. Rep., 4:6283, 2014.

- F. A. Martinsen, B. K. Smeltzer, J. Ballato, T. Hawkins, M. Jones, & U. J. Gibson. Horizontally aligned silicon microwires as solar cells. *To be submitted.*

Optical ray tracing code in 2D and 3D was written in MATLAB (included in Appendix C), and can be supplied to any interested users upon request. Although the code was designed with the structures in this work in mind, the inputs allow generalization to a wide range of geometries and materials.

I would like to thank the many people who have assisted me along the way during the completion of this work. First and foremost my advisor Prof. Ursula Gibson for her support and guidance and many fruitful ideas. In addition, I would like to

thank Fredrik Martinsen, Eric Karhu, and David Coucheron for experimental help and many useful discussions. I would also like to thank the NTNU glass shop and machine shop for producing components used in the experimental setup, as well as the NTNU Nanolab staff. Last but not least, I would like to thanks my family for their love and support.

Contents

Abstract **ii**

Preface **iv**

1 Introduction **1**

1.1 Global energy perspective 1

1.2 Overview of photovoltaic technology 3

1.3 Silicon microwires 5

1.4 Overview 7

2 Background **9**

2.1 Solar cell physics 9

2.2 Interaction of light with dielectric media 13

2.2.1 Absorption 15

2.2.2 Reflection and Transmission 15

2.2.3 Ray optics 17

2.2.4 Specular and Lambertian surfaces 18

2.2.5 Intensity Enhancement 19

2.3 Silicon optical properties 20

2.3.1 Techniques for increasing Si absorption 21

2.4 Radial junction solar cells 23

2.5 Absorption Measurements 26

2.5.1 Integrating sphere theory and design 27

2.5.2 Monochomator theory 30
2.5.3 Photodetector theory 31
2.5.4 Lock-in amplifier theory 32

3 Methods **35**
3.1 Modeling 35
3.1.1 Ray Tracing code 35
3.1.2 Statistical ray model 42
3.1.3 Gee model 45
3.2 Experiments 47
3.2.1 Assembly of horizontally aligned microwire array samples . . . 47
3.2.2 Experimental setup for absorption measurements 49

4 Results and Discussion **57**
4.1 Forest geometry with light-trapping cone 57
4.1.1 Cone angle and reflectivity scalings 59
4.1.2 Wire diameter and fill fraction 62
4.1.3 Wavelength dependence 63
4.1.4 Angle of incidence 67
4.1.5 Discussion 69
4.2 Horizontally Aligned Si Microwires 70
4.2.1 Modeling 71
4.2.2 Experimental Measurements 76
4.2.3 Specular backreflector 77
4.2.4 Lambertian backreflector 80
4.2.5 No backreflector 82
4.2.6 Performance across the solar spectrum 83
4.2.7 Discussion 85
4.3 General Discussion 86

Further Work **87**

Conclusion **88**

Bibliography **91**

Appendix A: Paper 1 **95**

Appendix B: Paper 2 **105**

Appendix C: Ray Tracing MATLAB Code **111**

Chapter 1

Introduction

1.1 Global energy perspective

Supplying the growing global energy demand is likely to be an outstanding challenge in the coming decades. The world consumption of energy has been predicted to rise 56% between 2010 and 2040, largely due to economic growth. [1] Currently, much of this demand is met by fossil fuels which emit carbon dioxide into the atmosphere. [1] Increasingly overwhelming scientific evidence linking fossil fuel emissions to climate change as well as their finite supply motivates a search for alternative renewable energy sources that are replenished during human timescales, as well as being less harmful to the environment and climate of the earth. Much of the global supply of non-renewable sources could be exhausted within the next 100 years given current consumption of ≈ 16 Terawatt-yr per year if the estimates in Fig. 1.1 are accurate. [2] Research and development of renewable energy sources are thus vital to meeting the long-term global energy demands, as well as combating climate change by replacing fossil fuel sources.

One of the most attractive and promising renewable energy sources is solar energy. Sunlight incident on the earth's surface represents by far the largest potential energy source as shown in Fig. 1.1, with approximately 10,000 times the current global energy consumption incident on the earth each year. [2] Despite the vast

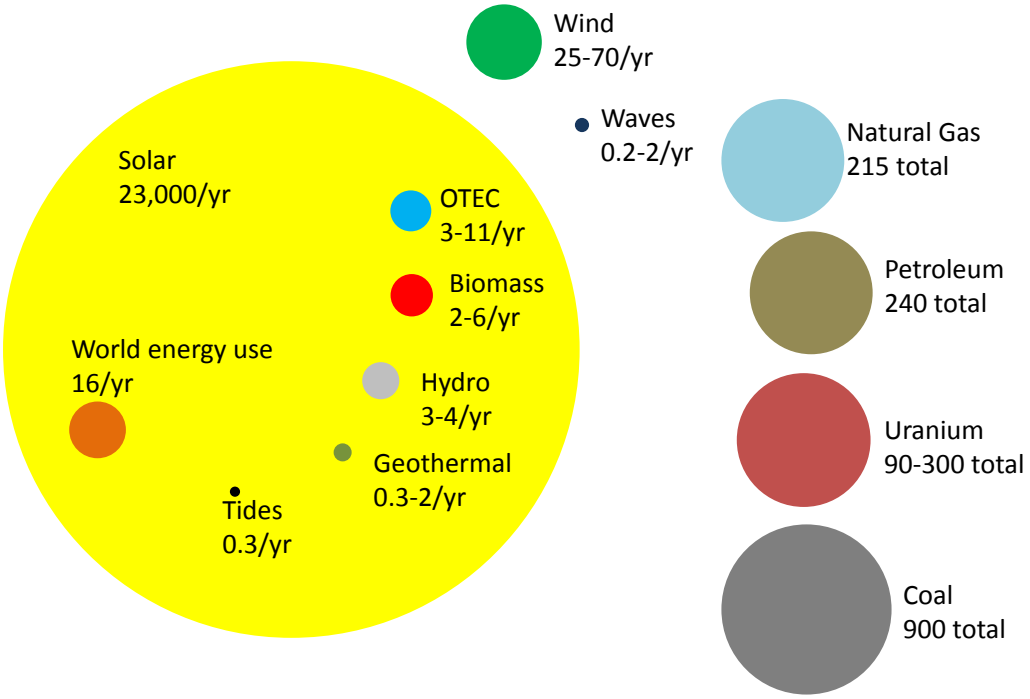

Figure 1.1: A comparison of the supply of potential energy sources. All units are Terawatt-years. The supply of renewable sources is expressed per year, while for fixed supply sources the estimated total reserve is given. Adapted from [2].

amount of solar energy supplied to the earth, widespread deployment of systems to harness solar energy remain limited. Photovoltaic (or solar cell) technology, which harnesses energy from the sun by absorbing solar photons and transferring this energy to an electrical circuit, remains expensive and relatively inefficient. However, advances in the manufacture of photovoltaic systems have reduced the price per unit of power ($/Watt), and the deployment of systems has experienced notable recent growth. Solar technology is one of most rapidly growing energy sources as seen in Fig. 1.2, yet continued research is vital in the quest to further reduce the ($/Watt) value and increase its widespread use to meet energy demands. [3] [4]

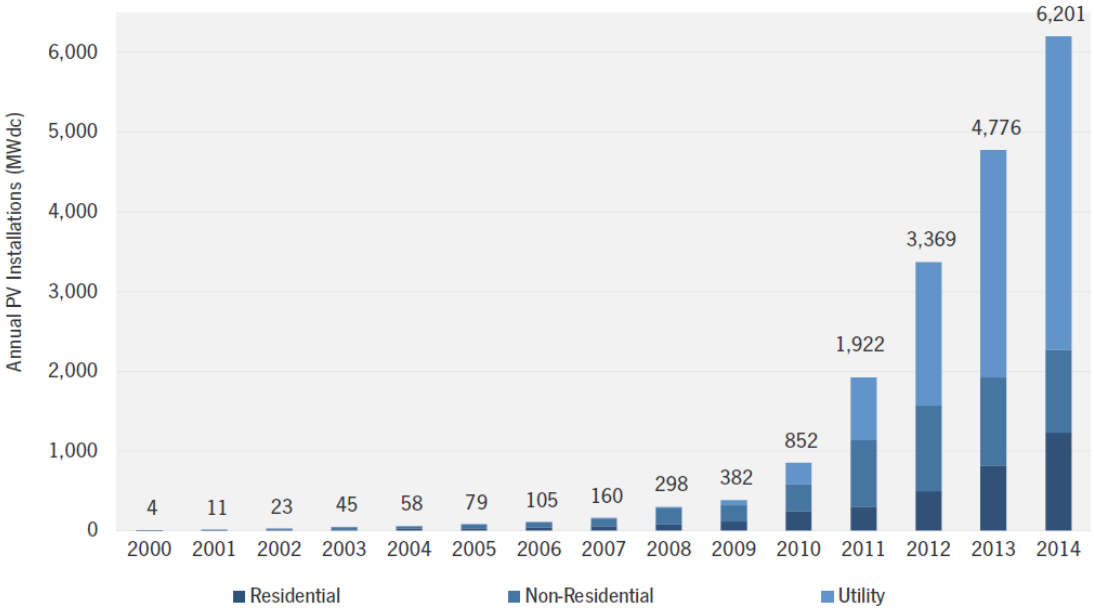

Figure 1.2: The number of annual photovoltaic installations in the US from 2000 to 2014. Taken from [5]

1.2 Overview of photovoltaic technology

Though there are many potential materials for photovoltaic systems, crystalline silicon-based technology has dominated the industry for the last decades, and has several notable advantages which contribute to its current success. Crystalline silicon has benefited from the uses of silicon in the electronics industry, where the purification and crystallization of silicon has a long-established research base. In addition, manufactured modules are robust having long lifetimes and silicon raw material is scalable to meeting large-scale energy demands due to its non-toxicity and supply as the second most abundant element on the earth. [6] [7] [4]

Despite these advantages, crystalline silicon systems are costly. There are many components that influence the total system cost which can be divided into three main areas: the wafer, cell, and module as shown in Fig. 1.3. [4] Wafer costs include crystallization and purification processes, and material losses from wafer sawing (kerf

loss) and breakage, especially as the material thickness is decreased. Cell and module related costs include the processing and packaging to produce the final system.

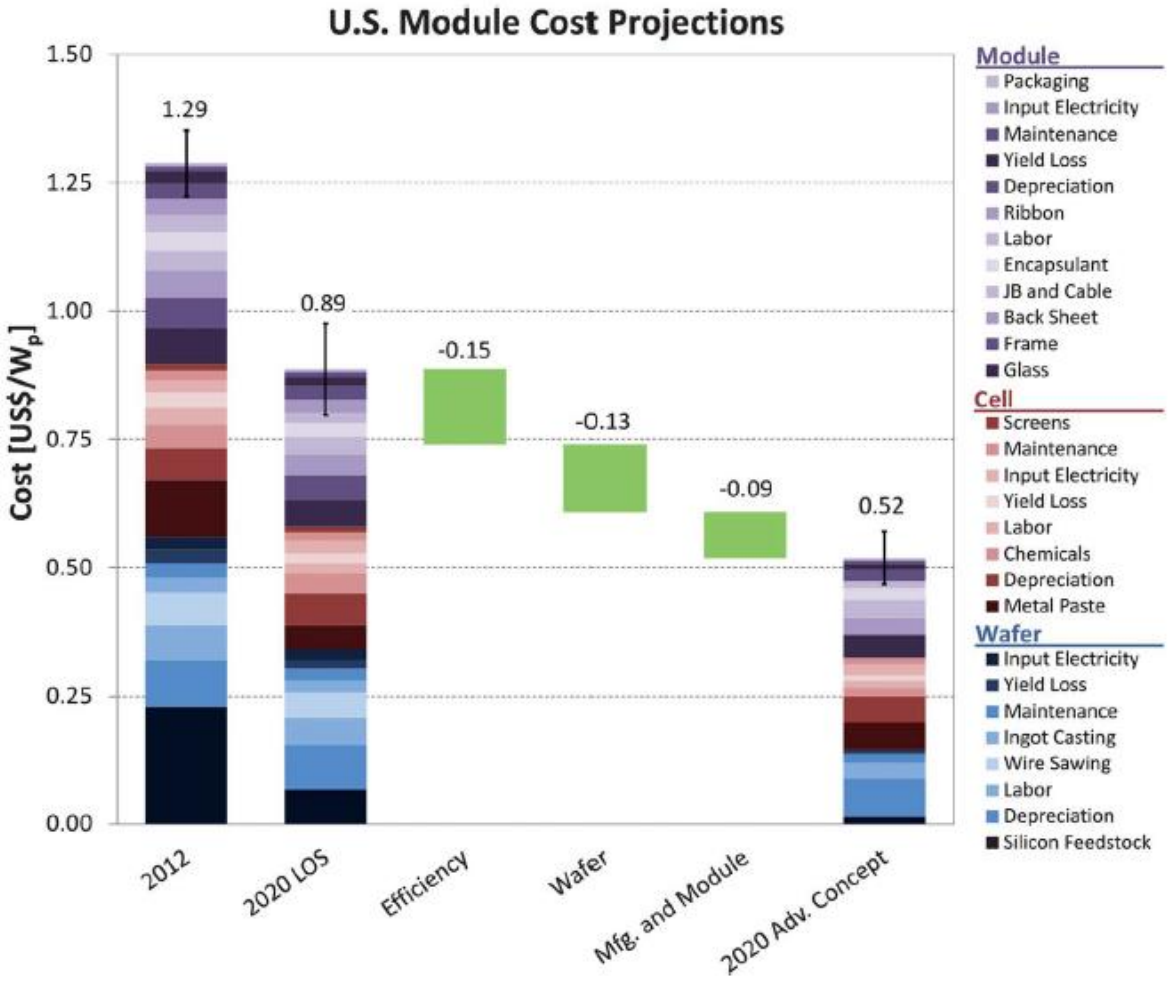

Figure 1.3: Cost estimates of the different components to crystalline silicon modules. Taken from [4]

The high cost of crystalline silicon cells has spurred research into thin film technologies which aim to drastically reduce the cell cost. This has resulted in a wide range of cheaper alternative technologies that have gained a share of the market, yet they suffer lower efficiency which has limited their use. However, there are potential applications for less-efficient yet semi-transparent cells for deployment on for example windows. Despite the drop in efficiency, these systems could be implemented on

structures where a large fraction of the surface area consisted of windows such as office buildings.

Another research area aims to increase the efficiency compared to what is achievable with silicon based cells through advanced technologies. This includes tandem and intermediate band cells that utilize multiple energy band gaps to better harness the solar radiation at different energies, as well as advanced strategies to circumvent fundamental efficiency limits. Record efficiencies have been demonstrated with this research, yet the cells are extremely costly limiting them to niche applications at the present time.

Though there are many exciting potential photovoltaic materials that could be the long-term future of the industry, it is likely that silicon will dominate in the near-term, and continued research efforts in silicon photovoltaics are of relevance. These efforts aim to reduce the costs while maintaining or improving the efficiency. While research into cost reductions in all areas of the device production process are important, we will focus here on wafer-related costs which account for a significant component (30-50%) of the total module cost. In decreasing these costs, two main strategies have been proposed by Powell *et al.* [4]: achieving high efficiencies with thinner wafers, and better material utilization by reducing losses. The research conducted in this work is aimed at addressing both these points by using a novel alternative to conventional wafers: silicon microwires.

1.3 Silicon microwires

Silicon mircowire-based photovoltaic structures represent a potential innovative and alternative strategy towards achieving the two goals mentioned above. Microwires consist of cylindrical sections of crystalline silicon typically arranged in a planar based array. These structures have the potential to realize high effiencies while reducing costs by relaxing material purity requirements, decreasing the volume of silicon required per unit device area, and reducing material losses during production among potential other factors. Silicon microwires (and smaller diameter nanowires)

have been the subject of an extensive body of research to date which will be summarized in the next chapter. One of the most important research areas involves strategies to maximize the absorption of solar radiation in these structures, a vital property in any high-performance solar cell as imperfect absorption results in a proportionate efficiency drop. In this work we investigate the optical absorption achievable in silicon microwire arrays from wires produced through the novel technique of molten-core fiber drawing. [8] [9] [10] This technique produces long segments of cylindrical silicon wire cores surrounded by a silica cladding layer. We investigate two general design approaches for assembling photovoltaic cells from these segments shown in Fig. 1.4.

The first arrangement consists of vertically aligned microwires surrounded by a conical-shaped cavity as shown in Fig. 1.4 a-b.). The formation of the cavity was observed during etching of wire segments in hydrogen fluoride (HF), and is likely due to rapid etching in an interfacial calcium oxide layer between the wire cores and the silica cladding. [10] The discovery of this cavity prompted the idea for this design, as solar radiation not directly incident on the wire top surfaces could be directed into the wires through reflections from this cone structure (Fig. 1.4 b.). Reduced silicon material could be utilized (effectively equivalent to decreasing wafer thickness) while potentially maintaining strong optical absorption.

The second arrangement consists of horizontally aligned microwires placed on a substrate as shown in Fig. 1.4 c.). This design does not have inherent light-directing surfaces such as the conical cavity, and gaps between wire elements could directly translate into absorption and thus efficiency losses. To improve the absorption, the design could involve mounting the wires on a backreflector and embedding them in a dielectric medium to increase the trapping of light rays in the structure. Though high optical absorption may be more challenging with this structure, the horizontal alignment largely avoids kerf loss due to sawing. This structure could also function as a semi-transparent cell applicable to installations where lower efficiency is acceptable. Tunable transparency could be achieved by controlling the center-to-center distance between adjacent wire segments.

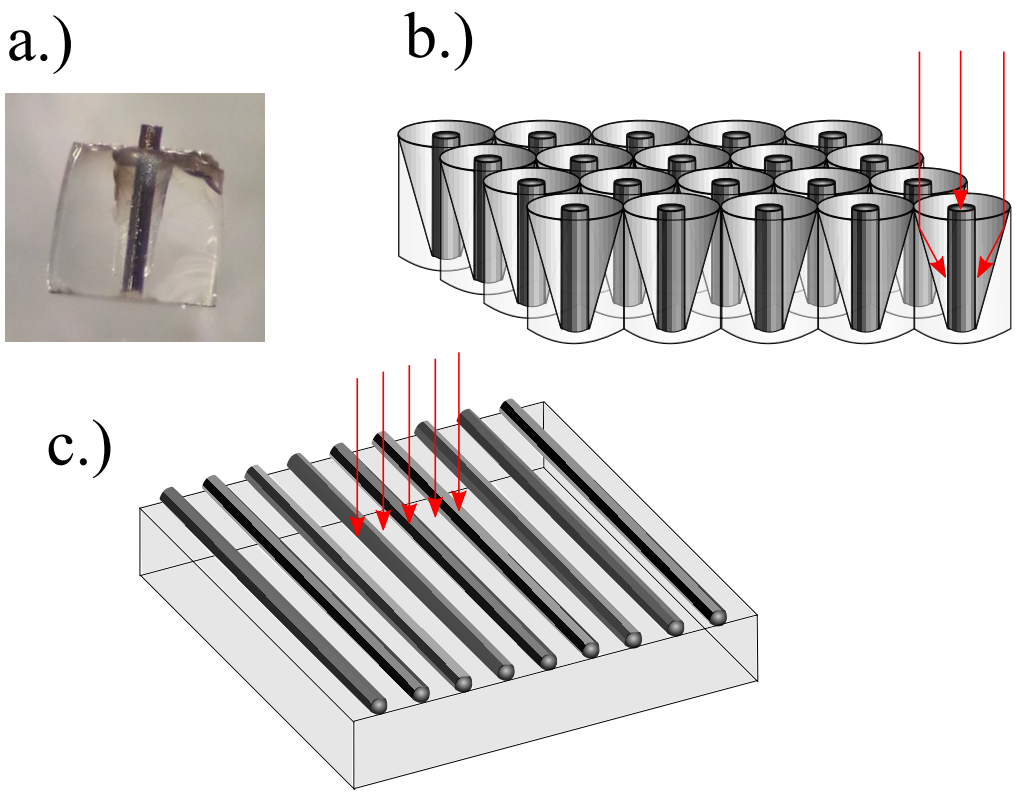

Figure 1.4: a.) An image of a segment of a silica-clad silicon microwire after HF, showing the conical cavity. b.) A schematic of an array of vertically aligned microwires with conical cavities acting to direct incident light into the wires. c.) Horizontally-aligned microwire array.

1.4 Overview

The work presented here aims to investigate the degree of optical absorption in these structures. As the solar cell efficiency scales directly with the fraction of absorbed solar radiation, maximization of the absorption is an important part of any solar cell design. The absorption potential of the two microwire designs mentioned above were evaluated through both modeling and experimental techniques. The modeling efforts included ray optics code written in MATLAB as well as several analytic techniques applied both designs. Experimental absorption measurements on hori-

zontally aligned array samples were conducted to validate and confirm the general accuracy of the models. Before presenting and discussing these results (chapter 4), necessary background information is provided (chapter 2), and the modeling and experimental techniques are described in detail (chapter 3).

Chapter 2

Background

Relevant background information and theory are presented in this chapter. The first part reviews relevant theory including the basic physics of solar cells and the interaction of electromagnetic radiation and matter, followed by a review of techniques for optimizing optical absorption in silicon as well as previous work specific to silicon wire arrays. The last part of the chapter reviews theory specific to the experimental setup for absorption measurements.

2.1 Solar cell physics

Absorbing incident solar radiation is only one important component to an efficient working solar cell. It is important to consider design strategies to maximize absorption in the context of a working solar cell as a whole, which warrants a review of basic solar cell physics. The basic principle of solar cell operation involves converting energy from light, or photons, into electrical energy. Solar photons are distributed over a wide range of wavelengths as shown in Fig. 2.1. The process involves absorption of the energy from photons, which create charge carriers by exciting electrons up to a higher energy state where they are free to be collected by an external circuit. A silicon solar cell consists of a p-n junction structure as shown in Fig. 2.2. Photon absorption induces a light-generated current as minority charge carriers diffuse to the junction and then pass through the electrodes to contribute to the current.

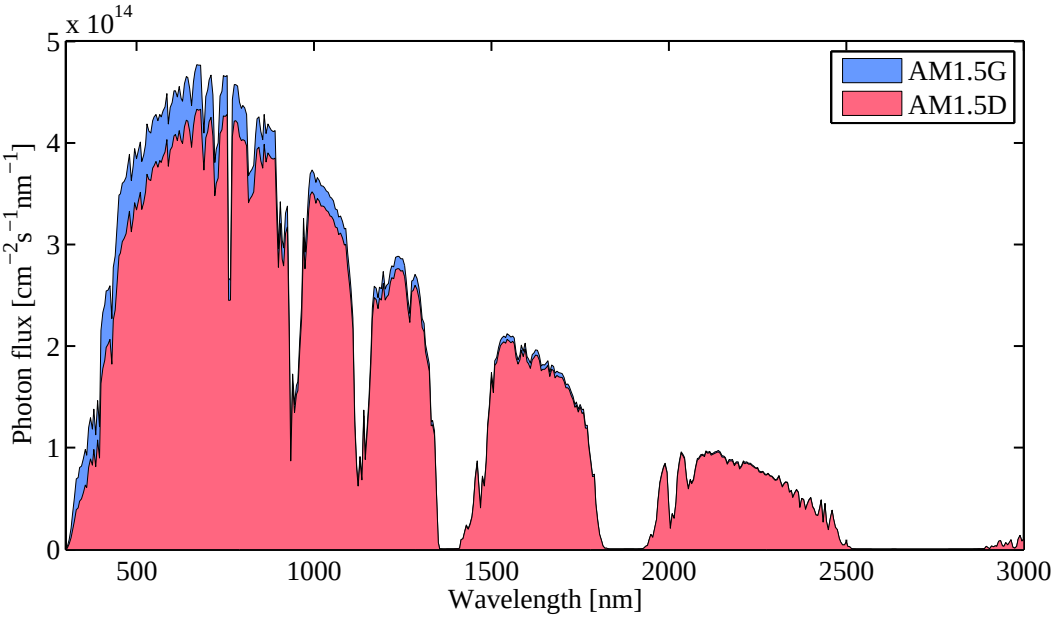

Figure 2.1: The solar photon flux. [11] The two spectra shown are the commonly used air mass 1.5 global (AM1.5G) and direct (AM1.5D) spectra. The air mass 1.5 refers to a standard the sun line-of-sight path is 1.5X longer than the normal direction (sun directly overhead). The AM1.5G spectrum includes radiation over all incident angles while the AM1.5D only includes the component from the direct line-of-sight path to the sun. [7]

When connected to an external load, a photovoltage is generated.

The simplified current-voltage characteristics of a solar cell is given as: [7]

$$J(V) = J_{\text{sc}} - J_0 \left(\exp \left[qV/mk_BT \right] - 1 \right), \tag{2.1}$$

where $J(V)$, J_{sc}, and J_0 are the net, short-circuit, and diode current densities respectively, V is the bias voltage, q is the electron charge, m is an ideality factor, k_B is Boltzmann's constant, and T is the temperature. The two terms on the right hand side of Eq. 2.1 represent the two contributions to the current. The short-circuit current (the resulting current under zero bias) is the result of incident light: photon absorption exciting charge carriers which are collected by the circuit. This

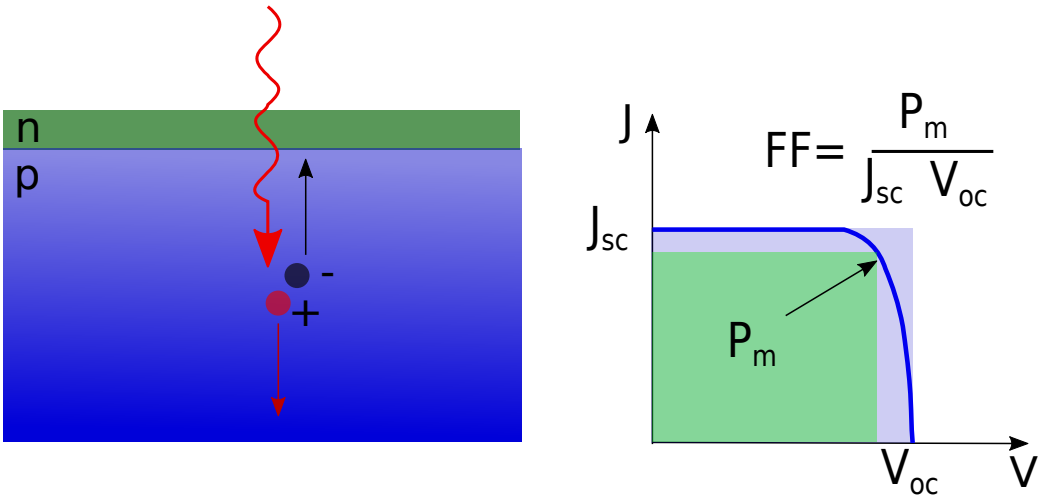

Figure 2.2: A schematic of the working principles of a solar cell, as well as the current-voltage characteristics, defining the relevant performance parameters.

light-generated current can be conveniently expressed as:

$$J_{sc} = q \int \phi_s(E) EQE(E) dE, \tag{2.2}$$

where $\phi_s(E)$ is the photon flux density at photon energy E, and $EQE(E)$ is the average number of carriers delivered to the circuit per incident photon, termed the external quantum efficiency. Eq. 2.2 can also be written as a function of photon wavelength λ using Plank's constant h, and the speed of light c:

$$E = hc/\lambda.$$

The external quantum efficiency both reflects the probability for photon absorption, as well as the probability the excited carrier will be collected by the circuit. A similar quantity known as the internal quantum efficiency (IQE) reflects only the collection probability, normalized to absorbed photons. The IQE is influenced by the rates of recombination processes, such as recombination due to impurity-related trap states, or recombination at surfaces (a particularly relevant concern for microwire devices). In general, both the EQE and IQE are influenced by the device thickness. From Eq. 2.13 we know the absorption is a function of the device thickess. The

carrier collection probability is also a function of material thickness, as generated carriers can be considered to diffuse a mean distance L_D before recombining. [7] This diffusion length is generally a function of material purity, with reduced values for increasing impure materials. Increasing the device thickness generally results in higher absorption yet reduced carrier collection efficiency as carriers generated greater than a distance L_D from the junction generally recombine and are lost to contributing to the device current.

The second term on the right side of Eq. 2.1 is often called the dark current, representing the current-voltage characteristics with no incident light. In this case, a solar cell tends to exhibit a diode behavior, with exponentially increasing current under forward bias across the junction. There are in general multiple terms that contribute to the dark current (such as minority carrier diffusion across the junction, or carrier recombination in the depletion region).

Eq. 2.1 can be re-arranged and written as in terms of an open-circuit voltage V_{oc} where no current passes through the device:

$$V_{\mathrm{oc}} = \frac{mk_BT}{q} \ln\left[\frac{J_{\mathrm{sc}}}{J_0} + 1\right]. \tag{2.3}$$

The open circuit voltage is dependent heavily on the dark current, and is thus influenced by the amount of recombination in the device.

The efficiency η of a solar cell is defined as the maximum power operation point of the I-V curve relative to the power of the incident radiation:

$$\eta = \frac{J_{\mathrm{sc}}V_{\mathrm{oc}}FF}{I_{\mathrm{solar}}}, \tag{2.4}$$

where I_{solar} is the power per unit area of the incoming solar radiation, and FF is the fill factor as defined in Fig. 2.2.

In general, the bandgap of the solar cell device influences both the short circuit current and the open circuit voltage. Smaller bandgaps allow higher fractional absorption since more photons have energies above the bandgap, yet reduced bandgaps lead to lower open-circuit voltages since qV_{oc} is less than the bandgap. Considering

un-concentrated solar radiation, the optimal bandgap for a single junction device is 1.4 eV. [7]

2.2 Interaction of light with dielectric media

Optical absorption involves coupling incident radiation into the material where the absorption process can occur. This warrants a brief review of the interaction of electromagnetic radiation and dielectric media, specifically related to the classes of media relevant to this work (for example silicon and silica). We start by stating Maxwell's equations in a source-free medium:

$$\nabla \times \mathbf{H} = \frac{\partial \mathbf{D}}{\partial t},$$

$$\nabla \times \mathbf{E} = -\frac{\partial \mathbf{B}}{\partial t},$$

$$\nabla \cdot \mathbf{D} = 0,$$

$$\nabla \cdot \mathbf{B} = 0.$$

E and **H** are the electric and magnetic fields, and **D** and **B** are the electric and magnetic flux densities respectively. Considering a non-magnetic, linear, homogeneous medium (a good assumption for the materials studied here), the flux densities can be expressed as a function of their respective fields as: [12]

$$\mathbf{D} = \epsilon \mathbf{E},$$

$$\mathbf{B} = \mu_0 \mathbf{H},$$

where ϵ and μ_0 are the medium permittivity and free-space permeability respectively. The permittivity can be expressed as a function of free-space permittivity ϵ_0:

$$\epsilon = \epsilon_0(1 + \tilde{\chi}), \tag{2.5}$$

where $\tilde{\chi}$ is the complex electric susceptibility. The refractive index, n, in this case is:

$$\tilde{n} \equiv \sqrt{1 + \tilde{\chi}}.$$

The refractive index is in general complex, with the imaginary component describing the absorption in the medium.

For the purposes of this work, we consider a monochromatic plane wave with the electric and magnetic fields defined as:

$$\mathbf{E}(\mathbf{r},t) = \mathbf{E_0}\exp\left(i\left[\mathbf{k}\cdot\mathbf{r}-\omega t\right]\right), \tag{2.6a}$$

$$\mathbf{H}(\mathbf{r},t) = \mathbf{H_0}\exp\left(i\left[\mathbf{k}\cdot\mathbf{r}-\omega t\right]\right), \tag{2.6b}$$

where $\mathbf{E_0}$ and $\mathbf{H_0}$ are the magnitudes of the electric and magnetic fields (independent of position $\mathbf{r}$), $\mathbf{k}$ is known as the wavevector, and ω is the frequency. Using the vector formula $\nabla\times(V\mathbf{A}) = \nabla V\times\mathbf{A} + V\nabla\times\mathbf{A}$ (for scalar field V and vector field $\mathbf{A}$), inserting Eq. 2.6 into Maxwell's equations yield:

$$\mathbf{k}\times\mathbf{E_0} = \omega\mu\mathbf{H_0}, \tag{2.7a}$$

$$\mathbf{k}\times\mathbf{H_0} = -\omega\epsilon_0(1+\tilde{\chi})\mathbf{E_0}. \tag{2.7b}$$

From these two equations, one can see that $\mathbf{E_0}$, $\mathbf{H_0}$, and $\mathbf{k}$ are mutually perpendicular. Furthermore, it can be shown:

$$|\mathbf{k}| = \omega\tilde{n}/c_0, \tag{2.8}$$

where $c_0 \equiv 1/\sqrt{\mu_0\epsilon_0}$ is the speed of light in vacuum. The flow of power for an electromagnetic wave is described by the complex Poynting vector: [12]

$$\mathbf{S} = \frac{1}{2}\mathbf{E}\times\mathbf{H}^*. \tag{2.9}$$

It is readily apparent that $\mathbf{S}\parallel\mathbf{k}$, thus the direction of the wavevector $\mathbf{k}$ indicates the direction of wave propagation, or energy flow. The magnitude of optical power per unit area (commonly termed intensity I) can be expressed as:

$$I = |\mathbf{E_0}|^2/2\eta, \tag{2.10}$$

where is $\eta \equiv \sqrt{\mu_0/\epsilon}$ is known as the impedance. It is important to note that $I\propto$ is proportional to the magnitude of the electric field squared. [12]

2.2.1 Absorption

As mentioned above, the imaginary component of the refractive index describes the absorption in a medium. It is useful to express the complex refractive index in terms of the real and imaginary components:

$$\tilde{n} = n + i\kappa, \tag{2.11}$$

where n and κ are real quantities. If we assume for simplicity that $\mathbf{k}$ points in the z-direction, the equation for the electric field of a monochomatic plane wave (Eq. 2.6) can be expressed using Eq. 2.8 as

$$\mathbf{E}(z,t) = \mathbf{E_0} \exp\left(-k_0\kappa + i\left[k_0 n z - \omega t\right]\right), \tag{2.12}$$

where $k_0 \equiv \omega/c_0$. Furthermore, the optical intensity can be expressed as:

$$I(z) = I_0 \exp(-2k_0\kappa z) = I_0 \exp(-\alpha z), \tag{2.13}$$

where $I_0 \equiv |\mathbf{E_0}|^2/2\eta$, and $\alpha \equiv 2k_0\kappa$. The quantity $\alpha \propto \kappa$ is known as the absorption coefficient. Eq. 2.13 is also known as Beer's law, which describes the attenuation of a plane wave propagating in a homogeneous absorbing medium. [13]

2.2.2 Reflection and Transmission

We now consider the interaction of a plane wave propagating in a medium with refractive index $\tilde{n}_1$ which is incident on a planar boundary with a second medium with refractive index $\tilde{n}_2$. This gives rise to a reflected wave with wavevector $\mathbf{k_r}$ and a wave that is transmitted into the medium, with wavevector $\mathbf{k_t}$. This is shown in Fig. 2.3.

Maxwell's equations require that the tangential components of $\mathbf{E}$ and $\mathbf{H}$ are continuous across the boundary surface. The wavevector describes the spatial propagation and variation of a plane wave, and based on these boundary conditions the following relations must hold: [14]

$$\mathbf{n} \times \mathbf{k_i} = \mathbf{n} \times \mathbf{k_r} = \mathbf{n} \times \mathbf{k_t}, \tag{2.14}$$

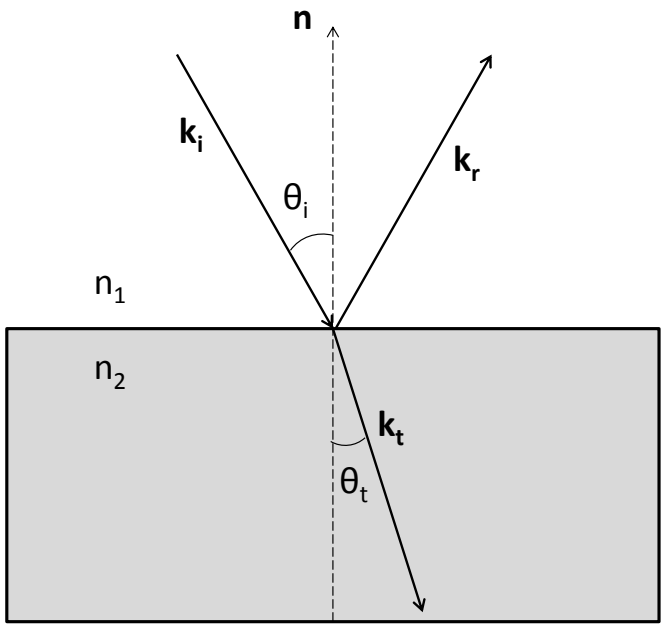

Figure 2.3: The incident, reflected, and tranmitted waves from an incident plane wave on a planar boundary between two media. **n** denotes the normal vector to the boundary surface.

where **n** is the normal vector to the boundary surface. Eq. 2.14 defines the angles of the reflected and transmitted waves relative to **n** as a function of the angle of the incident wave:

$$\theta_r = \theta_i, \tag{2.15a}$$

$$\tilde{n}_1 \sin\theta_i = \tilde{n}_2 \sin\theta_t, \tag{2.15b}$$

The first requires the angle of reflection to be the same as the angle of incidence, and the second, Eq. 2.15b, is known as Snell's law.

The boundary conditions imposed by Maxwell's equations also determine the relative magnitudes of the fields for the reflected and transmitted components, denoted r and t respectively. In this case, one must consider two orientations of $\mathbf{E_0}$ and $\mathbf{H_0}$ (polarizations) relative to the boundary surface. The case with $\mathbf{E_0}$ in the plane

of the boundary surface ($\perp \mathbf{n}$) is known as surface or 'S' polarization, and the case with $\mathbf{H_0} \perp \mathbf{n}$ is known as the normal or 'P' polarization. The $\mathbf{E_0}$ and $\mathbf{H_0}$ vectors could of course have any orientation in the plane perpendicular to $\mathbf{k}$, but can always be decomposed into surface and normal polarization components. Making use of Eq. 2.7 and imposing the boundary condition that $\mathbf{E}$ and $\mathbf{H}$ must be continuous leads to the Fresnel equations which describe r and t for both polarizations:

$$r_s = \frac{\tilde{n}_1 \cos\theta_i - \tilde{n}_2 \cos\theta_t}{\tilde{n}_1 \cos\theta_i + \tilde{n}_2 \cos\theta_t}, \tag{2.16a}$$

$$r_p = \frac{\tilde{n}_2 \cos\theta_i - \tilde{n}_1 \cos\theta_t}{\tilde{n}_2 \cos\theta_i + \tilde{n}_1 \cos\theta_t}, \tag{2.16b}$$

$$t_s = \frac{2\tilde{n}_1 \cos\theta_i}{\tilde{n}_1 \cos\theta_i + \tilde{n}_2 \cos\theta_t}, \tag{2.16c}$$

$$t_p = \frac{2\tilde{n}_1 \cos\theta_i}{\tilde{n}_2 \cos\theta_i + \tilde{n}_1 \cos\theta_t}, \tag{2.16d}$$

The reflection and transmission coefficients defined above describe the relative magnitudes of the electric fields. The fraction of optical power reflected or transmitted is then $|r|^2 \equiv R$ and similarly $|t|^2 \equiv T$. These magnitudes are different depending on the polarization, but in instances of unpolarized radiation such as sunlight, an average over the two polarizations can be used.

2.2.3 Ray optics

The above sections have considered plane waves that are infinite in extent, and their interaction with material regions that also extend to infinity. In practice this is clearly not always a useful assumption. The regime of validity of the plane wave assumption is defined by the wavelength of the radiation compared to the size of the material boundaries. In the limit that the wavelength is much smaller than the scale of material boundaries, wave-optical effects (diffraction) can be neglected and this plane wave assumption holds. This regime leads to a simplified treatment of electromagnetic radiation known as ray optics, in which the wavevector $\mathbf{k}$ can be used to represent the direction of propagation. Together with Snell's law and the fresnel equations as well as Eq. 2.13 that describes absorption, realistic simulation of electromagnetic wave propagation can be carried out. [12]

2.2.4 Specular and Lambertian surfaces

Snell's law and the Fresnel equations describe the interaction of a plane wave with a smooth planar boundary between two media. This is known as a specular surface, where the angle of reflection equals the angle of incidence, and the qualities of the outgoing reflected beam are the same as the incident one, namely remaining a collimated plane wave. However, this is only strictly true if the surface is perfectly flat, i.e. the normal vector points the same direction at all points. This is clearly an ideality, as most surfaces display some degree of random roughness. In this case, the reflected component will not have a planar wavefront, and will consist of radiation flowing throughout some range of solid angles. This component is known as diffuse reflection. The quantity radiance is used to characterize the flow of radiation out from some surface as a function of solid angle. It has units of power or photon flux per unit source area per unit solid angle.

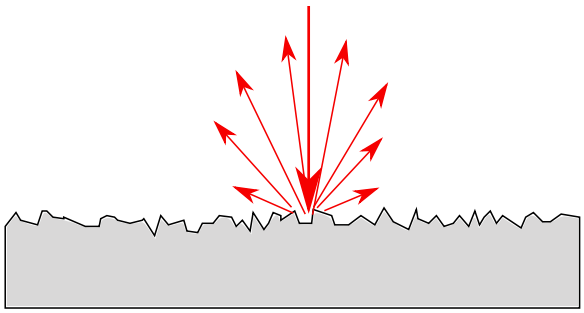

Figure 2.4: A diagram of a diffuse lambertian surface. The lengths of the rays are roughly proportional to the radiance in that particular angle.

In general, the functional form of the radiance is dependent on the surface roughness characteristics (the steepness of the surface topography features), but one idealistic case is particularly relevant, termed a Lambertian. In this case, the radiance L is:

$$L(\theta) = L_n \cos\theta, \tag{2.17}$$

where L_n is the radiance in the normal direction to the surface. A Lambertian

displays the special property that the observed radiance per unit projected source area is constant regardless of the viewing angle. Through the radiance falls off as $\cos\theta$, the projected source area also scales the same way, thus canceling each other out. [13]

2.2.5 Intensity Enhancement

When radiation propagates in a medium with non-specular surfaces that has a higher refractive index than the surrounding medium, there is a tendency for rays to be trapped and undergo many bounces before escaping, due to total internal reflection. This leads to a higher internal intensity than that of the incident radiation and can enhance absorption due to an effective longer path optical path length. To examine this further, we consider isotropic radiation propagating within a medium of refractive index n_{int}, surrounded by an external medium with index n_{ext}, both assumed to be real in this case. With $n_{\text{int}} > n_{\text{ext}}$, rays incident on the boundary surface will experience total internal reflection if the incident is greater than the critical angle θ_c defined by Snell's law:

$$\sin\theta_c = \frac{n_{\text{ext}}}{n_{\text{int}}}.$$

The escaping intensity I_{esc} (units of power per area), can be expressed as:

$$I_{\text{esc}} = I_{\text{int}} \int_0^{\theta_c} T_{\text{esc}}(\theta) \cos\theta \sin\theta d\theta,$$

where I_{int} is the internal intensity, and $T_{\text{esc}}(\theta)$ is the transmission as a function of incident angle θ. To simplify the integral, $T_{\text{esc}}(\theta)$ can be replaced by an effective transmission value $\bar{T}_{\text{esc}}$, which is a weighted average over angles up to θ_c. In this case, the solution to the integral becomes:

$$I_{\text{esc}} = I_{\text{int}} \bar{T}_{\text{esc}} \left(1 - \cos^2\theta_c\right).$$

Using the identity $\cos\left[\sin^{-1}(\theta)\right] = \sqrt{1-\theta^2}$ and the definition of θ_c, I_{esc} can be written in terms of the refractive indices:

$$I_{\text{esc}} = \frac{I_{\text{int}} \bar{T}_{\text{esc}} n_{\text{ext}}^2}{n_{\text{int}}^2}. \tag{2.18}$$

This equation relates the intensity that escapes to the internal intensity. In steady state, the intensity that enters the medium is equal to the intensity that escapes. Let I_{ext} be the intensity incident on the medium from outside with an average transmission $\bar{T}_{\text{ext}}$ into the medium. Using the steady state condition, the internal intensity is:

$$I_{\text{int}} = I_{\text{ext}} \frac{\bar{T}_{\text{ext}} n_{\text{int}}^2}{\bar{T}_{\text{esc}} n_{\text{ext}}^2}. \tag{2.19}$$

As the above equation shows, the internal intensity is enhanced by a factor $\frac{n_{\text{int}}^2}{n_{\text{ext}}^2}$. In general, the ratio of the transmission factors is roughly unity.

2.3 Silicon optical properties

In this section we highlight the optical properties of silicon, and their relevance to solar cell design. Of particular interest is the absorption, a vital property for efficient solar cell operation. Other properties such as the reflectivity are also relevant in this sense, since this influences the ease of coupling light into silicon material regions.

The energy band gap utilized in crystalline silicon solar cell designs is an indirect gap which leads to a relatively weak absorption coefficient since a phonon is also required in the absorption process. The absorption length of silicon ($L_{\text{abs}} \equiv 1/\alpha$) is shown in Fig. 2.5 a.). This quantity represent the material thickness required to absorb a fraction $(1 - e^{-1})$ of the incident solar radiation. L_{abs} varies over several orders of magnitude across the solar spectrum from micron scale at short wavelengths to millimeter scale at near bandgap infrared wavelengths complicating solar cell design. Device thicknesses of hundreds of microns are required to optimally absorb infrared photons, placing high purity requirements on the silicon material.

The real component of the silicon refractive index as well as the reflectivity of a planar interface is shown in Fig. 2.5. Due to the indirect bandgap, the imaginary component of the refractive index is small for solar wavelengths and can generally be neglected in the calculation of the reflectivity using the fresnel equations. The high refractive index of silicon increases the reflectivity making it more difficult to

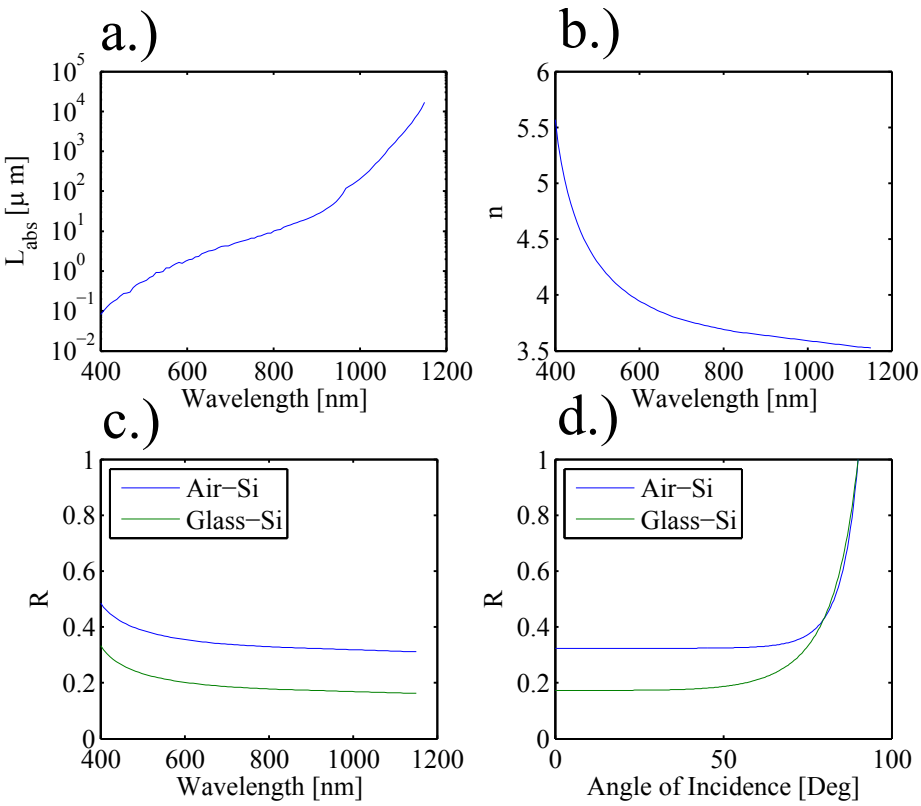

Figure 2.5: Summary of crystalline silicon optical properties. Values calculated using optical constants from Palik. [15] a.) Absorption length as a function of wavelength. b.) Real component of the refractive index. c.) Fresnel reflectivity for an air-silicon and glass-silicon interface as a function of wavelength as normal incidence. d.) Fresnel reflectivity as a function of angle of incidence at a 900 nm wavelength.

couple light into silicon to be subsequently absorbed. However, a high index is an advantage for trapping potential as seen in section 2.2.5, which improves light absorption in the infrared regime where a long path length is necessary.

2.3.1 Techniques for increasing Si absorption

Due the relatively weak absorption coefficient of crystalline silicon, there is interest in methods that enhance material absorption. There have been a large variety of techniques developed which can generally be classified into 4 different general

categories, shown in Fig. 2.6.

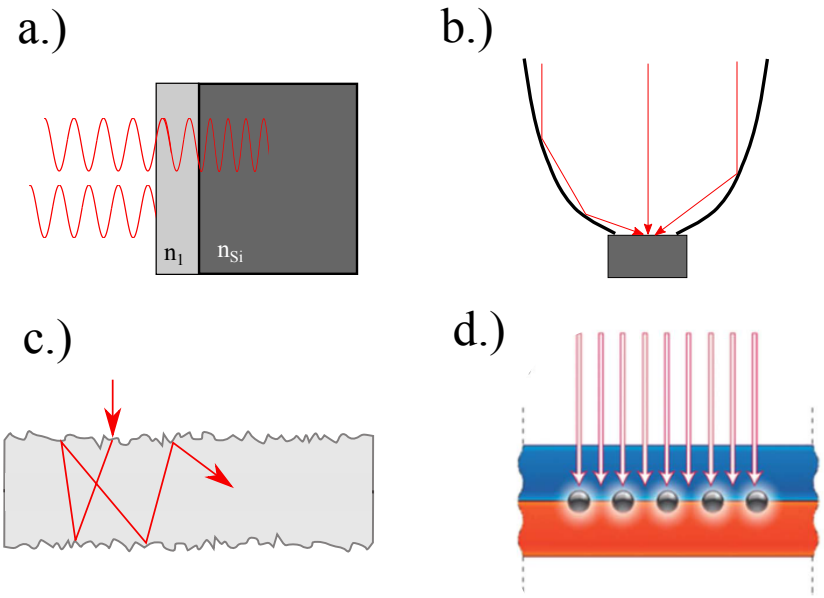

Figure 2.6: Strategies for improving Si absorption which include antireflection coations (a.)), specular techniques (b.)), surface texturing (c.)), and wave-optic effects (d.)). d.) is taken from Hue *et al.* [16]

Antireflection coatings: These are aimed at decreasing the reflectivity of the silicon material interface through wave-interference effects by applying a thin coating. The coating is designed such that the components from the two boundaries experience destructive interference as shown in Fig. 2.6 a.), thus minimizing the reflected component. The performance is dependent on wavelength and angle of incidence, yet multilayer coatings can achieve reduce the reflectivity to $< 4\%$ over a wide range of wavelengths and incident angles. [17]

Specular techniques: These include structures to direct light into silicon regions as shown in Fig. 2.6 b.), or aim to trap light in the structure. In principle these can also be regarded as solar concentration techniques. The conical etch cone design is an example of this technique.

Ray-randomization techniques: These often involve textured front and or

back surfaces (Fig. 2.6 c.)) to randomize rays such that an intensity enhancement similar to that described in the section 2.2.5 can occur. This intensity enhancement translates into an absorption enhancement of up to $4n^2$ where n is the material refractive index, especially at weakly absorbing wavelengths. [18]

Wave-optic effects: These include effects that confine and guide light in silicon regions, or increase the electric field through plasmonic effects, such as the concept shown in Fig. 2.6 d.). [16]

2.4 Radial junction solar cells

As described in the section 2.1, the optimal device thickness of a planar cell is a trade-off between increased optical absorption of infrared photons and reduced carrier collection efficiency. Charge carriers generated near the back-surface must travel a greater distance to reach the junction, increasing the probability they will recombine. Higher-purity material with a greater carrier diffusion length can increase this collection efficiency, yet this increases the cost of the cell. This trade-off motivates an alternative radial junction geometry, shown in Fig. 2.7. The junction covers the sides as well as the top of this cylindrical cell, with solar radiation incident on the top surface. Excited charge carriers can travel in the radial direction to reach the junction, while photons generally progagate along the length of the cylinder. The axes for carrier collection and optical absorption are thus decoupled allowing optimization of both independent of the other. The length of the cylinder or 'wire' can be increased to enable higher photon absorption without influencing the carrier collection efficiency, while the diameter of the cylinder can be made comparable to the minority carrier diffusion length to enable efficient collection of charge carriers. A radial junction cell can thus in principle utilize low-purity material with short carrier diffusion lengths while preserving efficient carrier collection and device efficiency by tuning the diameter of the wire. [19]

However, the radial junction design is not without inherent drawbacks and challenges. The greater surface area-to-volume ratio of the radial design compared to

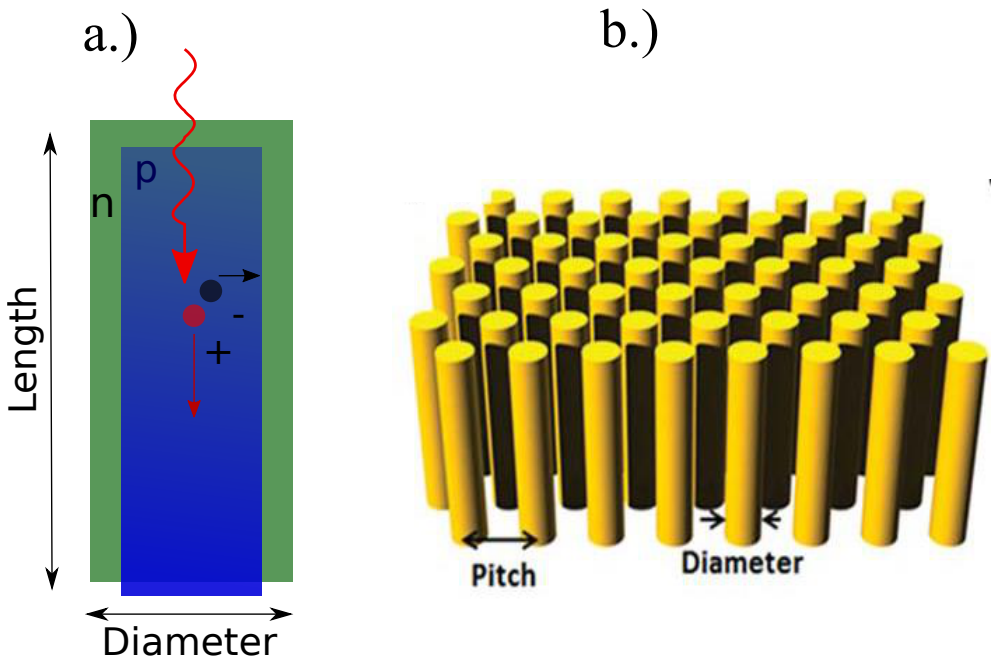

Figure 2.7: a.) A diagram of a radial junction. Light generated charge carriers on average travel a radial distance to the junction, while the wire length can be tuned to improve absorption. b.) An array of vertically aligned radial junction wires. Taken from Hua *et al.* [16]

a planar junction results in parasitic effects on device performance. [19, 20] One is related to the greater junction area relative to an equivalent planar device which can degrade the open circuit voltage. Recalling Eq. 2.3, the open circuit voltage is a function of the ratio of the short circuit current and the dark current parameter J_0: $V_{\text{oc}} \propto \ln[\frac{J_{\text{sc}}}{J_0} + 1]$. In the radial junction case, the light-generated current is distributed over a larger junction area which reduces J_{sc} while J_0 is independent of the junction geometry. For a vertically-aligned wire of diameter D and length L, the ratio of the junction area of a radial device versus a an equivalent planar geometry is

$$\gamma = \frac{\pi D^2/4 + \pi DL}{\pi D^2/4} = 1 + \frac{4L}{D}, \tag{2.20}$$

where γ is the fractional reduction in short current density. This factor γ tends to

be decreased and is independent of wire geometry for horizontally aligned wires:

$$\gamma = \frac{\pi DL}{DL} = \pi. \tag{2.21}$$

A second parasitic effect is due to surface recombination, which is of increased importance for a radial junction device with greater surface area-to-volume ratio than a planar device of the same area. Surface passivation techniques are of greater importance to radial junction cells since this recombination can degrade the cell performance to a larger extent than planar cells. [19]

Despite these drawbacks and challenges, the potential to utilize lower purity (thus reduced material cost) has motivated a large body of research into radial junction solar cells. The design for upscaling from a single wire to an extended-area cell typically involves an array of vertically aligned-wires in a forest geometry as shown in Fig. 2.7. [21] [22] [23] [24] [25] Gaps between the array wire elements (the pitch $>$ diameter as shown in Fig. 2.7) imply a reduced volume of material compared to a planar cell of the same thickness. This reduced volume or fill fraction further reduces material costs and is another attractive feature of radial junction cells.

Though a range of materials have been studied, we will focus in this case on silicon. There have been a number of demonstrated methods for manufacturing radial junction silicon wire arrays which include catalyst assisted vapor liquid solid growth, [21] [26] deep reactive ion etching, [27] high pressure chemical vapor deposition, [28] as well as molten-core fiber drawing. [9] High fractional absorption has been achieved in these structures despite an areal fill fraction of silicon far less than one. This has generally been attributed to absorption enhancement via ray randomization as described by Yablonovitch [18] for larger scale ($\geq \mu$m diameters), and wave-optical effects for nm-scale diameter devices. Kelzenberg *et al.* reported micron-scale diameter wire arrays demonstrating 85% absorption of the integrated incident solar radiation over all above-bandgap wavelengths despite only a $\sim 5\%$ areal fill fraction. [21] This was achieved by applying an anti-reflection coating to the wires and embedding the array in a polymer material with a backreflector and scattering molecules to aid in ray randomization. Despite short minority carrier dif-

fusion lengths, the device achieved near unity internal quantum efficiency by using wire diameters of the same scale demonstrating the advantages of radial junctions. A number of devices of smaller diameters (micron or less) have been reported to exceed the Yablonovitch light trapping likely due to wave-optic effects. [29] [30] [31] [32] As the wire diameter becomes comparable to the optical wavelength wave-optical effects become significant, and ray-optical modeling becomes inadequate for understanding the absorption mechanisms in these structures. [24] Though the underlying physics responsible for the enhanced absorption is still under investigation it is commonly attributed to an increase in the local optical density of states. [29] [16] Horizontally aligned microwire arrays have also been suggested and studied, but to a far less extent. [25] [33] Small wire diameters have limited the absorption of these arrays in the literature.

2.5 Absorption Measurements

This section presents background information and theory relevant to the experimental setup for making absorption measurements. The approach used here assumes the fractional sample absorption A can be described as:

$$A = 1 - R - T, \tag{2.22}$$

where R and T are the total reflected and transmitted components from the sample. For most cases here, the transmitted component could be neglected, making the absorption as one minus the reflectivity.

In the simplest sense, conducting reflectivity measurements involves irradiating a sample and measuring the magnitude of the reflected radiation. If the reflected radiation from the sample is specular in nature, a relatively simple system could potentially be used consisting of a single detector placed to capture the reflected radiation. However, for samples where the reflected component deviates from being perfectly specular, a more complex radiation 'collection' system is required to capture reflections over all solid angles. An integrating sphere is commonly utilized in

this case, allowing measurements to be made of the total reflected radiation from samples regardless of the angular distribution. The sphere walls are covered with a diffuse coating, which has the effect of spatially averaging the total reflected flux over the entire wall area. Using a detector whose field of view contains a portion of the sphere walls, the total reflected radiation component can thus be measured.

2.5.1 Integrating sphere theory and design

The integrating sphere is commonly used in characterizing the total sample reflectivity, i.e. when no angular dependence of the reflectivity profile is desired. In this section, the optical flux of photons on the walls will be derived as a function of the incident flux irradiating a small surface of the sphere wall, or in practice, the sample port. The following definitions will be used:

$$\begin{aligned}\Phi &\equiv \text{Flux [photons/s]}\\ L &\equiv \text{Radiance } [\frac{\text{photons}}{\text{s m}^2\text{sr}}]\\ \rho &\equiv \text{Reflectivity [Unity]}\\ M &\equiv \text{Sphere enhancement factor [Unity]}\end{aligned}$$

Now, the flux on the sphere walls resulting from an input flux will be derived. It is first useful to consider the flux incident on one area element, dA_1, due to the radiation from area element dA_0. This is depicted in Fig. 2.8. If dA_0 is a diffusively reflecting surface, the radiance L_0 is: [34]

$$L_0(\theta) = L_n \cos\theta, \tag{2.23}$$

where θ is the angle from the surface normal, and L_n is the radiance in direction normal to the surface. The total flux Φ_0 radiated from dA_0 can be expressed:

$$\begin{aligned}\Phi_0 &= dA_0 \int_0^{2\pi}\int_0^{\pi/2} L_n \cos\theta \sin\theta d\theta d\phi\\ &= \pi dA_0 L_n \left(\cos^2(0) - \cos^2(\frac{\pi}{2})\right) = \pi dA_0 L_n.\end{aligned}$$

Therefore the radiance L_0 can be written:

$$L_0(\theta) = \frac{\Phi_0}{\pi dA_0} \cos\theta. \tag{2.24}$$

Considering Fig. 2.8, the flux Φ_1 incident on dA_1 can be expressed as:

$$\Phi_1 = L(\alpha) dA_0 d\Omega, \tag{2.25}$$

where $d\Omega$ is the solid angle subtended by dA_1, as viewed from dA_0. From Fig. 2.8, we can see:

$$d\Omega = \frac{dA_1 \cos\alpha}{r^2} = \frac{dA_1}{4R^2 \cos\alpha},$$

since $r = 2R\cos\alpha$. Thus, the flux at dA_1 is:

$$\Phi_1 = \frac{\Phi_0 dA_1}{4\pi R^2}. \tag{2.26}$$

This is significant since it is independent of the location of dA_1 relative to dA_0 (expressed by the angle α). [34]

The total flux accumulated on the walls of the sphere in steady state can be calculated accounting for multiple bounces from the sphere walls. The initial reflected flux reflected from the irradiated surface can be expressed as $\Phi_0 = \rho_0 \Phi_i$, where Φ_i is the incident flux and ρ_0 is the irradiated surface reflectance (both assumed to be independent of position in this case). This flux Φ_0 is then incident on the sphere walls, contributing to another flux component $\bar{\rho}_w \Phi_0$ after reflection, where $\bar{\rho}_w$ is the average wall reflectivity of the sphere, taking into account any openings. Furthermore, there is a further flux component $\bar{\rho}_w^2 \Phi_0$ after the second reflection. Continuing, the total flux Φ_{tot} on the wall surface can be written: [34]

$$\begin{aligned} \Phi_{tot} &= \Phi_0(1 + \bar{\rho}_w + \bar{\rho}_w^2 + \bar{\rho}_w^3 + \dots) \\ &= \frac{\Phi_0}{1 - \bar{\rho}_w}, \end{aligned}$$

valid for $\bar{\rho}_w \leq 1$. The above equation indicates that the total flux on the walls after many reflections will be greater than the intitial reflected flux Φ_0, by a factor $M \equiv \frac{1}{1-\bar{\rho}_w}$.

If we consider a sphere with wall reflectivity ρ_w, total surface area A_s, and a series of port openings of areas a_i with reflectivities ρ_i, the average wall refectivity can be expressed as:

$$\bar{\rho}_w = \sum_i \rho_i a_i / A_s + \rho_w \left(1 - \sum_i a_i / A_s \right). \tag{2.27}$$

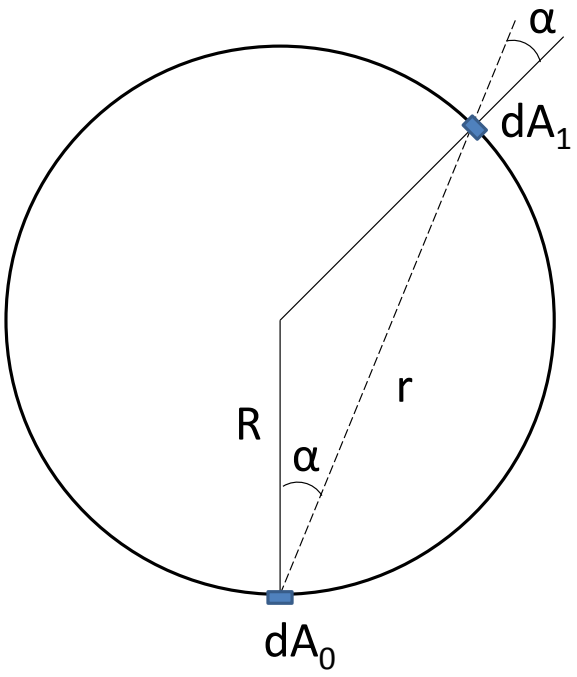

Figure 2.8: A diagram of sphere flux transfer from dA_0 to dA_1. Modified from Goebel. [34]

Measuring the sample reflectivity using an integrating sphere involves comparing the wall flux due to the irradiation of the test sample to the flux with a sample of known reflectivity. Using an approach called the substitutional method, subsequent measurements are made irradiating the test sample and reference material placed in the sample port.

With the sample in place, the measured flux, Φ_s, is

$$\Phi_s = \Phi_i \rho_s M_s, \tag{2.28}$$

where Φ_i is the incident flux on the sample port, ρ_s is the sample reflectivity, and M_s is the sphere efficiency with the test sample in place. With the reference in place, the measured flux, Φ_r, is

$$\Phi_r = \Phi_i \rho_r M_r, \tag{2.29}$$

where the subscripts r refer to the reference sample. The ratio of the two measurements is:

$$\frac{\Phi_s}{\Phi_r} = \frac{\rho_s M_s}{\rho_r M_r},$$

and the sample reflectance can be found:

$$\rho_s = \rho_r \frac{M_r \Phi_s}{M_s \Phi_r}. \tag{2.30}$$

This method gives the correct reflectivity for the case where $M_s = M_r$. Otherwise, there is an error term introduced. [34] [35] [36]

2.5.2 Monochomator theory

Spectroscopic information is typically desired when measuring sample reflectivity, thus requiring measurements as a function of irradiation wavelength. A monochromator is commonly employed in this case, which functions as an optical filter of sorts allowing only a narrow spectral band of a broadband input source to pass through the output aperture. The key optic of a monochromator is a dispersive element such as a grating or prism which separates the spectral components in angle space. Since the monochromator employed in this study utilized a prism, we will focus on this particular case here, but much of the description holds for a system using a grating as well. The angular deflection of a plane wave from a prism is:

$$\theta_d = \theta - \beta + \sin^{-1}\left[\sqrt{n(\lambda)^2 - \sin^2\theta}\sin\beta - \sin\theta\cos\beta\right], \tag{2.31}$$

where θ_d, θ, and β are defined in Fig. 2.9 and $n(\lambda)$ is the wavelength dependent refractive index of the prism. [12] The deflection angle θ_d is thus wavelength dependent due to $n(\lambda)$. A aperture or slit downstream of the prism thus allows only a subset of wavelengths to pass through as shown. Controlling the size of slit controls

the spectral bandwidth of the output radiation. Rotating the prism changes which set of wavelengths passing through the output slit. By rotating the dispersive element and controlling the slit, the user has control over the center wavelength and spectral bandwidth of the output radiation. It is important to note that Fig. 2.9 is a simplification of a monochromator optical system which likely includes lenses to collimate the rays as well as potentially other relay optics.

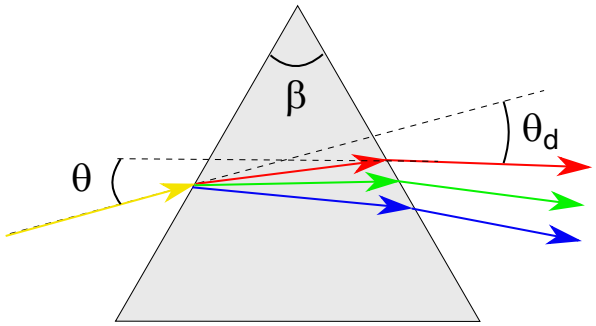

Figure 2.9: Diagram of a prism with the relevant angles in Eq. 2.31 denoted.

2.5.3 Photodetector theory

Measuring the wall flux typically involves mounting a photosensitive detector to one of the sphere port openings such that sections of the sphere walls are contained in the detector field of view (FOV). A photodetector was used in this work, which operates much in the same way as a solar cell with absorbed photons exciting electrons across a band gap. Contrary to a solar cell it is operated with negative bias of the electrodes (often termed the third quadrant of the I-V characteristic curve). In this case, the current is effectively independent of the bias voltage, and approximated well by the short circuit current. From Eq. 2.2 we can see that this current is proportional to the incident photon flux, making it a useful radiation detector. [37]

As with a solar cell, photons with energies below the bandgap of the photodector

material are not absorbed. This determines the spectral range of detection. Other design parameters such as the material thickness and reflectivity of the front surface determine the quantum efficiency of the device: the number of electrons on average that are added to the circuit per incident photon.

2.5.4 Lock-in amplifier theory

A lock-in amplifier aids in measuring a signal of interest in the presence of a large degree of noise. The device uses a principle called phase-sensitive detection to measure the amplitude of a particular frequency component present in the signal, while effectively filtering out other frequencies (containing noise). The device requires two inputs: a signal and a reference. The reference is typically a sine wave or a square wave at the desired detection frequency. For the purposes of this description, we assume that the signal S is a sine wave of frequency ω_s with relative phase $\Delta\phi$:

$$S(t) = S_0 \sin(\omega_s t + \Delta\phi).$$

We assume the reference $R(t)$ is a square wave with frequency ω_{ref}:

$$R(t) = \Pi(\omega_{\text{ref}} t).$$

The quantity $\Delta\phi$ is the relative phase between $S(t)$ and $R(t)$. Both the signal and reference are inputs to the phase sensitive detector, which through the use of a synchronous switch generates an output signal that is effectively the multiplication of the reference with the input signal. If the signal and the reference have the same frequency ($\omega_s = \omega_{\text{ref}}$) and there is no phase difference ($\Delta\phi = 0$), the resulting product will have a non-zero time-averaged mean value. For $\omega_s \neq \omega_{\text{ref}}$, the mean will tend towards zero. The phase sensitive detector thus functions to pick out the fourier component of the input signal at frequency ω_{ref}, where the mean of the output signal is related to S_0. [38]

In the case of the analog lock-in amplifier used in this study (Brookdeal 401), a resistor-capacitor (RC) low pass filter is implemented to yield a near-DC output

signal from the phase sensitive detector. The time constant of this RC filter controls the bandwidth of the output signal and its temporal response to changes in S_0. [38]

The experimental setup can be designed such that the desired signal of interest is oscillatory at a given frequency of choice equal to the reference frequency. In this work, an optical chopper was used to create AC intensity modulated input radiation. Even if there are significant noise components that may dwarf the amplitude of the signal of interest, as long as there is not a significant component of noise at the same frequency, the DC output signal from the lock-in amplifier will be proportional to S_0.

Chapter 3

Methods

This chapter describes the methods used to characterize the two silicon microwire array designs. This involved both modeling and experimental techniques. The first part describes the modeling techniques used which included ray tracing code in 2D and 3D written in MATLAB, as well as two simpler analytically models. The experimental work involved assembling arrays of horizontally aligned microwire arrays, and sample absorption measurements using an integrating sphere setup.

3.1 Modeling

3.1.1 Ray Tracing code

This section describes ray tracing code written in MATLAB. Code was written to handle both 2D and 3D cases. The inputs are defined slightly differently depending on the dimensionality, but in both cases the ray tracing algorithm consists of two functions. The first is a lower level function which propagates a single input ray until it intercepts the next material boundary (if any), and generates two output rays corresponding to the reflected and transmitted components at the material boundary. The second is a higher level function to run further iterations of this lower level function, and perform the necessary book keeping to organize the entire set of rays generated. This higher level function allows the user to launch a single

ray at a structure of defined material boundaries, returning the entire set of rays that traverse through the structure. Here we will describe the details of how these two functions are implemented.

Inputs

The ray tracing code requires input arguments that specify the characteristics of the initial launched ray and the boundaries that define the various material regions. These input arguments are organized into two input MATLAB structure variables, *Ray*, and *B* respectively. Each of these contain sub fields with the relevant parameters. The *Ray* structure contains the fields:

- **R0**: Column vector specifying the starting position of the launched ray
- **dR0**: Column vector specifying the ray direction. The magnitude (norm) of this vector defines the magnitude of the ray (the associated field intensity).
- **Lambda**: Wavelength of the light
- **Polarization**: The polarization of the light - S, P, or unpolarized. In the unpolarized case, the ray is considered to contain equal components of S and P polarizations.

The *B* structure is an array with each element defining a material region. For the 2D version of the code, each element has the following fields:

- **P**: A $2 \times n$ array specifying the verticis of the material boundary, in counterclockwise order. Counterclockwise order is necessary in determing the correct normal vector to the surface.
- **n**: A function handle specifying the refractive index of the material as a function of wavelength.
- **alpha**: An optional arguement fixing the absorption length of the material. If this field is provided, it will override the absorption calculated from the given

refractive index profile. This can be set to a 'NaN' value to eliminate ray propagation in the material (i.e. if only reflection of incoming rays from the material boundary is relevant to the user).

- **Reflection**: A $1 \times n$ array with reflectivity values of each material side, in the order specified by the 'P' field. These values are set to 'NaN' if the reflectivity calculated from the refractive index is desired.

In 2D, material regions are defined simply by a set of vertices. In 3D, they are defined by bounded planar surfaces. This requires a different set of fields in the B structure input variable. Each element in B structure defines a separate plane specifying a material boundary. Assuming a point **p0** that lies in the plane and two vectors **a1** and **a2** that are parallel to the plane, any point **p** that lies in the plane can be parameterized by:

$$\mathbf{p} = \mathbf{p0} + s\mathbf{a1} + t\mathbf{a2}, \tag{3.1}$$

where s and t are the parameterization variables. The boundaries of the plane are defined by a set of line segments i that place limits on s and t:

$$sc_i \leq tm_i + b_i. \tag{3.2}$$

c_i, m_i, and b_i thus are chosen to define the planar boundaries. Material volumes can be defined by a sequence of planes, for example a cube volume using 6 square planes. It is up to the user to ensure that the boundaries of the planes are defined correctly to create the desired material shape, and that the planes define an enclosed volume.

The B structure variable for the 3D code contains the following fields:

- **p0** Three-element column vector defining a point on the plane
- **a1** A unit vector parallel to the plane
- **a2** A second unit vector parallel to the plane.
- **c_i** 1D array defining the plane boundary (see Eq. 3.2)

- **m_i** (see Eq. 3.2)
- **b_i** (see Eq. 3.2)
- **n** The refractive index on the opposite side of the plane from normal vector direction
- **Reflection** The reflectivity of the plane, which if provided will override calculation based on the fresnel equations.

One final additional input argument is provided, specifying the ambient refractive index, typically air approximated as a vacuum. The dimensional units are in general flexible, but the vertices, wavelength, and function specifying the refractive index must all be defined with the same units.

Single ray iteration algorithm description

A brief description of the steps involved in a single ray iteration are described in this section, and shown in Fig. 3.1. The first step performs initial checks on the inputs provided by the user, setting default values and raising the appropriate errors or warnings if insufficient or contradictory information is provided. The second step finds the next intersection of the input ray with a material boundary. This is implemented by finding the ray intersection with all material boundaries (lines in 2D or planes in 3D), and determining which the ray intercepts first. It is of course possible that the ray does not intersect any boundaries, in which case the function can now return the outputs.

The third step is to calculate the unit vectors of the reflected and transmitted rays at the the boundary as a function of the initial direction vector $\mathbf{k_i}$, as shown in Fig. 2.3. It is useful to decompose the vectors into components that are parallel and perpendicular to the boundary surface. For a general vector $\mathbf{k}$, these are: [14]

$$\mathbf{k}_\perp = (\mathbf{k} \cdot \mathbf{n})\mathbf{n},$$

$$\mathbf{k}_\parallel = \mathbf{k} - \mathbf{k}_\perp,$$

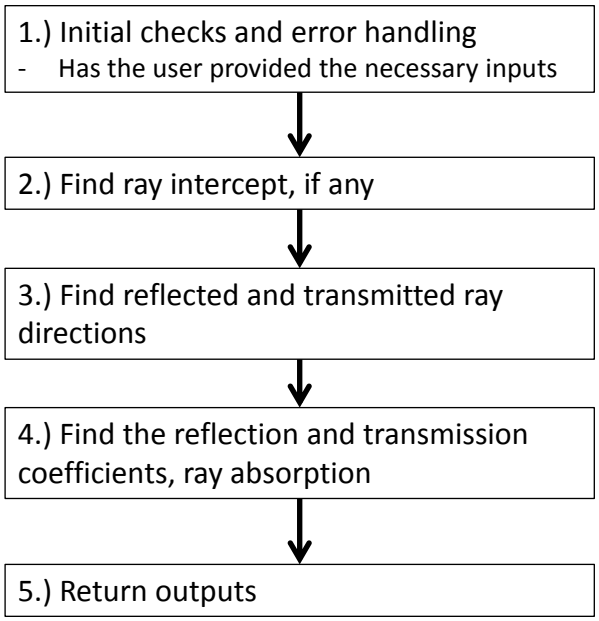

Figure 3.1: A schematic of the single ray iteration algorithm.

where $\mathbf{n}$ is the normal vector to the surface. In the case of the reflected ray, $\mathbf{k_r}$,

$$\mathbf{k_{r,\perp}} = -\mathbf{k_{i,\perp}} = -(\mathbf{k_i} \cdot \mathbf{n})\mathbf{n},$$

$$\mathbf{k_{r,\parallel}} = \mathbf{k_{i,\parallel}},$$

thus,

$$\mathbf{k_r} = \mathbf{k_i} - 2(\mathbf{k_i} \cdot \mathbf{n})\mathbf{n}. \tag{3.3}$$

For the transmitted ray, snell's law requires:

$$\mathbf{k_{t,\parallel}} = \frac{n_1}{n_2}\mathbf{k_{i,\parallel}} = \frac{n_1}{n_2}\left(\mathbf{k_i} + \cos\theta_i \mathbf{n}\right).$$

The perpendicular component can be found using $|k|^2 = |k_\perp|^2 + |k_\parallel|^2$:

$$\mathbf{k_{t,\perp}} = -\sqrt{1 - \sin^2\theta_t}\mathbf{n}.$$

Thus,

$$\mathbf{k_t} = \frac{n_1}{n_2}\mathbf{k_i} + \mathbf{n}\left(\frac{n_1}{n_2}\cos\theta_i - \sqrt{1 - \sin^2\theta_t}\right). \tag{3.4}$$

The fourth step finds the magnitudes of the reflected and transmitted rays using the fresnel equations, and finds the absorption of the launched incident ray in the medium it traversed to reach the material boundary. The final step collects and returns the outputs. These include structure variables with the same arguments as the input *Ray* variable defining the transmitted and reflected rays. The field **dR0** contains the direction vector of the ray with the vector norm representing the reflected or transmitted magnitude. Another output variable is the fractional absorption of the launched ray as it passed through the relevant medium.

Multiple ray iteration algorithm

The preceding section describes the algorithm that finds the transmitted and reflected ray components from a launched ray that encounters a material boundary. These rays in turn will also tend to intercept additional material boundaries, thus generating more rays. Propagating an initial single ray through a structure where rays encounter multiple boundaries requires another algorithm to perform the book keeping and organization of the many rays.

Each iteration where rays encounters a boundary there are two new rays produced, so there are in general approximately 2^m total new rays for iteration number m. To perform the book keeping, the code has two main structure array variables containing lists of defined rays. The first contains all the launched incident rays, and their fractional absorption values. This array is appended following each iteration with more rays. The second structure array contains a list of the new rays generated during a given iteration, which are then the set of launched rays the next iteration. The code performs this process a specified number of iterations to generate a set of rays, each with a weighted fractional absorption value. Summing up these weighted absorption values gives the fractional absorption of the initial launched ray. To ease computational demands, there is ray magnitude value tolerance set. New rays generated with magnitudes below this threshold are not propagated further, and not included in the total set of rays. A diagram of this algorithm is shown in Fig. 3.2.

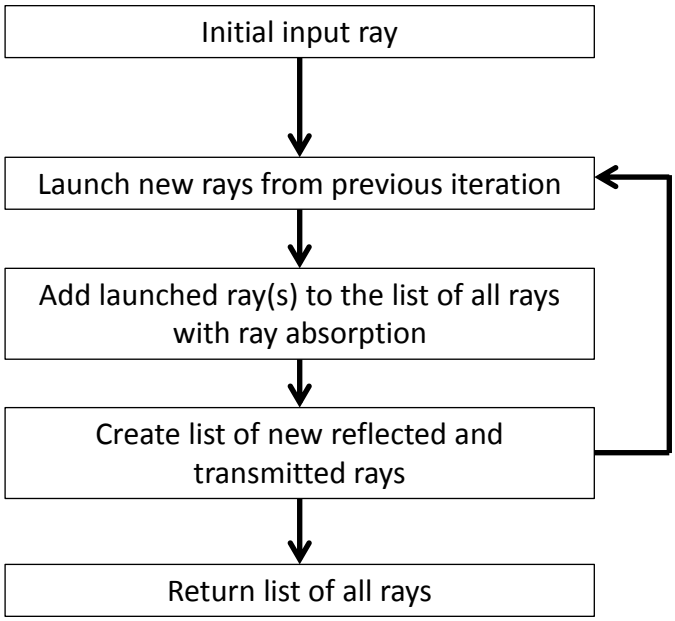

Figure 3.2: A schematic of the multiple ray iteration algorithm.

Representation of 3D surfaces

The 2D version of the code defines material regions as a set of vertices, which is relatively trivial. On the other hand, the 3D version of the code defines surfaces as a set of bounded planes, which is more complicated warranting a short discussion here with an example relevant to the cone geometry.

To model the cone geometry in 3D, the user needs to define a cylindrical wire surface, as well as a conical surface. The cylindrical section can be defined using two n-sided regular polygon planar regions approximating the circular top surfaces, and a set of n rectangular planes defining the sides. The long dimension of these rectangular planes is the wire length, with the normal vector to each plane pointing in the positive radial direction. A cylinder with $n = 16$ is shown in Fig. 3.3. The conical surface can be approximated with n trapezoidal planar regions as shown in Fig. 3.3. Though a value of $n = 16$ is shown here for viewing convenience, a value

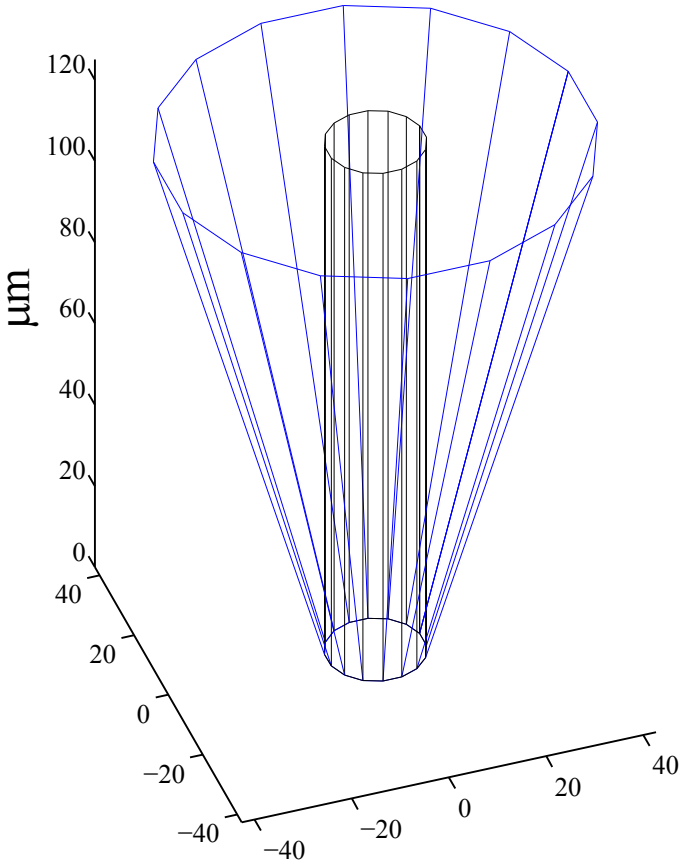

Figure 3.3: A diagram of the 3D representation of the cone structure. The blue lines indicate the boundaries of 16 trapezoidal planes which define the conical surface, while the black lines indicate the boundaries of the planes defining the cylindrical wire.

of $n = 64$ was used in the modeling presented later in this work.

3.1.2 Statistical ray model

Even without any intentional attempt to create rough surfaces, there is a tendency for rays entering a medium to become randomized, as described by Yablonovitch [18]. In this case, a statistical ray model can be developed to predict the internal intensity, as well as absorption. The radiation is considered to be isotropic, such that the photon flux density incident on any surface is proportional to an internal intensity

regardless of the surface orientation.

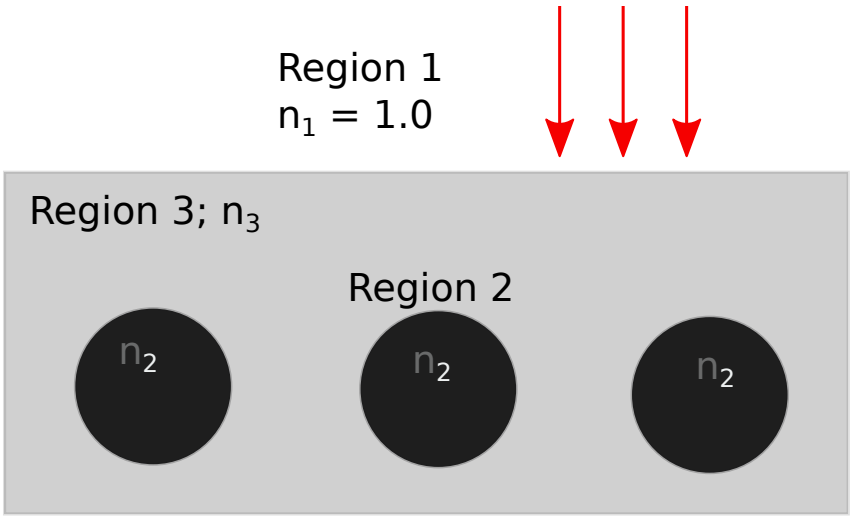

Figure 3.4: A diagram of the structure considered in the statistical ray model. Silicon wire sections (denoted as Region 2 with refractive index n_2 and viewed end on) are embedded in a medium (Region 3) with index n_3. Light is initially incident from Region 1 assumed to be vacuum.

In this section, we consider a geometry of sections of Si embedded in a medium of refractive index n_3, representative of glass, PDMS, or epoxy as shown in Fig. 3.4. The general technique, as described by Yablonovitch, [18] involves balancing the inflow and outflow of photons within each material region. We begin by considering a simpler case, in the high-absorption regime of Si (valid wavelengths in the visible range) where light that enters the Si region is immediately absorbed. Thus, there is no outflow from the Si regions (denoted with refractive index n_2). For the surrounding medium (refractive index n_3), the energy inflow is due to the incident radiation, I_1. The outflow is due to light escaping into the incident medium $n_1 = 1.0$, and the Si regions. Thus, an energy balance equation can be written as:

$$A_{13}T_{13}I_1 = \frac{A_{13}\bar{T}_{13}/n_3^2 + A_{23}\bar{T}_{23}I_3}{2}. \tag{3.5}$$

A and T are the surface area and transmission coefficients of the media boundaries denoted by the subscripts, and I is the intensity in the respective media. As before,

internal intensity is assumed to be bi-directional (4π steradians), while I_1 is considered to be radiating in 2π steradians. This is reason for the factor of 2 present in the above equation. We are interested in the absorption in the Si section, which in high absorption regime can be expressed as a function of the light entering the Si:

$$Abs_{\mathrm{Si}} = \frac{A_{23}T_{23}I_3}{2}. \tag{3.6}$$

Abs_{Si} represents the number of photons absorbed in the Si. Expressing this quantity in terms of the incident photons leads to an expression for the fractional absorption of the structure:

$$f_{\mathrm{ABS}} = \frac{A_{23}T_{23}T_{13}}{A_{13}\bar{T}_{13}/n_3^2 + A_{23}\bar{T}_{23}}. \tag{3.7}$$

One can further factor a term $\frac{A_{23}}{A_{13}} \equiv A_{\mathrm{Si}}$:

$$f_{\mathrm{ABS}} = \frac{A_{\mathrm{Si}}T_{23}T_{13}}{\bar{T}_{13}/n_3^2 + A_{\mathrm{Si}}\bar{T}_{23}}. \tag{3.8}$$

A_{Si} is the fractional area of the wires relative to the area of the incident radiation.

The transmission coefficients can be calculated from a weighted average of the transmission as a function of incident angle. For isotropic radiation,

$$\bar{T}_{\mathrm{ij}} = \int_0^{\pi/2} T_{\mathrm{ij}}(\theta)\cos\theta\sin\theta d\theta, \tag{3.9}$$

where $T_{\mathrm{ij}}(\theta)$ is the transmission as a function of incident angle for a ray entering material j from material i. The factor $\cos\theta$ accounts for the intensity reduction as a function of incident angle. For unpolarized light of wavelength 750 nm entering silicon, the transmission factor as a function of the incident medium refractive index (n_3) is shown in Fig. 3.5. As seen, this angular weighted value is not drastically different from the transmission at normal incidence.

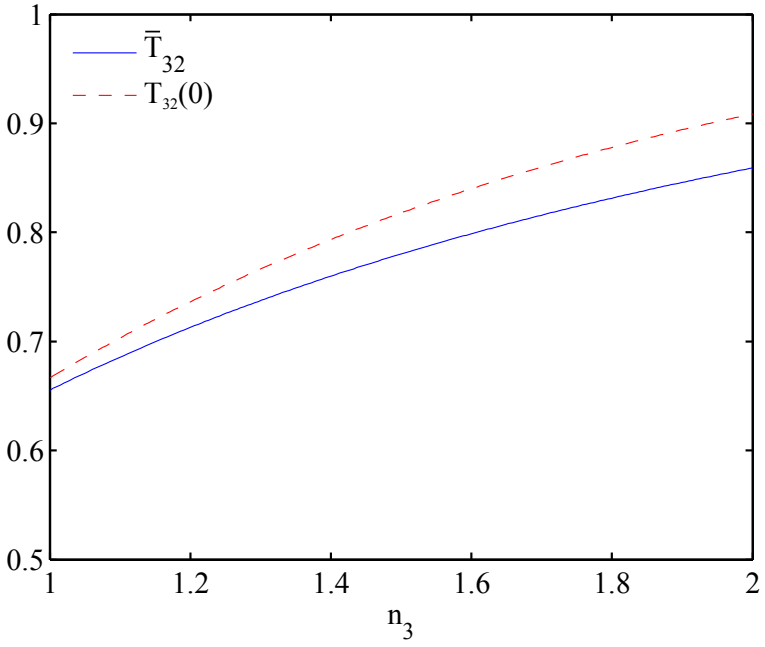

Figure 3.5: The transmission into silicon as a function of the incident medium refractive index n_3. $\bar{T}_{32}$ is the weighted angular average, while $T_{32}(0)$ is the transmission at normal incidence.

3.1.3 Gee model

The ray tracing code and the statistical model both are based on assumptions of the internal radiance distribution. The ray tracing assumes specular surfaces, while the statistical ray model assumes complete ray randomization. Any departure from smooth surfaces limits the applicability of the ray tracing code, while the assumption of complete randomization is of the other extreme, as absorption may take place before complete randomization is achieved. [18] Here, we introduce a simple self-consistent modeling approach similar to that described by Gee [39] which does not inherently rely on these assumptions. The approach expresses the optical intensities at various planes as a function of surface reflectivities and transmission values. An example of the application of this approach to an array of horizontally-aligned silicon microwires is shown in Fig. 3.6. For a wire diameter-to-center-distance ratio F, we

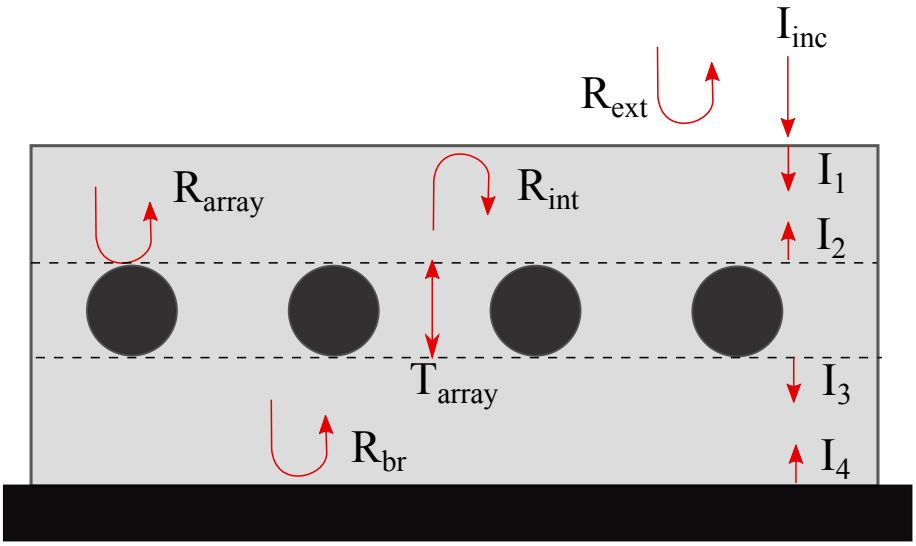

Figure 3.6: A diagram showing silicon microwires embedded in a dielectric with a backreflector. The various terms in Eq. 3.10 are denoted above.

consider a strongly absorbing wavelength in silicon and assume for simplicity that $R_{\text{array}} = R_{\text{Si}}F$ and $T_{\text{array}} = 1 - F$, where R_{Si} is the reflectivity of silicon embedded in the surrounding medium. The backreflector reflectivity R_{br}, internal reflectivity R_{int} and external reflectivity R_{ext} similarly are used to express the intensities at 4 different planes in the structure as denoted by Fig. 3.6:

$$I_1 = (1 - R_{\text{ext}})I_{\text{inc}} + R_{\text{int}}I_2, \tag{3.10a}$$

$$I_2 = R_{\text{array}}I_1 + T_{\text{array}}I_4, \tag{3.10b}$$

$$I_3 = T_{\text{array}}I_1 + R_{\text{array}}I_4, \tag{3.10c}$$

$$I_4 = R_{\text{br}}I_3. \tag{3.10d}$$

The array absorption can be expressed as $A_{\text{array}} = (1 - R_{\text{array}} - T_{\text{array}})\,(I_1 + I_4)$.

For the case of weak absorption, light entering the wires that is not absorbed must be considered. This is accounted for by modifying R_{array} and T_{array}. For simplicity we assume that half the un-absorbed light contributes to R_{array}, and half

to T_{array}. In this case, the modified coefficients are:

$$R_{\text{array}} = FR_{\text{Si}} + (1 - R_{\text{Si}})Fe^{-\alpha l}/2, \tag{3.11a}$$

$$T_{\text{array}} = 1 - F + (1 - R_{\text{Si}})Fe^{-\alpha l}/2, \tag{3.11b}$$

where α is the silicon absorption coefficient and l is the average propagation length in the wires. The array absorption is also modified: $A_{\text{array}} = (1 - e^{-\alpha l})(1 - R_{\text{array}} - T_{\text{array}})\,(I_1 + I_4)$

3.2 Experiments

3.2.1 Assembly of horizontally aligned microwire array samples

Silicon microwires with a surrounding silica cladding layer were fabricated using a molten core fiber drawing technique, similar to that used to make standard optical fibers. Long segments with a silica outer diameter $\sim$ 5-10X the inner silicon microwire diameter were obtained using this method. The silicon microwire diameter was $\sim$ 40-50 μm, measured from optical microscope images calibrated using an object of known size.

Horizontally aligned silicon microwire arrays resembling the structure shown in Fig. 1.4 c.) were assembled by positioning segments of microwires with a fixed center-to-center distance. To improve the accuracy of the positioning, the surrounding silica cladding layer was utilized. These silica-clad wires could then be placed close packed eliminating the need for positioning individual segments separately. The center-to-center distance d is in this case controlled by the thickness of the silica cladding layer. Various cladding thicknesses were achieved by etching the silica in a solution of 48% hydrogen fluoride (HF) in water (Sigma Aldrich) for various times.

Sections of microwires with a partially stripped cladding layer were cut into 2-3 mm segments and placed close packed on a PDMS substrate. These segments were fixed together using a low-viscosity epoxy (EPO-TEK®301). This epoxy was chosen

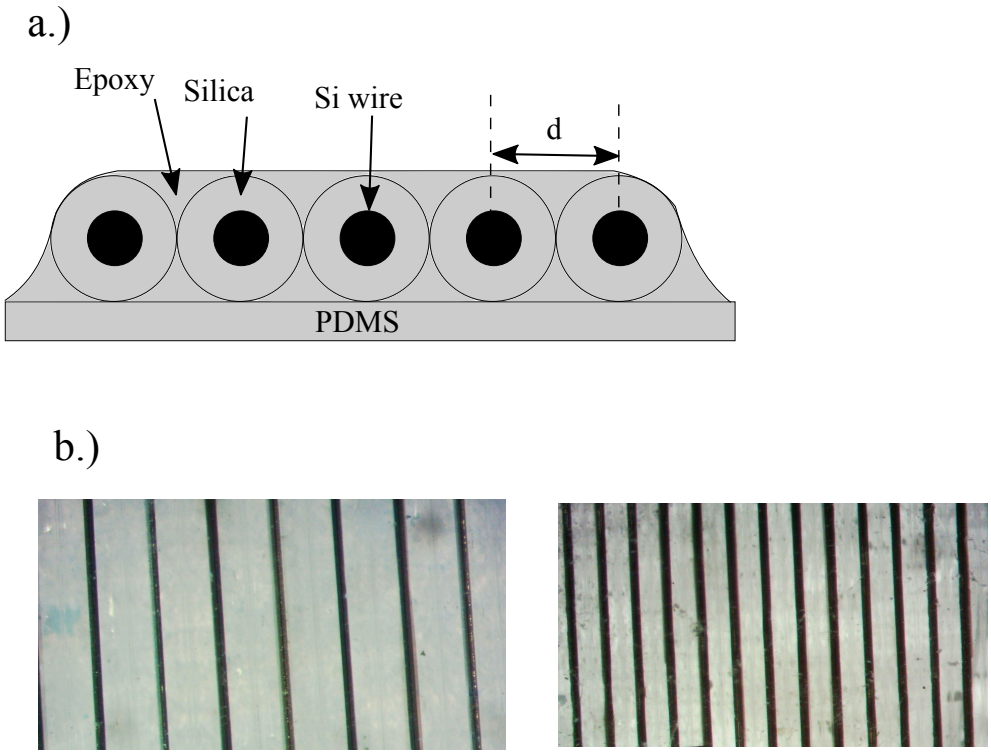

Figure 3.7: a.) An end-on view of an assembled array consisting of silica-clad wires fixed together by epoxy on a PDMS substrate. Dimensions not to scale. b.) Images from the top of two assembled wire arrays of different fill fractions.

as it is optically transparent across the visible and near infrared regions, and has a refractive index similar to silica. The epoxy was cured for 2 hours in an oven at 60°C as recommended.

PDMS films of desired varying thicknesses were achieved by spin coating at 1000 rpm for varying durations. The films were then cured at 80°C for 2 hours. The film thicknesses were measured from side-on images taken with an optical microscope. A spin duration of 25 seconds yielded a film thickness of ≈100 μm, which was the thickness used for the layer separating the wire arrays from the backreflector.

The wire diameter-to-d ratio (fill fraction F) of assembled arrays was determined from analyzed images taken with an optical microscope. The images were taken with the arrays aligned such that the wire lengths were approximately vertical in the ob-

tained images. The average wire periodicity in the horizontal direction of the image was found by calculating the maximum non-DC component of the fourier transform of a horizontal line out. This value was then used to create a mask an integer number of periods across, such that a subsequent gray scale binary thresholding procedure could be used to find the fill fraction. The threshold value was determined using a library MATLAB function that utilizes an algorithm described by Otsu. [40]

3.2.2 Experimental setup for absorption measurements

A basic schematic of the experimental setup is shown in Fig. 3.8. The setup consists of three main subsystems. The first generates narrow spectral bandwidth light with a desired central wavelength, and delivers the radiation to the sample through a system of relay optics. The second is the integrating sphere containing the mounted sample. The third is a detection system to measure the sphere wall flux. The following sections describe the details and components of these subsystems.

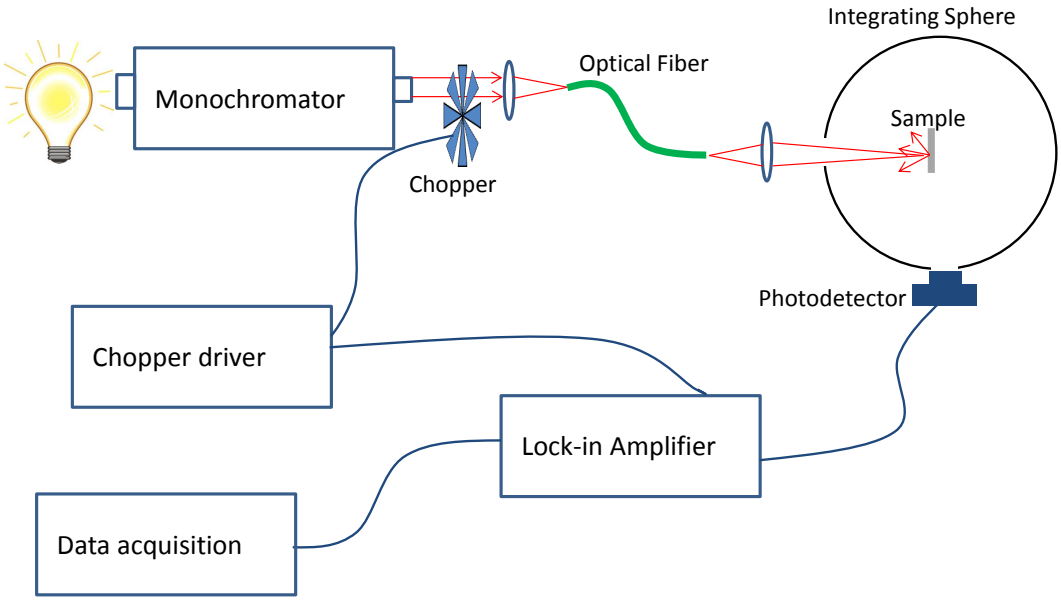

Figure 3.8: A schematic of the experimental setup for absorption measurements.

Light source and delivery system

A Carl Zeiss M4 QIII monochromator system was used as an effective narrow band tunable wavelength light source. A halogen white light bulb source contained in metal housing illuminated the input aperture of the monochromator, which utilizes a prism as the dispersive element. A slit of adjustable width up to 2 mm allowed control of the bandwidth of the output radiation. Little detail is provided in the manual concerning the internal optics, but it is likely that the wavelength adjustment mechanically rotates the prism such that a different spectral component of light exits the output aperture.

The output beam was coupled into an optical fiber (Thorlabs M37L01: 500 μm core diameter, NA = 0.22) using a collimation lens (Thorlabs F220SMA-B: 10.99 mm focal length, NA = 0.25). The opposite end of the fiber was imaged onto the sample using a single lens (Thorlabs A220TM-B: 11.0 mm focal length, NA = 0.26) mounted an adjustable distance away from the fiber tip. The fiber tip-to-lens distance controlled the beam spot size on the sample.

The fiber and lens specifications were chosen to enable a $\sim$2 mm size beam of optimal intensity to be achieved at a distance up to one integrating sphere diameter (45 mm) from the lens.

Integrating sphere

An custom built integrating sphere, shown in Fig. 3.9 was designed to accommodate the small sample sizes of the microwire arrays. There are three port openings for the entering incident light, sample, and detector. In general, there are two possible configurations for these ports. In the first, the sample is mounted externally covering port A, with the incident light entering from port B. The incident light thus irradiates the sample at and angle of 15° relative to the sample port normal direction, ensuring the specular component of the reflected light from the sample will illuminate the walls of the sphere as opposed to exiting back through port B. In this configuration, the sample reflectivity irradiates the sphere walls. This setup has

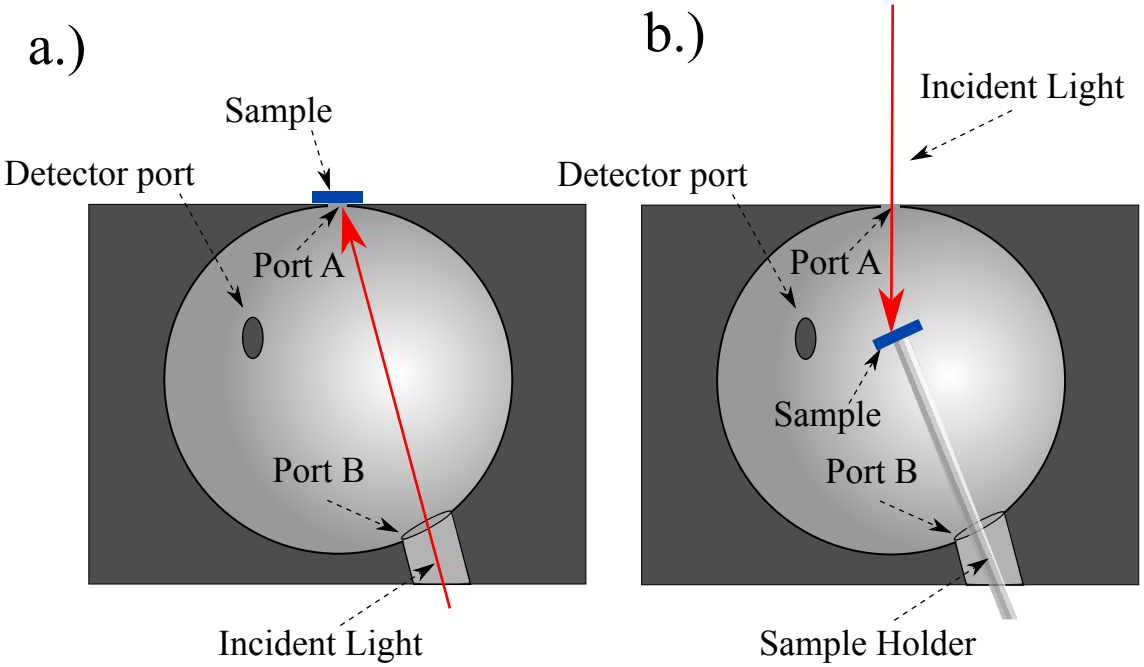

Figure 3.9: A diagram of the integrating sphere with ports (labeled A and B) for the incident light and sample, as well as a detector port. The configuration with the sample mounted externally to port A is shown in a.), while the alternative configuration with the sample mounted internally to the sphere is shown in b.).

the advantage of easier sample alignment with the pre-defined aperture of the port opening. However, finite sample thickness implies that light can be lost out the sides of the sample which are external to the sphere. A second configuration consists of mounting the samples inside the sphere, with the incident light entering through either port A or B depending on the mounting scheme. Using this approach, both the reflected and transmitted component from the sample irradiates the sphere walls. This approach does not suffer the drawback of the former, as any light transmitted or reflected from the sample will in principle irradiate the sphere walls. However, this approach requires more difficult alignment of the samples with respect to the incident radiation. To assist in this case the sample mounting rod was mounted on a 2D translation stage to improve alignment ease and precision. The end face angle of the rod determined the angle of the incidence of the radiation. Several angles

were used to achieve incident angles of approximately 0°, 15°, and 45°. This second configuration was used for the measurements presented here to eliminate concerns over light escaping from the sides of samples.

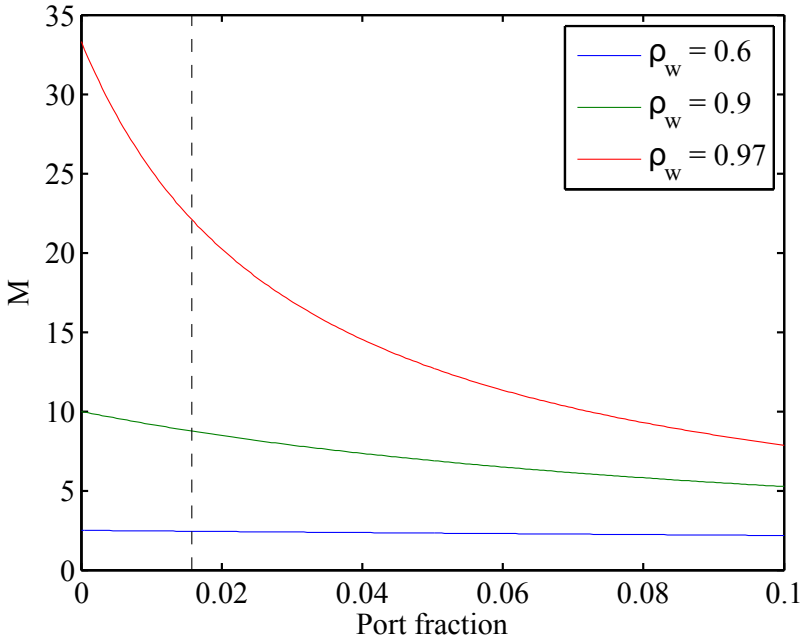

Figure 3.10: Sphere efficiency factor M as a function port fraction for various wall reflectivities ρ_w. The vertical dashed line indicates the port fraction for the sphere designed and used in this work.

The dimensions of the sphere were designed based on integrating sphere theory. [34] [35] [36] The port opening diameters were chosen based on the expected sample sizes ($\approx$ 2 mm), photodetector active area, and input beam dimensions. The optimal outer diameter of the sphere is a trade-off between wall flux ($\propto$ detector signal), and sphere multiplier factor (spatial integration capability). A smaller sphere diameter will increase the wall flux, yet decrease the sphere multiplier factor as the port fraction becomes too large since the average number of wall bounces decreases. A 45 mm sphere diameter with port diameters Port A = 2 mm, Port B = 9.0 mm, and Detector Port = 6.5 mm were chosen as it maintained a small port fraction of

$< 2\%$ and a sphere efficiency factor of over twenty as seen in Fig. 3.10, yet was small enough to enable an adequate detected signal.

The sphere was fabricated out of aluminum by the NTNU machine shop. The internal walls of the sphere were coated with a white diffuse paint (Labsphere 6080) which was expected to perform as a near lambertian reflector with $\approx 97\%$ reflectivity over the visible and near infrared regimes. The coating was applied in many thin layers using an airbrush.

Detection system

A phase sensitive detection system was implemented consisting of a chopper, photodetector, and lock-in amplifier. The chopper (Thorlabs Optical Chopper ML2000) was placed directly downstream of the monochromator output aperture creating a modulated optical intensity signal of known frequency that illuminated the sample. The chopper driver electronics also generate a reference square wave signal of the same sample frequency as the chopper rotation. This signal was connected to the reference input of the lock-in amplifier (Brookdeal Type 401). The photodetector was mounted externally outside sphere port C in Fig. 3.9 such that the field of view of the active area contained a portion of the sphere walls. The detected signal had a frequency defined by the chopper, and an amplitude defined by the sphere wall flux. A silicon photodetector (Thorlabs PDA36A) was used for optical wavelengths up to 1100 nm, while a germanium photodetector (Thorlabs PDA50B-EC) was used for 900 nm and above. This was connected to the input of the lock-in amplifier. The DC output of the lock-in amplifier was recorded using a digital-to-analog converter (DATAQ Model DI-155) and MATLAB software.

The lock-in amplifier based detection system was implemented to improve the signal-to-noise ratio alleviating the effects of ambient room light, which contains strong spectral components at the desired measurement wavelengths. In principle, this background ambient signal could be measured and subtracted from the recorded sample data using un-modulated input radiation, yet ensuring this background signal remains constant for samples is difficult.

A chopper frequency of 500 hz was chosen as it was well above the frequencies of expected ambient room light. The sensitivity adjustment of the lock-in (which controls the amplification of the input signal) was varied as a function of wavelength to maintain an output signal between 200-1000 mV. This was necessary due to varying spectral flux of the optical illumination and detector response. The lock-in amplifier integration constant was set to a value of 1.0 sec. This value appeared adequate in terms of filtering unwanted noise in the output signal, yet allowed the output signal to respond to changes in the detector signal amplitude decreasing the measurement time switching between wavelengths.

Measurement Procedure

As the samples were mounted internal to the integrating sphere, the samples were aligned ensuring the incident beam under-filled the sample using the 2D translational stage. This process required removal of the top half of the integrating sphere.

Sample measurements were performed by manually scanning through monochromator center wavelengths, and recording the measured lock-in DC signal at each wavelength. For all cases, the monochromator slit width was set to 0.5 mm. Measurements were first made on the reference near unity refectivity sample, with adequate lock-in sensitivity values set at each wavelength as described above. The same sensitivity settings for each wavelength were used for all subsequent samples. An effective dark background signal without incident light was measured prior to each set of sample measurements, and subtracted from all the resulting sample data. The sample reflectivity plus transmission was calculated from the ratio of the signal with the sample versus the reference installed, and scaled to the known reflectivity plus transmission of the reference sample. Two near-unity reflectivity reference samples were used in the measurements: a silver coated substrate, and a painted glass slide (Labsphere 6080 paint). In the case of the silver substrate, the values were scaled based on the calculated fresnel reflectivity (assuming no transmission), [15] while in the case of the white paint sample it was assumed that any non-reflected component was transmitted and also captured by the sphere walls, thus no scaling was

performed. The sample absorption was calculated as one minus this quantity.

Chapter 4

Results and Discussion

A key requirement of efficient solar cell operation is high absorption of the incident solar spectrum. This chapter investigates the absorption achievable with the two novel silicon microwire designs introduced in chapter 1. The first arrangement consists of vertically-aligned wires in a 'forest' geometry combined with a conical cavity produced via HF etching, while the second consists of horizontally aligned wires in a 'log' geometry. Both these structures have the potential to use lower purity silicon by employing a radial junction, and improve material utilization through a reduced fill fraction and in the horizontal alignment, reduced kerf loss. However, the reduced fill fraction implies achieving high absorption becomes more challenging, motivating the investigations conducted here.

The absorption of these two structures was investigated through modeling (both structures) as well as experimental absorption measurements (horizontally-aligned structure). These results are divided up into two sections focusing on the two geometries independently. A general discussion section relevant to both is included at the end of the chapter.

4.1 Forest geometry with light-trapping cone

Considering the cone geometry shown in Fig. 4.1 a.) there are a number of geometrical parameters that influence the general shape of the structure. These include the

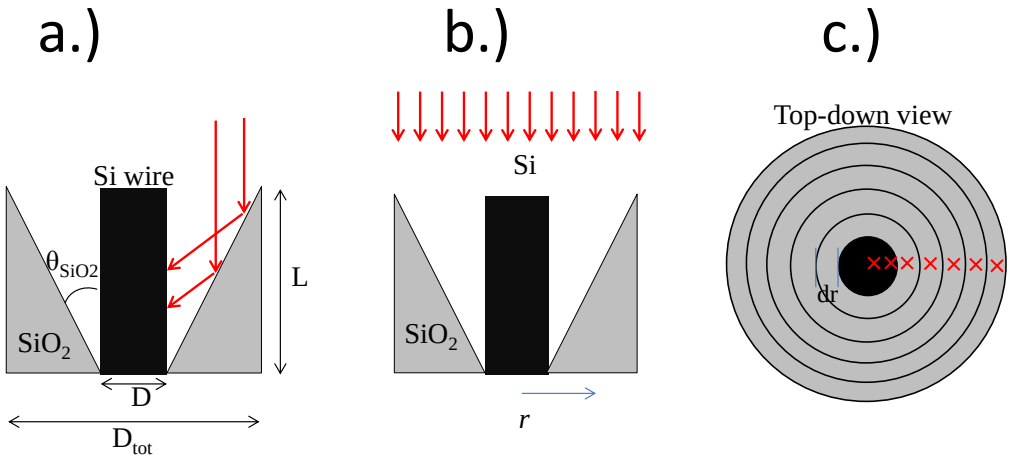

Figure 4.1: a.) Diagram of the cone structure, showing the various geometrical parameters. b.) Rays (denoted as red arrays) are launched as a function of position across the top of the cone structure. c.) A top view of rays launched at normal incidence, where radial symmetry allows the 2D code to be utilized, and a radial integral can be performed to calculate the total absorption.

angle of the cone relative to the wire axis θ_{SiO2},diameter D, and length L. Furthermore, an outer diameter D_{tot} of the conical cavity can be defined that is a function of D, θ_{SiO2}, and L. The fractional area or fill fraction F_{area} of the wire as viewed from above is then $(D/D_{\mathrm{tot}})^2$. This can also be considered the volume fill fraction compared to a planar cell of thickness L. All these geometrical parameters could potentially be controlled in the design, thus warranting a thorough investigation into their respective influence on the absorption of the structure. Assuming specular surfaces, the ray tracing code was used to model the absorption as a function of these parameters. This modeling gives useful information into the general scalings as well as design strategies to optimize the absorption. Reproducibility of the etch cone profile proved to be difficult to achieve in practice, thus experimental measurements were not conducted here. Further research is necessary to improve the quality of the HF-etched cones. This section presents the results from the ray modeling as a function of cone angle, wire diameter, fill fraction, optical wavelength, and angle of

incidence.

A single-element structure was used in the code, with rays being launched vertically from the top as shown in Fig. 4.1 a.) The optical constants (refractive index and absorption coefficient) of silicon were used for wire, while varying assumption concerning the cone surface were made (described below). The total absorption was calculated as an integral of the absorption of each ray launched as a function of position across the top of the array spanning D_{tot} (Fig. 4.1 b.)). For rays launched a normal incidence (parallel to the wire axis), the geometry is radially symmetric, thus the 2D code could be used with radial integration. Off-axis rays required the 3D code, and a grid of launched rays that spanned the circular region of diameter D_{tot}. It is notable that a potential solar cell would likely consist of an array of many of these conical elements close packed. Assuming cylindrical elements, there is a fractional area gap of $> 9\%$ due to gaps between the cylinders. The absorption values presented in this section do not include this factor.

In the first part of this section, the absorption at single wavelength of 900 nm was modeled. This wavelength was chosen as it is an intermediate wavelength between the visible regime where absorption occurs over a very short (few micron) path length, and near bandgap wavelengths where absorption occurs over hundreds of microns. A 900 nm wavelength has an absorption length of $\approx 26\mu$m which is the same order as the wire diameters considered here. It was thus assumed that this wavelength was best suited for investigating the general absorption scaling of this structure, since the absorption would be sensitive to the wire diameter as well as other geometrical parameters. Wavelength dependent results are presented later in this section.

4.1.1 Cone angle and reflectivity scalings

The conical cavity is the key element enabling potential high optical absorption of the structure. We consider here the absorption in terms of the cone design parameters, namely the angle θ_{SiO2} and the reflectivity of the surface. The angle could

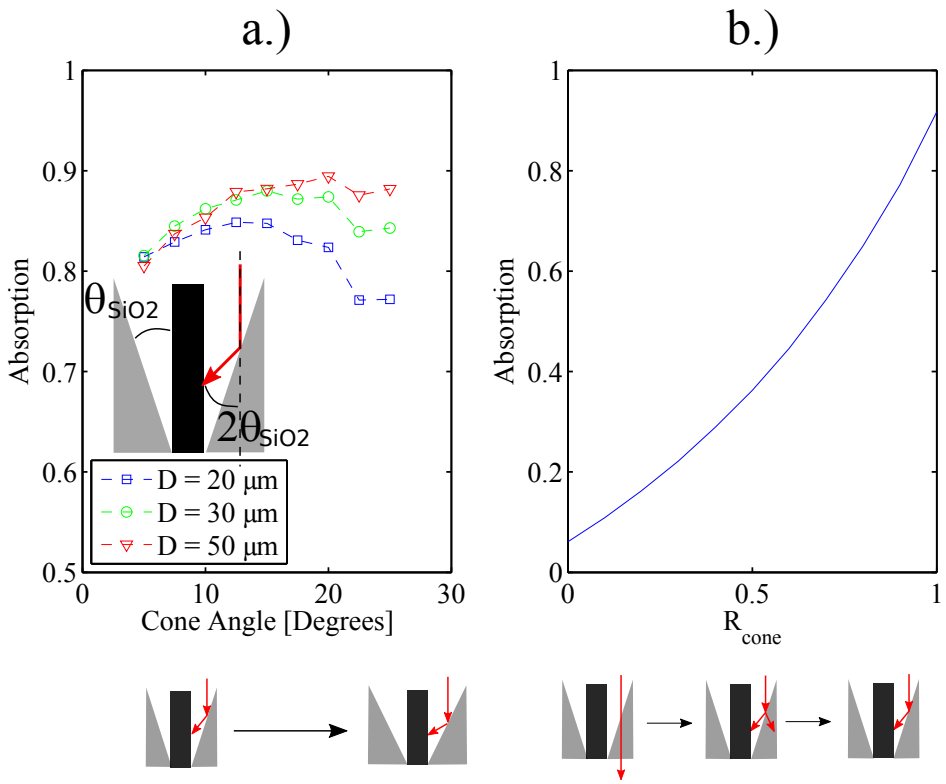

Figure 4.2: Modeled absorption at 900 nm wavelength for wires with L = 125 μm. **a.)** Absorption as a function of the etch cone angle, θ_{SiO2} for various wire diameters. The inset shows the $2\theta_{\mathrm{SiO2}}$ increase to the ray angle relative to the wire axis after each bounce off the cone surface. **b.)** Absorption vs. the cone surface reflectivity R_{cone}, assumed to be independent of angle of incidence.

potentially be controlled the HF etching dynamics (namely the relative etch rates of the calcium oxide layer relative to the silica), while the reflectivity could be controlled by applying different coatings to the cone surface.

The absorption of 900 nm wavelength incident rays as a function of cone angle θ_{SiO2} is shown in Fig. 4.2a.) for various wire diameter values D assuming normal incidence and an idealized perfectly reflecting ($R = 1$) cone surface. The general shape of the curves can be understood by considering the interplay between two competing influences. First, each bounce from the cone surface increases the ray angle relative to the horizontal direction by $2\theta_{\mathrm{SiO2}}$ as shown in Fig. 4.2 a.). The

number of bounces from the cone surface and incident on the wire is thus approximated by $\pi/2\theta_{\mathrm{SiO2}}$. This results in a decreased coupling of rays into the Si sections for larger angles. On the other hand, the area fill fraction of the wire top surface decreases with increasing cone angle. Since rays incident on the cone section are more effectively coupled into the wire compared to rays incident on the wire top surface due to multiple bounces, a lower fill fraction due to increasing cone angle tends to yield higher absorption. The interplay between these two competing factors explains the curves in Fig. 4.2 a.): at low θ_{SiO2} values the absorption increases with cone angle as the fill factor decreases, until the effective number of bounces becomes significantly few, causing the absorption to roll off. However, these factors do not have a significantly large effect on the absorption, which remains within $\sim$5% absolute over the range of angles shown. As expected, the absorption tends to be lower for smaller diameter wires, due to decreased absorption per pass through the wire.

The assumption of a perfectly reflecting cone surface is of course idealized. Fig. 4.2b.) shows the absorption as a function of the cone surface reflectivity $R_{\mathbf{cone}}$ for $D = 30$ μm, and $\theta_{\mathrm{SiO2}} = 15°$. In this case, $R_{\mathbf{cone}}$ was assumed to be independent of incident angle. Though rays undergo multiple bounces off the cone surface, the performance is roughly linear with the reflectivity value. This plot highlights the importance of a near unity value of R_{cone} for the performance of the structure. In practice, a high reflectivity could be achieved by depositing a metallic coating (such as silver) on the cone surface. To model a silver coating, the silver optical constants (with $R \approx 0.97$ over most wavelengths and angles of incidence) were assumed in subsequent modeling.

In summary, the etch cone angle determines the number of bounces from the cone surface and thus the effective coupling strength of the cone. However, good coupling resulting in $> 80\%$ absorption at 900 nm with a ideal cone reflectivity is achievable over a wide range of cone angles, an advantage since achieving a precise cone angle is likely to be challenging experimentally. Furthermore, the results highlight the importance of a near-unity reflectivity cone coating in achieving high absorption

values in the silicon. Silver is thus an example of an optimal choice for a metallic coating.

4.1.2 Wire diameter and fill fraction

Rays reflecting from the cone surface tend to enter through the sides of the silicon wire. Predictably, just as wafer thickness is an important parameter for the absorption of planar cells, the wire diameter is analogously of importance for this structure. In addition, the cone structure has the potential to achieve high absorption while using less volume of material. The degree of material reduction in general is quantified by the fill factor. These two parameters are investigated here.

Fig. 4.3 shows the absorption as a function of wire diameter assuming various area fill factors, F_{area}, which can be expressed as:

$$F_{\text{area}} = \left(\frac{D}{D + 2L \tan \theta_{\text{SiO2}}} \right)^2 . \tag{4.1}$$

In maintaining a fixed F_{area} value as a function of D, the height L was kept constant at 125 μm and θ_{SiO2} varied in Fig. 4.3a.), and visa versa in b.) with $\theta_{\text{SiO2}} = 15°$. As expected, the absorption increases with wire diameter value with an asymptotic behavior as the diameter becomes significantly larger than the absorption length at 900 nm. The exception is the F_{area} case in Fig. 4.3a.). Here, θ_{SiO2} becomes large to preserve a fixed fill factor, thus reducing the number of passes through the wire section as described in the analysis of Fig. 4.2a.). The other notable trend in both plots is the slight increase in absorption as the fill factor becomes smaller, since light is more effectively coupled into the wire through multiples bounces from the cone section, as opposed to a single bounce from the wire top surface.

In general, absorption of nearly 90% is achievable for most geometries with wire diameters exceeding 20 μm, despite a low fill fraction of silicon. As an example of a comparison to planar cells, the $F_{\text{area}} = 0.10$ curve in Fig. 4.3 a.) has the same equivalent volume as a 12.5 μm thick planar cell which is only roughly half the absorption length at 900 nm. This highlights the potential of the cone structure to improve material utilization.

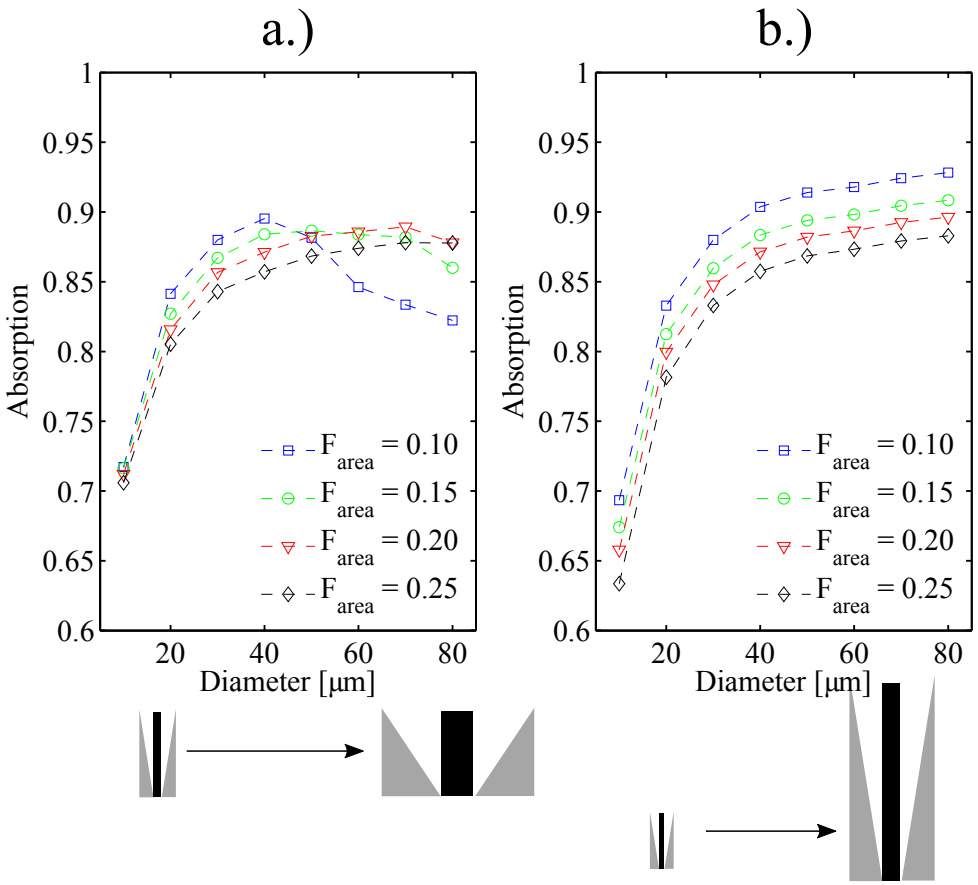

Figure 4.3: **a.)** Absorption as a function fill of wire diameter for various fill factors F_{area}, assuming a fixed wire height of 125 μm. **b.)** The same as a.), but with a fixed etch angle $\theta_{\text{SiO2}} = 15°$, and varied wire height. In both cases, the wavelength used was 900 nm.

4.1.3 Wavelength dependence

Calculating the absorption at a single wavelength yields insight into the general geometric design trends that influence the absorption. However, since the incident solar spectrum contains significant spectral flux over a range of wavelengths where the silicon optical properties (namely the absorption coefficient) change appreciably, wavelength dependent calculations are necessary to evaluate the total absorption due to incident solar radiation. The absorption as a function of wavelength for various geometries is shown in Fig. 4.4. As expected, there is a stronger diameter dependence

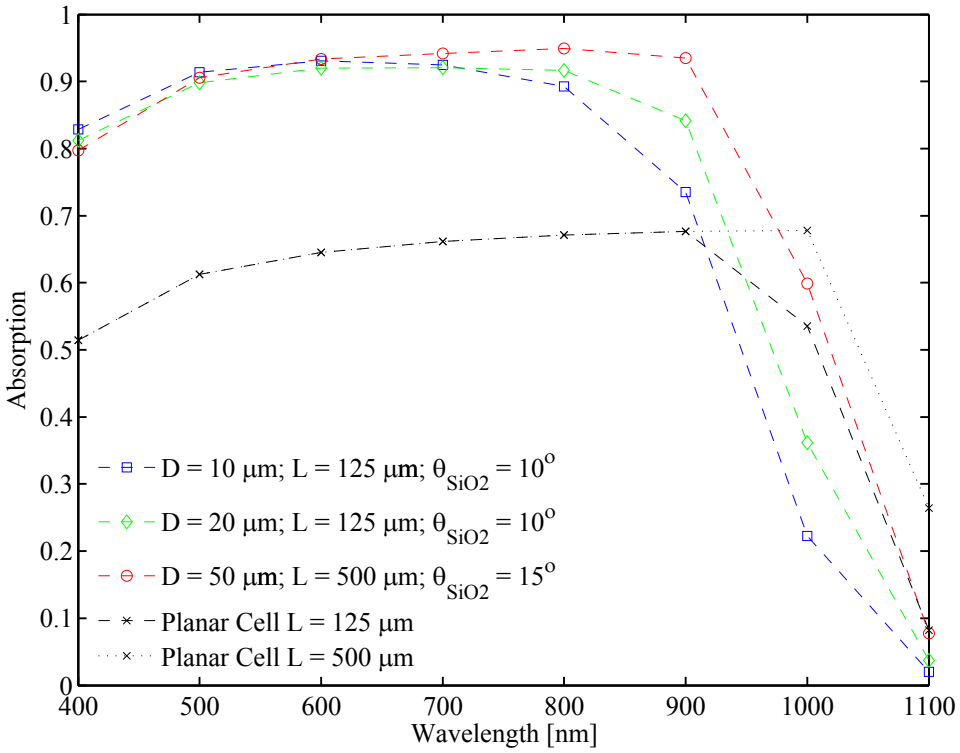

Figure 4.4: Absorption as a function of wavelength for various geometries. A comparison to planar cells is also shown.

at longer wavelengths as the absorption coefficient deceases. At shorter wavelengths (400-600 nm), the absorption falls off due to increased Si surface reflectivity. A comparison to planar cells is also shown in Fig. 4.4.

Fig. 4.5 shows the fractional absorption integrated over the AM1.5D solar spectrum for photon energies larger than the bandgap. The AM1.5D spectrum was chosen as it includes only the collimated direct component of solar radiation, relevant here for use with the ray model. Total absorption over 80% is possible for larger wire diameter and height values, and remains $\sim 70\%$ for short diameters. The integrated absorption serves as an upper bound for the external quantum efficiency of a solar cell device utilizing the cone geometry.

This structure enables a high fractional absorption of incident photons compa-

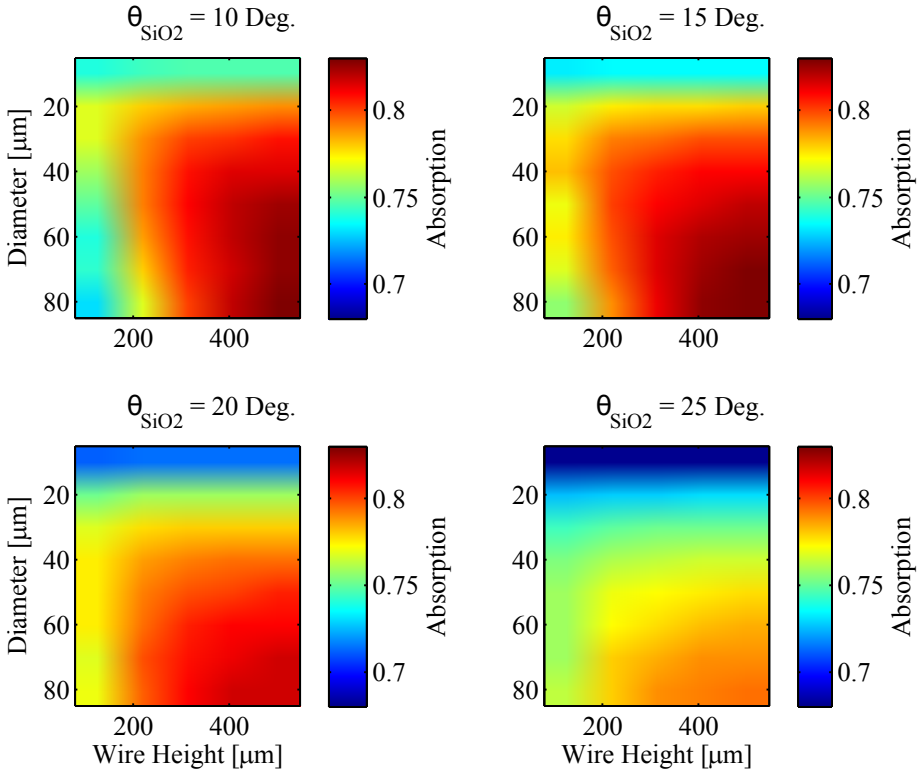

Figure 4.5: Total absorption (shown in the color bar) integrated over the solar spectrum for various etch cone angles θ_{SiO2}, as a function of wire diameter and wire height.

rable to an equivalent planar geometry. Due to the small silicon fill fraction, this results in a higher density of absorbed photons and thus excited charge carriers per volume of silicon. Though the surface area-to-volume ratio of the wires is larger than that of a planar cell, the higher carrier density can lead to an increased short circuit current J_{sc} across the junction area for certain cone geometries. The junction area of the wire is assumed to be the sum of the top surface and side surface:

$$A_{\mathrm{jct}}^{\mathrm{wire}} = \pi D^2/4 + \pi DL,$$

while the junction area of an equivalent planar cell is:

$$A_{\mathrm{jct}}^{\mathrm{planar}} = \pi D_{\mathrm{tot}}^2/4 = \pi \left(D + 2L\tan\theta_{\mathrm{SiO2}}\right)^2/4.$$

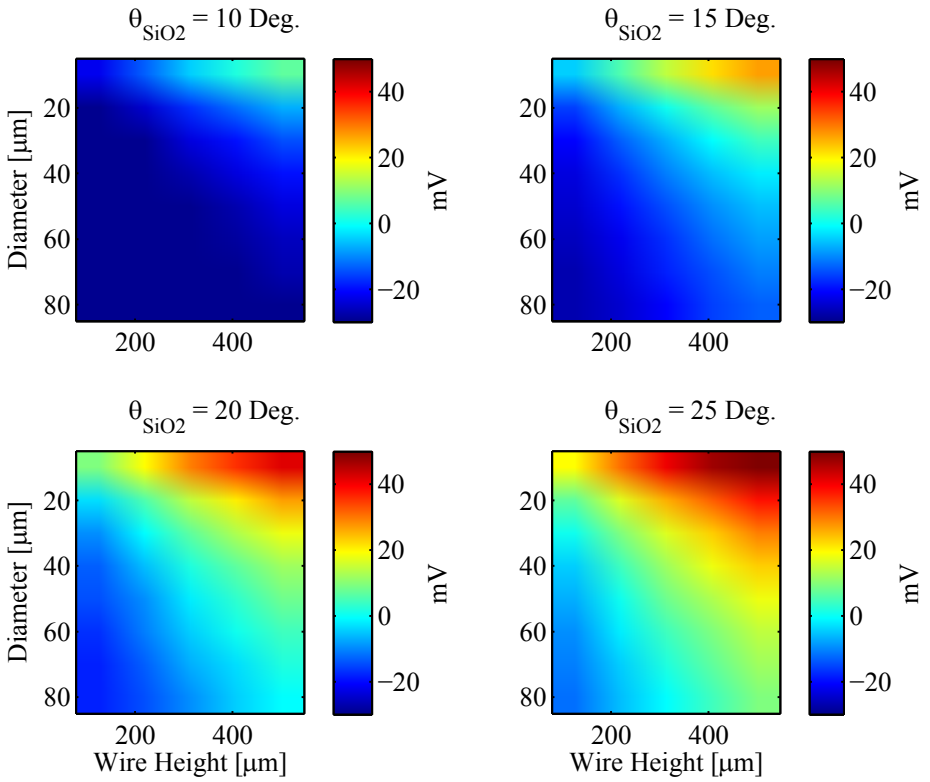

Figure 4.6: The change in V_{oc} due to a higher short circuit current density is shown in the colorbar as a function of wire diameter and height.

Assuming comparable absorption between a planar cell and the cone structure, J_{sc} will be higher in the cone geometry if $A_{jct}^{wire} > A_{jct}^{planar}$. Specifically, the short circuit current density of the cone structure J_{sc}^{cone} can be expressed in terms of the current of an equivalent planar device J_{sc}^{planar} that absorbs 100% of the sub-bandgap solar radiation:

$$J_{sc}^{cone} = \frac{f_{ABS} J_{sc}^{planar} A_{jct}^{wire}}{A_{jct}^{planar}}, \tag{4.2a}$$

$$J = X J_{sc}^{planar}, \tag{4.2b}$$

where f_{ABS} is the fractional absorption of the cone structure and $X \equiv \frac{f_{ABS} A_{jct}^{wire}}{A_{jct}^{planar}}$.

This could lead to an increased open circuit voltage, since $V_{oc} \propto \ln\left[\frac{J_{sc}}{J_0} + 1\right] \approx$

$\ln\left[\frac{J_{sc}}{J_0}\right]$. The quantity $\frac{k_B T}{q}\ln[X]$ is shown in Fig. 4.6 for the same range of parameters. This represents the change in V_{oc} relative to an equivalent planar cell with 100% absorption. The fractional increase in V_{oc} is in general more complicated as it is also dependent on the dark current parameter J_0. In general, the regions with highest gains in V_{oc} have the lowest fractional absorption, referring to Fig. 4.5. This implies that these gains may not result in a higher device efficiency. It is however notable that the increased excited carrier density overcomes the inherent higher surface area-to-volume ratio of a radial junction wire geometry under some geometries, especially for higher cone angles. The cone structure thus acts as an effective solar concentration system.

The wavelength integrated absorption confirms the results of the previous single wavelength modeling, indicating high absorption potential of total incident solar radiation. In addition, effective concentration due to the cone surface overcomes the inherent parasitic geometrical effect of reduced short current density for radial junctions, and a slight increase in open circuit voltage may be possible.

4.1.4 Angle of incidence

Up to this point, all modeling has assumed solar radiation at normal incidence. Since the sun moves across the sky over the course of the day, evaluating the performance over multiple angles of incidence is relevant. Solar tracking systems can be implemented to maintain a near-normal incidence, but these are costly and are not practical in all situations. The absorption of the cone structure as a function of angle of incidence θ_{inc} was modeled using the 3D version of the ray tracing code developed in MATLAB. This is shown in Fig. 4.7 a.) for various geometries and wavelengths. Design 1 ($D = 80\mu\text{m}; L = 500\mu\text{m}; \theta_{SiO2} = 10°$) maintains absorption near 90% out to incident angles $\sim 20°$, with similar values for both 700 and 900 nm due to the large wire diameter. The absorption begins to decrease at smaller angles of incidence of $\sim 10°$ for Design 2 ($D = 20\mu\text{m}; L = 125\mu\text{m}; \theta_{SiO2} = 15°$). This occurs for both wavelengths, implying it is not a result of the smaller wire diameter

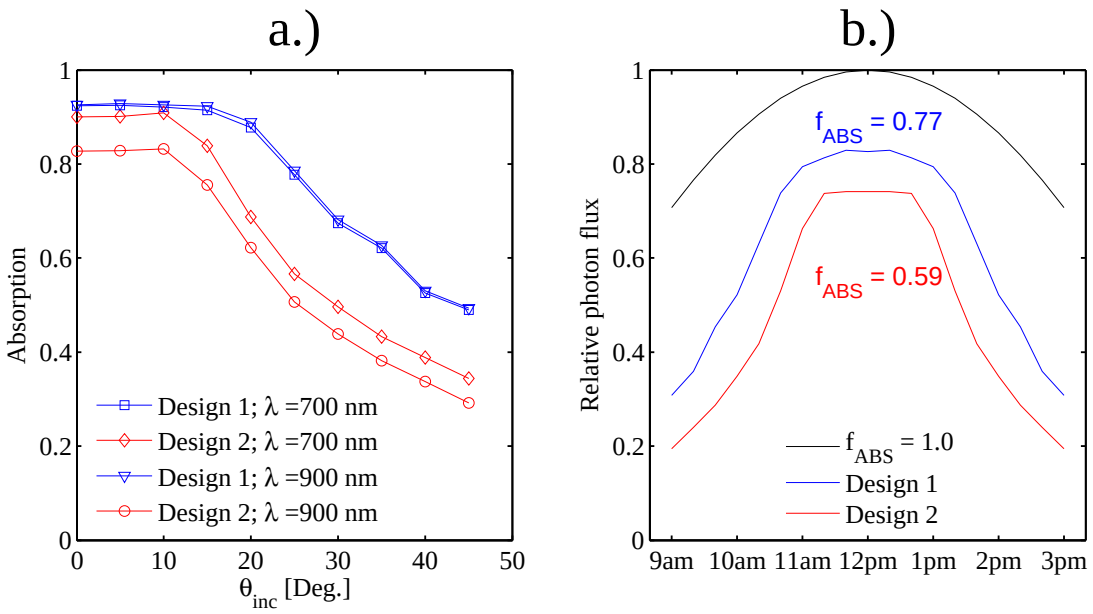

Figure 4.7: a.) Absorption as a function of incident angle. Design 1 has $D = 80\mu\text{m}; L = 500\mu\text{m}; \theta_{\text{SiO2}} = 10°$, while Design 2 has $D = 20\mu\text{m}; L = 125\mu\text{m}; \theta_{\text{SiO2}} = 15°$. b.) Relative photon flux as a function of time of day. The labeled f_{ABS} is the fractional absorption integrated over the day from 9am to 3pm.

but instead due to the smaller fill fraction of design 2 compared to design 1 (5.3% vs. 9.7%).

The performance of the cell over the course the day was evaluated by assuming the angle of incidence varies at a rate of 15°/hr with normal incidence occuring at 12pm noon, and $\theta_{\text{inc}} = 45°$ occurring at 9am and 3pm. Furthermore, it was assumed the photon flux scales as $\cos\theta_{\text{inc}}$ for all wavelengths due to oblique incidence. It is important to note these are both simplified assumptions as the angular movement of the sun is latitude dependent, and absorption and scattering in the atmosphere result in a more complicated wavelength dependent functional scaling of the photon flux. The wavelength integrated relative absorbed photon flux as a function of time of day (thus θ_{inc}) is shown in Fig. 4.7 b.) between 9am and 3pm. Also noted in the figure is the total fractional integrated current over the whole day relative to a device with 100% absorption. Design 1 absorbs 77% of incident solar radiation over the day

length shown in Fig. 4.7 b.), while design 2 absorbs 59%. The discrepancy is due both to the smaller wire diameter of design 2 which limits infrared absorption, as well as the smaller fill fraction which leads to decreased absorption at larger angles of incidence.

4.1.5 Discussion

The modeling presented in this section highlights the potential of the cone geometry to absorb nearly 90% of solar radiation up to 900, with this high absorption achievable for a wide range of geometrical parameters allowing for flexibility in the design. The day-integrated value of 77% presented above approaches the value of 85% reported by Kelzenberg *et al.* for vertically-aligned wires embedded in PDMS with scattering centers. [21] The wire height-to-diameter values in that study were greater than 10:1, whereas design 1 above is 6.25:1. The modeled absorption for the cone geometry indicates that near 80% day integrated absorption is possible for wires of lower aspect ratio. This decreases the degree of parasitic effects on device performance especially due to potential surface recombination, thus likely to lead to higher open circuit voltages. However, the material reduction is significantly less than in Kelzenberg *et al.* where the effective planar thickness was 2.8 μm compared to 50 μm for design 1.

The cone geometry does perform better than a planar geometry of untreated silicon in air which suffers $\sim$30% reflection losses. The solar industry combats this loss with anti-reflective (AR) coatings, which could also be applied to the microwires in this cone structure. These coatings would further increase the absorption of the cone geometry, potentially making the design more competitive to the results of Kelzenberg *et al.* where an AR coating is also applied to the wires. This represents an area of potential further investigation for the cone geometry.

4.2 Horizontally Aligned Si Microwires

The majority of research on radial junction devices has focused on vertically aligned wire arrays. Most growth techniques favor vertical wires, and the absorption potential of these vertical wire arrays has been well documented. However, for the larger diameter and longer length wires made using the molten core fiber drawing method the horizontal alignment also warrants consideration. The diameters are large enough such that notable absorption is achieved through one pass at most wavelengths, and the relatively long wire lengths ($\geq$ cm) allow for continuous segments to be placed next to each other with the wire length serving as an areal dimension of the solar cell.

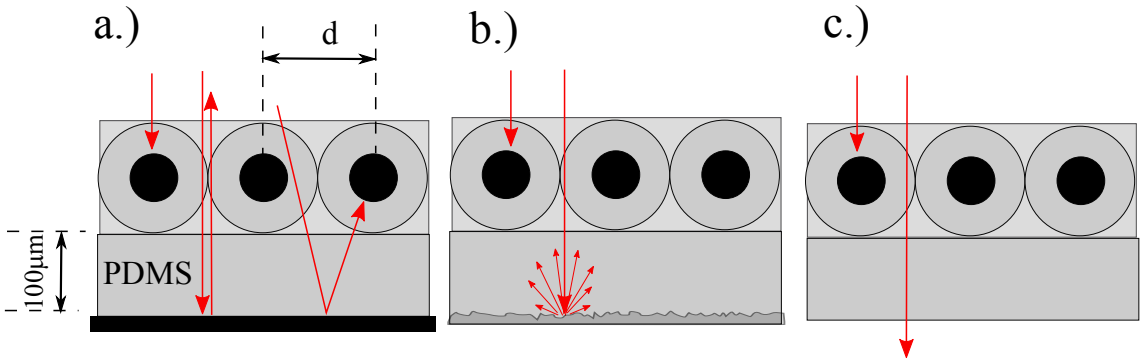

Figure 4.8: Three horizontally-aligned wire designs featuring different backreflector types: a specular substrate (a.)), lambertian substrate (b.)), and no backreflector (c.)).

This section presents modeling and experimental measurements for horizontally aligned Si microwire arrays. Three different sub-designs were considered with different backreflectors as shown in Fig. 4.8. The first has a specular backreflector with near unity reflectivity (Fig. 4.8 a.)). For normal incident rays, the backreflector has little effect in terms of directing rays into the silicon wire sections, as rays not intercepting the wires on the first pass tend to exit the structure after reflection from the backreflector. However, rays incident off-axis can intercept the wires after reflecting from the specular substrate as shown. A potential alternative design fea-

tures a lambertian (diffuse) backreflector, where normal incident rays reflected from the backreflector travel in all directions (Fig. 4.8 b.)) and can intercept the wires. Both these designs aim to maximize the absorption in the wires, and the structure is non-transparent. For potential applications as semi-transparent solar cells, a third design without a backreflector was also considered (Fig. 4.8 c.)). In this case, light rays not intercepting the wires on the first pass through the array will tend to be transmitted through as shown.

4.2.1 Modeling

The primary geometrical parameters influencing the design above are the wire diameter and center-to-center distance d, warranting investigation here. For convenience, a fill factor $F \equiv \frac{D}{d}$ was defined (for wire diameter D). For traceability to assembled arrays which were measured experimentally, it was assumed the wires were surrounded by a silica cladding and epoxy with the cladding thickness determining d, and the arrays were attached to a $\approx 100\mu$m thick PDMS layer. The distance from the wire center to the backreflector was thus $d/2 + 100\mu$m, as shown in Fig. 4.8. For simplicity, the silica, PDMS, and epoxy were all assumed to have a refractive index $n = 1.5$.

The ray tracing code was used to investigate the absorption dependence on various parameters for the specular backreflector, assumed to be a silver coated substrate. Rays were launched as a function of position in the direction perpendicular to the wire lengths. In addition to dependence on the diameter and fill fraction, the absorption was also expected to be a function of angle of incidence for this design as described previously (see Fig. 4.8 a.)). Since the horizontal wire alignment is not radially symmetric, the angle of incidence must be defined with respect to two coordinate axes, chosen here as the wire axis and the perpendicular direction as shown in Fig. 4.9. For angles of incidence in the $\perp$ direction, the 2D code could be used with the wire surfaces represented as circular regions while for the $\parallel$ orientation, the 3D code was necessary.

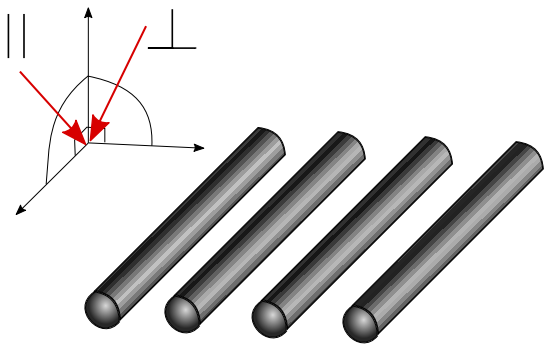

Figure 4.9: A diagram of showing the two sample orientations measured. The angle of the incident light in the $\perp$-orientation is in the plane perpendicular to the wire axis, while in the $\parallel$-orientation the light makes angle in the plane parallel to the wire lengths.

The modeled absorption as a function of wire diameter and fill factor is shown in Fig. 4.10 for wavelengths of 600, 900, and 1000 nm and incident angles θ_i of 0° and 15° in the $\perp$ direction. As may be expected, there is very little diameter dependence at 600 nm where the absorption length is short, with a stronger dependence at longer wavelengths. Furthermore, the absorption is generally increased for all cases at a non-normal incident angle, as rays reflecting from the backreflector can intercept the wires on the second pass. Near unity absorption despite the $\sim 20\%$ fresnel reflectivity of a silica-silicon interface is achieved for shorter wavelengths as the $F \rightarrow 1$. This is due to the tendency of the reflected components from the curved wire surfaces to intercept adjacent wires. In general, the absorption scaling follows intuition: a diameter dependence analogous to planar cells, and monotonically increasing as a function of fill factor.

The absorption values calculated above at finite angle of incidence assume rays making an angle in the $\perp$ direction as denoted in Fig. 4.9. To further investigate the dependence on angle of incidence, the absorption was calculated as a function

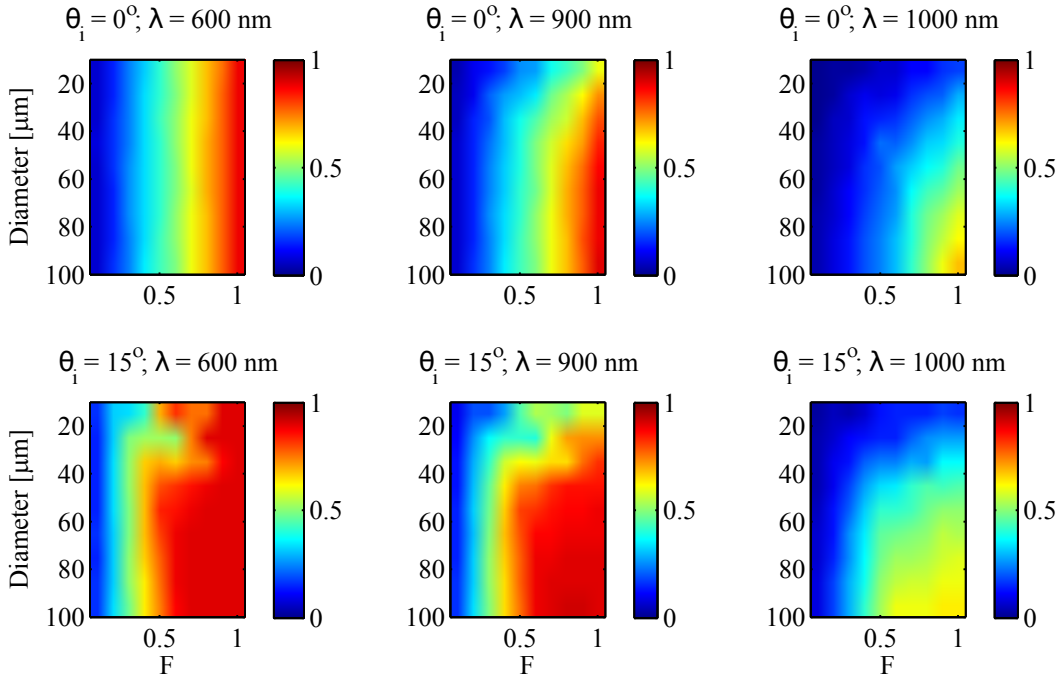

Figure 4.10: Modeled absorption as a function of wire diameter D and fill fraction F for various wavelengths λ and angles of incidence θ_i. For ease of viewing a finer grid is displayed, interpolating between calculated values at various D and F values.

of angle of incidence in both orientations for a single geometry with $D = 50\mu$m, $F = 0.25$, and $\lambda = 900$nm. The results are shown in Fig. 4.11. For the $\parallel$ orientation, there is negligible dependence on the angle of incidence since the ray angles are in the plane parallel to the wire lengths, implying that reflections from the backreflector do not direct the rays towards the wire segments. In this case, the absorption is roughly the fill fraction multiplied by the fresnel transmission into silicon ($\sim 80\%$). On the other hand, the absorption for the $\perp$ orientation tends to increase as a function of θ_i up to $\approx 20°$, with a maximum value of approximately twice that at normal incidence. At these angles the backreflector effectively acts to double the number of rays that intercept the silicon wire sections.

The ray model yields general information into the design trends of the horizontal

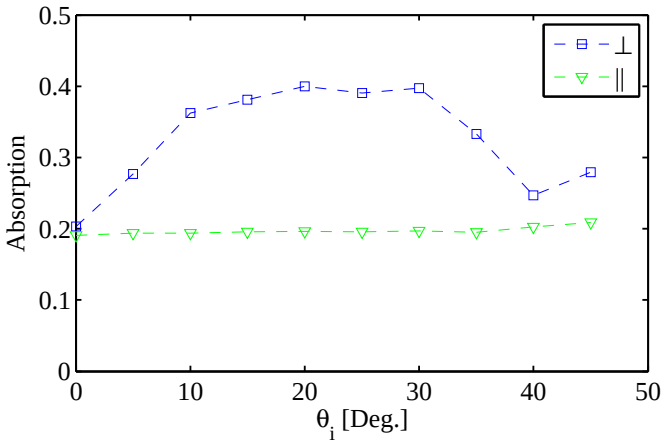

Figure 4.11: Modeled absorption as a function of angle of incidence θ_i in both the $\perp$ and $\parallel$ directions.

geometry, especially relevant to the specular backrelfector, yet assumes all surfaces are specular which of course is an idealized assumption. Rough wire surfaces and irregularities in the silica-epoxy interface could cause rays to become somewhat randomized. In addition, to model the structure in Fig. 4.8 b.) a different technique is necessary to account for reflections from the lambertian backreflector. To model the structure in the case of randomized rays, the analytical statistical model from Yablonovitch [18] described in section 2.2.5 was used. This model assumes isotropic radiation to derive a simple relation for the fractional absorption in the strongly absorbing (short wavelength) regime (Eq. 3.8):

$$f_{\mathrm{ABS}} = \frac{A_{\mathrm{Si}} T_{23} T_{13}}{\bar{T}_{13}/n_3^2 + A_{\mathrm{Si}} \bar{T}_{23}}.$$

In this case, the fractional area of the Si wires relative to the area of incident radiation is $A_{\mathrm{Si}} = \pi F$. The curve shown in Fig. 4.15 assumes transmission coefficients $\bar{T}_{23} = 0.78$, $\bar{T}_{13} = 0.96$, and $n_3 = 1.5$.

However, this statistical model also relies on the idealized assumption that rays are completely randomized within the structure. There is likely some degree of anisotropy, and as Yablonovitch pointed out, absorption can take place before ran-

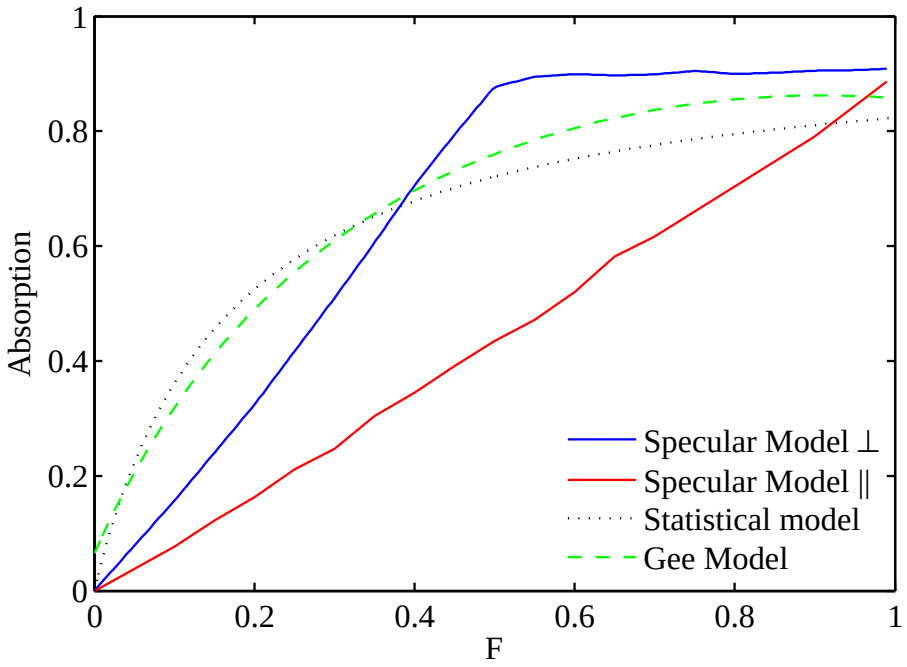

Figure 4.12: Modeled absorption as a function of fill factor F for the ray tracing code (specular model assuming $\lambda = 750$ nm and $\theta_i = 15°$, as well as the statistical model and the Gee model.

domization occurs. [18] This motivates the use of a third model, the self-consistent Gee approach [39] described in section 3.1.3 for strongly absorbing wavelengths, which does not rely implicitly on either of these assumptions. The model parameters $R_{\text{ext}} = 0.04$, $R_{\text{array}} = 0.22F$, $T_{\text{array}} = 1 - F$, $R_{\text{int}} = 0.57$, and $R_{\text{br}} = 0.98$ were assumed here.

A comparison of the three models is shown in Fig. 4.12, for $\theta_i = 15°$ and $\lambda = 750$nm in the case of the ray tracing code (the other models shown here don't have a dependence on wavelength and angle of incidence). At low fill fractions the statistical model predicts the highest absorption, as ray randomization increases the probability of rays intercepting the wires for sparsely-packed arrays. The opposite trend occurs at larger fill fractions, where ray randomization becomes a somewhat

parasitic effect compared to $\perp$ specular ray model curve. As may be expected, the Gee model is roughly bounded by the other two models over most fill factors (for the $\perp$ orientation) as it treats the somewhat intermediate case of quasi-random rays.

These three models were used to better interpret the experimental results shown in the next section.

4.2.2 Experimental Measurements

Silica-clad wires were fastened together using epoxy and mounted on a PDMS film as described in the previous chapter, and shown in Fig. 4.8. The absorption of assembled samples with various fill fractions was measured using the integrating sphere setup. Measurements were conducted on samples with backreflectors representative of the three designs in Fig. 4.8: a silver coated specular substrate, white lambertian sample (Labsphere 6080 coating on glass), as well as without a backreflector. The results are presented for each backreflector configuration separately, with general discussion at the end. Absorption measurements of Si wire arrays mounted on these backreflectors are shown for different sample orientations as shown in Fig. 4.9, and in some cases light incident angles. The results were compared to the modeling techniques to evaluate the performance of the arrays as a function of fill fraction.

Example data from an irradiated sample mounted internally to the integrating sphere is shown in Fig. 4.13. Data was taken every 50 nm center wavelength (shown as the points) while the dashed lines serve as a guide for the eyes. The photodetector signal as a function of wavelength for both Si and Ge detectors was normalized in this case to a silver-coated substrate. As seen, there is reasonable agreement $\sim$ 2-3% absolute between the two detectors. This was the case for most all measurements, and in further data shown in this chapter where the wavelength range extends above 1100 nm the two signals were averaged over the overlapping regime (900-1100 nm). The signal shown in Fig. 4.13 represents the sample reflectivity, or reflectivity plus transmission depending on the backreflector configuration. The sample absorption was assumed to be one minus this quantity. The measured reflectivity was repeat-

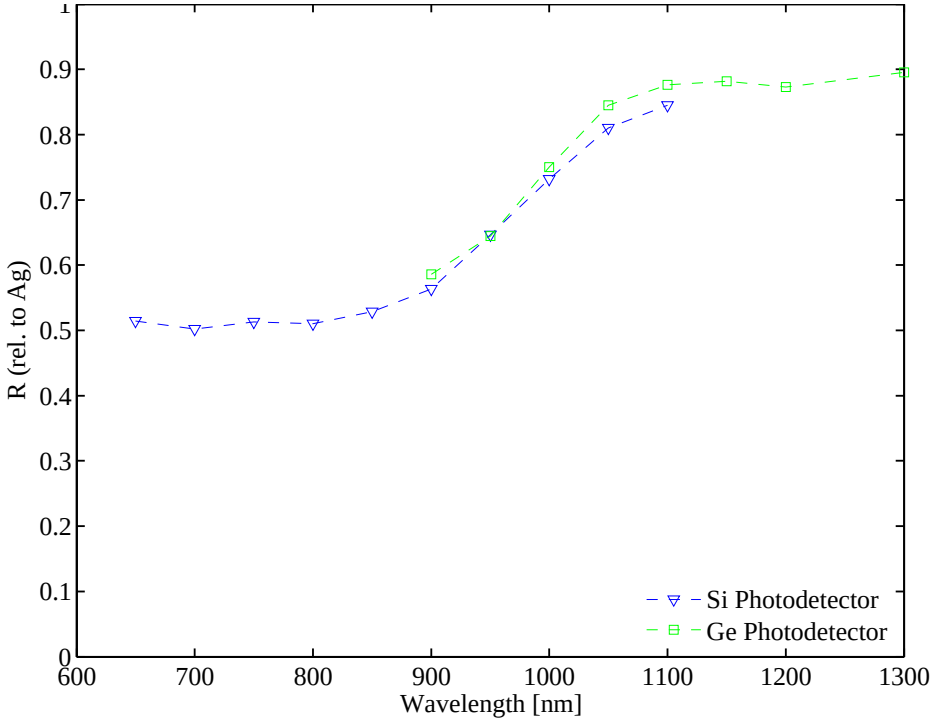

Figure 4.13: Example sample reflectivity data is shown relative to a specular Ag backreflector for both the Si and Ge photodetectors. The points indicate the wavelengths at which measurements were made, while the dashed line serves as a guide for the eyes.

able to within ±2% absolute standard deviation through multiple measurements re-inserting and aligning the samples.

4.2.3 Specular backreflector

Shown in Fig. 4.14 are the absorption values as a function of wavelength for various samples of different fill fractions F, mounted on a silver-coated specular substrate serving as a backreflector. In Fig. 4.14 a.) the samples were mounted at $\approx 15°$ relative to the incident radiation in the plane perpendicular to the wire lengths (denoted the $\perp$-orientation), as shown in Fig. 4.9. The orthogonal sample orientation, with the angle of the incident light in the plane parallel to the wire lengths ($\|$-orientation

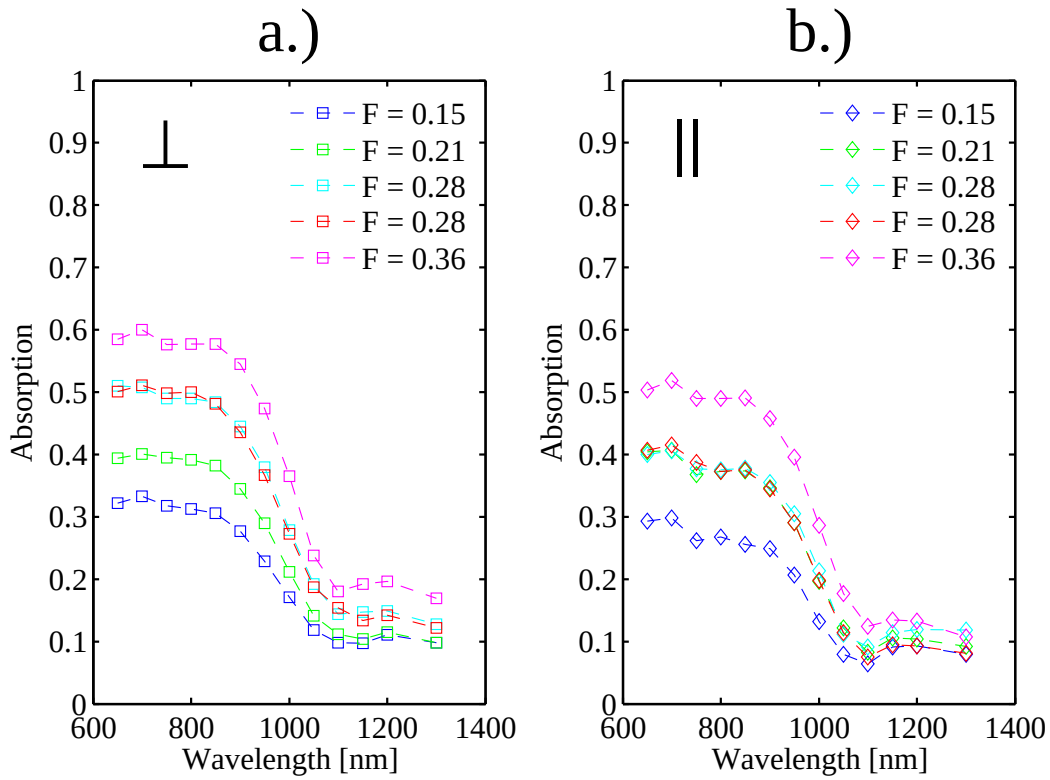

Figure 4.14: a.) Absorption for samples of various fill fractions F mounted on a silver backreflector as a function of wavelength for the $\perp$-orientation. b.) $\parallel$-orientation.

in Fig. 4.14), is shown in Fig. 4.14 b.).

At most wavelengths the absorption tends to increase with increasing fill factor. As expected, the absorption begins to fall off around 900 nm as the absorption coefficient decreases. For wavelengths above the band gap there is expected to be negligible band-to-band absorption, yet the measured absorption in Fig. 4.14 is $\sim 5-15\%$ at wavelengths 1100-1300 nm. This is suggestive of parasitic absorption processes, which include absorption in any of the other sample materials (silica, epoxy, PDMS), backreflector, or other absorption processes in the silicon wires. As this absorption tends to increase with increased fill fraction, wire absorption appears the likely to contribute. Sub bandgap absorption processes such as free carrier absorption and absorption due to defects have been reported for silicon. [41] [42] The

silicon starting material resistivity suggests dopant concentrations many orders of magnitude above intrinsic levels, yet sample absorption was shown to be $\sim$ constant out to a 1600 nm wavelength (data not shown) suggesting that free carrier absorption is negligible since the absorption coefficient has been shown to increase at longer wavelengths. [41] Thus, the most likely silicon parasitic absorption process is due to defects which create energy levels within the bandgap. [42] Parasitic absorption in the backreflector may also contribute, as the light trapping of the structure leads to multiple ray bounces off the backreflector with reflectivity $< 100\%$.

At above-bandgap wavelengths (< 1100 nm) it is difficult to de-couple the band-to-band absorption which is useful for solar cell performance from parasitic absorption. The rate for band-to-band absorption varies drastically over the wavelength range 650-1100 nm, thus the fraction of the measured sample absorption due to parasitic processes is also expected to vary. In general, the fraction of parasitic absorption is expected to be minimized at lower wavelengths since band-to-band absorption occurs over a shorter silicon path length in this regime. Given the uncertainty regarding the cause of the non-zero sample absorption at sub-bandgap wavelengths and the difficulty in decoupling parasitic absorption, no attempt was made to apply a correction to the measured absorption data. In terms of solar cell performance, the experimental values can thus be considered an upper bound on the band-to-band absorption.

A comparison to the three models described in the previous section is shown in Fig. 4.15 as a function of fill factor at 750 nm and $\theta_i = 15^\circ$. The ray model reasonably approximates the data for the $\perp$-orientation at low fill fractions, yet overestimates the absorption as F approaches unity. For the $\|$-orientation, the ray model poorly predicts the absorption, which indicates that some degree of ray-randomization is present in the structure.

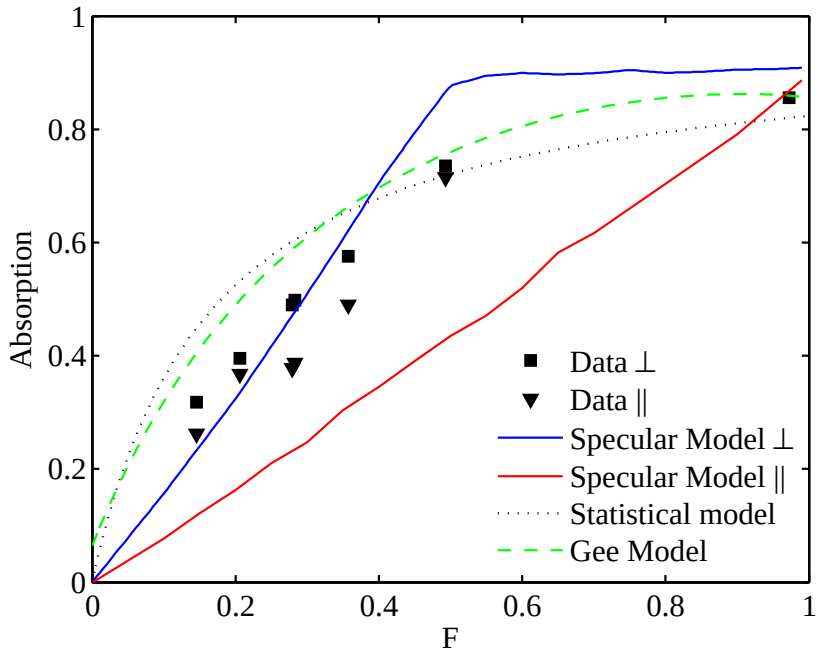

Figure 4.15: Sample absorption on a silver backreflector ($\approx 15°$ incident angle) at a center wavelength of 750 nm as a function of fill fraction F. The data is compared to modeling using the ray tracing code (specular model), as well as the statistical random model and the Gee model.

4.2.4 Lambertian backreflector

Similar results with a lambertian backreflector (Labsphere 6080 white paint coating on glass) are shown in Fig. 4.16 for an incident angle of 15° and both sample orientations. In this case there is a negligible difference between the ⊥ and ∥ sample orientations, consistent with increasing ray randomization due to the lambertian backreflector. However, in most cases the absorption is not drastically increased compared to the specular backreflector.

The Gee model approach was used to model the absorption as a function of wavelength for various fill fractions. A comparison to the experimentally measured sample absorption with a lambertian backreflector is shown in Fig. 4.17. The path length through the wires l was assumed to be 50 μm, approximately the wire di-

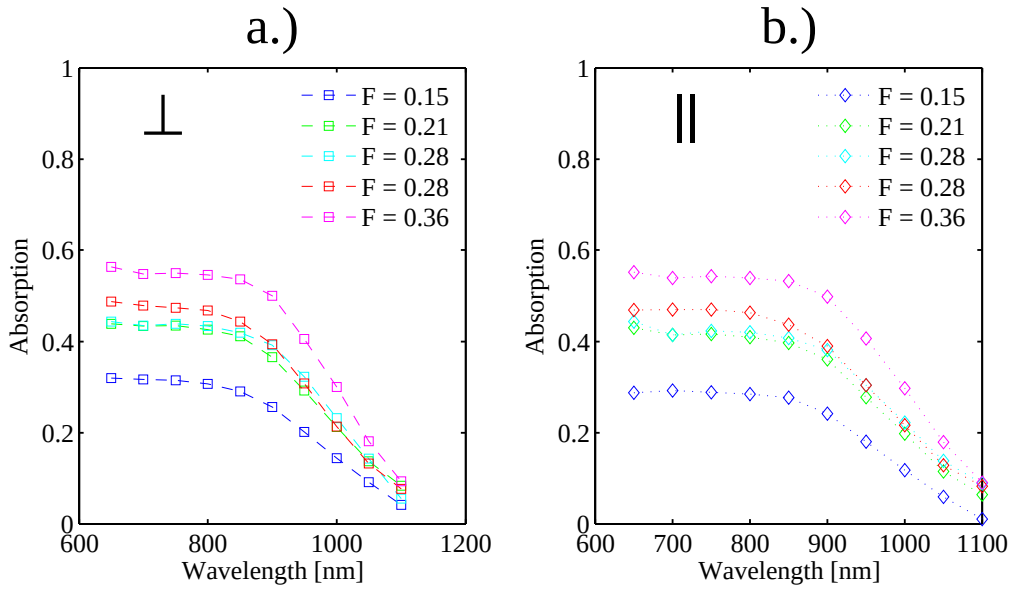

Figure 4.16: a.) Absorption for samples of various fill fractions F mounted on a lambertian backreflector as a function of wavelength for the $\perp$-orientation. b.) $\|$-orientation.

ameter for all samples. The model under-estimates the measured absorption at larger wavelengths likely due to the presence of parasitic absorption, described in the previous section. However, the general functional form of the experimental data is reproduced in the model with the simplified path length assumption.

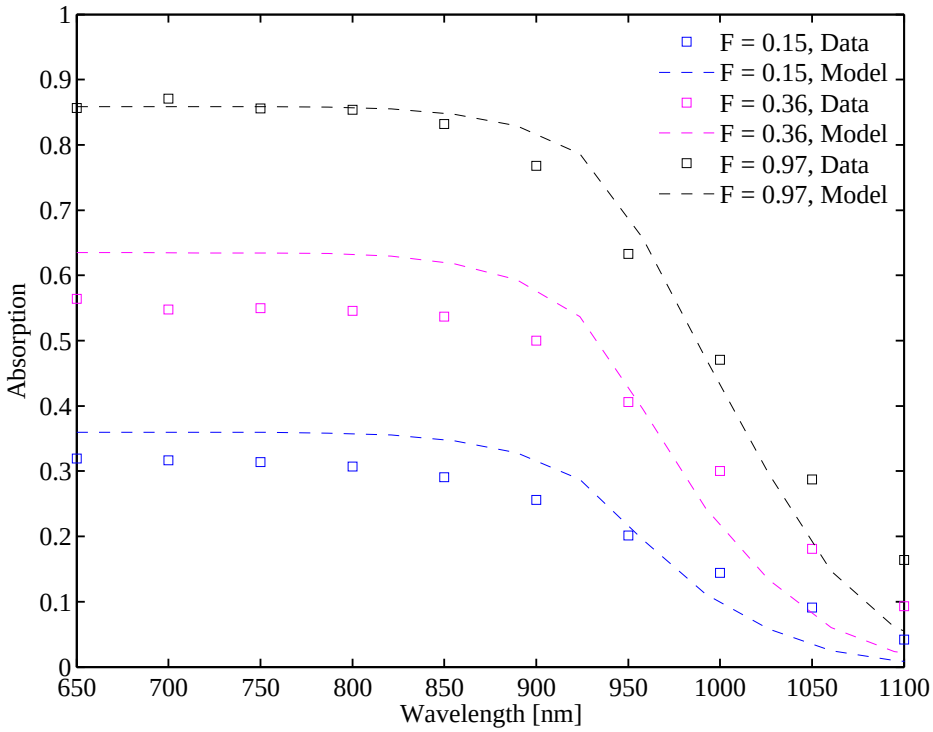

Figure 4.17: Absorption as a function of wavelength for various samples of different fill fractions mounted on a lambertian backreflector at incident angles of 15° for $F = 0.15, 0.36$ and near-normal incidence for $F = 0.97$. The dashed curves show the Gee model for these fill fractions.

4.2.5 No backreflector

For comparison, measurements were also conducted for samples without a backreflector. Horizontally-aligned microwire arrays could potentially function as semi-transparent solar cells in this case. To allow for easier comparison of the absorption dependence on fill fraction, the absorption at a single center wavelength of 750 nm is shown. In this regime, light internal to the Si wires is quickly absorbed for these wire diameters (~ 50 μm). Samples were mounted at two angles relative to the incident radiation: near normal incidence, and at a larger angle of $\sim 45°$. The results are shown in Fig. 4.18, along with the modeled absorption using the Gee model (3.1.3). The model uses the same assumptions as in section 4.2.3 in the case of the backreflector, and assumes $R_{\mathrm{br}} = R_{\mathrm{int}}$ in the case of no backreflector. The model

reproduces the qualitative behavior of the experimental data for both backreflector cases.

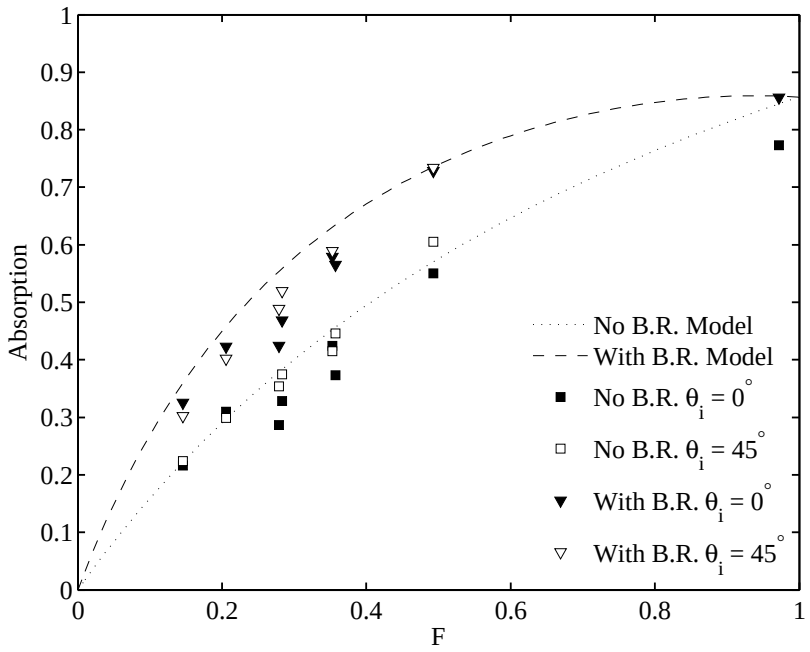

Figure 4.18: Absorption as a function of fill fraction for samples with and without a lambertian backreflector, at incident angles of 0° and 45°. The dotted and dashed are the Gee model with and without a backreflector.

4.2.6 Performance across the solar spectrum

To evaluate the total fractional absorption of the solar spectrum, the cumulative integral of photon flux absorbed by the wire arrays was calculated and multiplied by the charge constant q to find an equivalent cumulative short circuit density:

$$J_{\mathrm{csc}}(\lambda) = q \int_0^{\lambda} f_{\mathrm{ABS}}(\lambda')\phi_{\mathrm{inc}}(\lambda')d\lambda', \tag{4.3}$$

where ϕ_{inc} is the incident AM1.5G spectral photon flux. The integral was evaluated by linearly interpolating between measured absorption values to give a continuous function $f_{\mathrm{ABS}}(\lambda')$. The cumulative equivalent current density is shown in Fig. 4.19 for the same samples as shown in Fig.4.17. Eq. 4.3 was evaluated up to the silicon

band gap wavelength (assumed to be $\approx$ 1120 nm). For wavelengths below the range of measured data (650 nm), the absorption was assumed to be equal to the lowest measured wavelength for simplicity. This short circuit current density value assumes a unity internal quantum efficiency where there is no recombination current, thus an upper bound on the achievable value. The total fractional absorption of incident above-bandgap solar photons is represented by the value of J_{sc} at the band gap wavelength divided by the value for the incident AM1.5G spectrum. Wire arrays with fill fractions of 0.15, 0.36, and 0.97 absorb 0.27, 0.49, and 0.75 of the above-bandgap solar spectrum respectively. For the first two cases, the absorption is notably higher than the fill fraction indicating a higher absorption per volume of silicon.

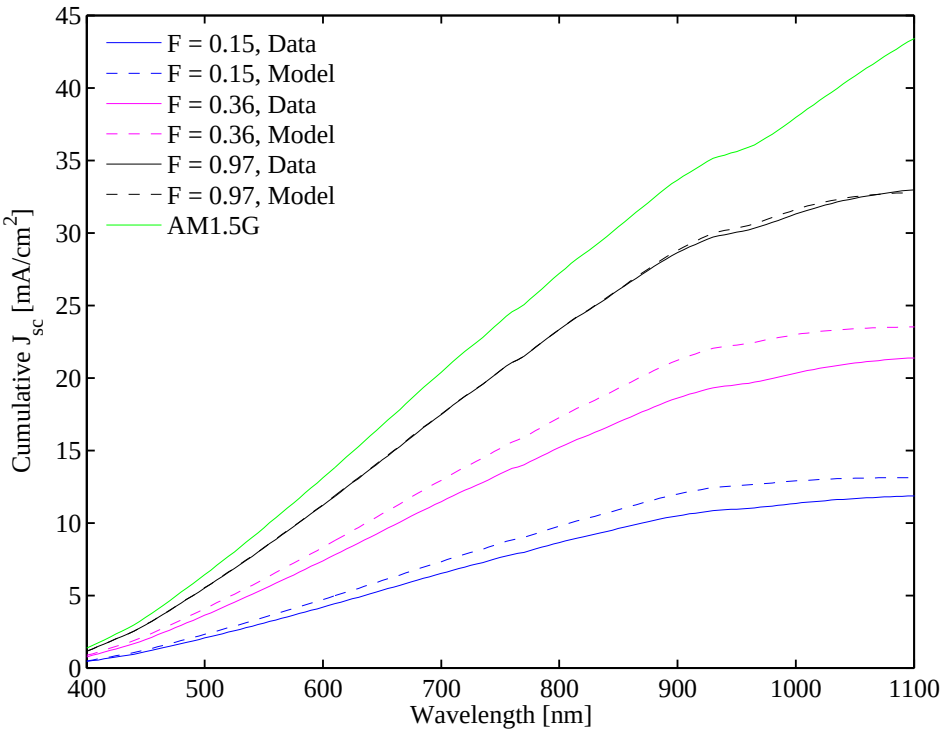

Figure 4.19: Cumulative short circuit current as a function of wavelength, assuming AM1.5G incident solar radiation. The dashed curves are the model, while the solid curves are the experimental data.

4.2.7 Discussion

Though the absorption results for the horizontal array embedded in a dielectric material indicate that total fractional absorption that exceeds the fill factor is possible for $F \leq 0.5$ with a specular or lambertian backreflector, the absolute absorption remains relatively modest for sparse arrays. This implies that cost savings due to reduced material usage would likely be offset by a greater efficiency decrease making the arrays impractical versus conventional planar devices. However, the close packed array ($F = 0.97$) demonstrates 0.75% absorption of wavelength-integrated AM1.5G solar radiation, which is over 90% of the light coupled into the wires considering the near 20% reflection loss from the silicon-epoxy interface. This design results in an equivalent planar thickness of 38 μm which is significantly less than current planar wafers which are $\geq 150 - 200$ μm in thickness. In addition, the horizontally-aligned microwire design could drastically reduce kerf loss since the wire diameter is analogous to the wafer thickness in this case. For these reasons, the close packed array is potentially of interest as a means of achieving high absorption while reducing effective cell thickness.

In addition, horizontal arrays with smaller fill fractions without a backreflector have the potential to function as semi-transparent solar cells. As demonstrated by the results in this section, there is a wide range of tunable transparency achievable by varying the fill fraction. Furthermore, the transparency is roughly constant over the visible wavelengths measured here implying 'white' transmitted light, an attractive feature for windows.

The modeling techniques are in general able to reproduce the qualitative behavior of the experimental data. In particular, the Gee model is in good general agreement with the results as a function of wavelength and fill factor for the cases of the lambertian backreflector, and no backreflector.

4.3 General Discussion

The results presented for both structures indicate that total integrated absorption over 70% is achievable with an effective device thickness of 50 μm or less. Given the relatively similar predicted absorption values, the horizontal alignment geometry is likely to be preferable given the simplicity to implement in practice. Experimentally realizing the cone geometry requires more research into controlling and reproducing the etch profiles as well as selectively coating the conical profile with a high reflective metal coating (shown to be necessary for high absorption). Due to these concerns, experimentally achieving the modelled values may prove difficult. The horizontal geometry was realized experimentally in this work, and an array was processed into a functional solar cell with efficiency of 3.5% (see submitted manuscript). In addition, in the case of the horizontal alignment the wire length can account for one areal dimension of the solar cell whereas in the the cone geometry wire bundles would need to be assembled and cut into slices increasing complexity and material losses from kerf loss.

Thus, the most attractive geometry for achieving maximal efficiency in practice appears to be the horizontal alignment with a near-unity fill factor. In this case, the wire array closely resembles a planar cell, with the fiber-drawing method serving as an effective purification and crystallization technique to achieve reduced effective cell thickness. In addition, as mentioned previously the horizontal alignment also has the flexibility to serve niche applications as a semi-transparent cell.

Further Work

The modeling and experimental results presented in the last chapter have identified several areas for potential further work. These are presented for the vertical and horizontal alignments separately.

For the vertically aligned cone structure, the most obvious future work involves efforts to controllably produce arrays with this metal-coated conical cavity. There are many challenges to achieving some of which were touched on in previous section such as the reproducibility of the etch profile and applying a selective metal coating to the cone surface while leaving the wires un-coated. If these could be achieved, a further next step could involve applying an AR coating to the wire surfaces to reduce the fresnel reflectivity. This degree to which this improves absorption could be explored using the ray tracing code. Another potential area of further work with regard to the vertical alignment involves abandoning the cone structure and adopting the technique used by Kelzenberg *et al.*, [21] AR coating the wires and embedding the array in a medium with scattering centers to enhance ray randomization. This technique demonstrated high absorption that may be transferable to larger wire diameters if the high absorption was not greatly influenced by wave-optic effects.

For the horizontal alignment, further work involves efforts to increase the absorption in close-packed arrays. Many of the same strategies used for planar cells could be adopted here, such as texturing the wires and the inclusion of an AR coating. Since the cylindrical shape of the wires is not crucial to this design, efforts to draw wires of different cross-sectional shapes (such as rectangular) could be undertaken to ease assembly of wires into an array of relevant solar cell dimensions.

Conclusion

The use of silicon microwires represents an attractive means to reduce the cost of crystalline solar cells by relaxing material purity requirements and utilizing less material. Microwire arrays have been studied extensively in the past, with demonstrated high absorption of incident solar radiation possible using far less material per area than conventional wafer-based cells. In this work, the optical absorption of two microwire array designs using wires produced via the molten core fiber drawing method was investigated through modeling and experimental methods. A vertically-aligned structure with a conical etch cavity was shown through modeling to absorb $\sim 90\%$ of wavelengths up to 900 nm at normal incidence, with the results being relatively insensitive to geometrical parameters. An array of 500 μm height and 80 μm diameter wires packed with a 9.7% areal fill fraction demonstrated a day-integrated absorption of 77% over the above-bandgap solar spectrum. A second design consisting of horizontally-aligned microwires was also investigated using modeling and experimental techniques. An array with a fill fraction $F = 0.97$ was measured to absorb 75% of the incident above bandgap solar spectrum when placed on a lambertian backreflector. Absorption exceeding the fill fraction was demonstrated for arrays with $F < 0.5$ in the same case, with general agreement between the experimental and modeling techniques. Horizontal arrays without a backreflector with reduced fill fractions also demonstrated the potential for tunable array transparency by varying the fill factor.

The horizontal array geometry was identified as the most promising of the two designs considered here due to reduced complexity and the ability to reduce effective

material thickness without inherent kerf losses. The absorption of near unity fill factor arrays could likely be increased using conventional processing techniques such as AR coatings currently applied to wafer-based cells. Horizontal-based designs thus have the potential to realize high fractional absorption values with reduced silicon usage compared to conventional planar cells implying a lower $/Watt value, while designs with a reduced fill factor can potentially function as semi-transparent cells.

Bibliography

[1] John Conti et al. International energy outlook 2014. Technical report, U.S. Energy Information Administration, 2014. Available: www.eia.gov.

[2] R. Perez and M. Perez. A fundamental look at energy reserves for the planet. *The IEA SHC Solar Update*, 50:2, 2009.

[3] Axel Metz et al. International technology roadmap for photovoltaic. Technical report, Semi, 2015. Available: www.itrpv.net.

[4] D. M. Powell, M. T. Winkler, H. J. Choi, C. B. Simmons, D. Berney Needleman, and T. Buonassisi. Crystalline silicon photovoltaics: a cost analysis framework for determining technology pathways to reach baseload electricity costs. *Energy Environ. Sci.*, 5:5874–5883, 2012.

[5] Shayle Kann et al. U.S. solar market insight report. Technical report, GMT and SEIA, 2015. Excecutive summary, available: www.seia.org.

[6] J. Jean, P. R. Brown, R. L. Jaffe, T. Buonassisi, and V. Bulovic. Pathways for solar photovoltaics. *Energy Environ. Sci.*, 8:1200, 2015.

[7] J. Nelson. *The Physics of Solar Cells*. Imperial College Press, 2004.

[8] J. Ballato, T. Hawkins, P. Foy, R. Stolen, B. Kokuoz, M. Ellison, C. McMillen, J. Reppert, A. M. Rao, M. Daw, S. R. Sharma, R. Shori, O. Stafsudd, R. R. Rice, and D. R. Powers. Silicon optical fiber. *Opt. Express*, 16(23):18675–18683, Nov 2008.

[9] F. Martinsen, B. K. Smeltzer, M. Nord, T. Hawkins, J. Ballato, and U. Gibson. Silicon-core glass fibers as microwire radial-junction solar cells. *Sci. Rep.*, 4:6283, 2014.

[10] E. F. Nordstrand, A. N. Dibbs, A. J. Eraker, and U. J. Gibson. Alkaline oxide interface modifiers for silicon fiber production. *Optics Express*, 3(5):651, 2013.

[11] PV Lighthouse. Solar spectra calculated with SMARTS v 2.9.2. Available: www.pvlighthouse.com.

[12] B.E.A. Saleh and M.C. Teich. *Fundamentals of Photonics*. Wiley, 2007.

[13] Max Born and Emil Wolf. *Principles of Optics*. Pergamon Press, 4th edition, 1970.

[14] P.C.Y. Chang, J.G. Walker, and H.I. Hopcraft. Ray tracing in absorbing media. *J. Quant. Spec. Rad. Trans.*, 96:327–341, 2005.

[15] E. D. Palik and Gorachand Ghosh. *Handbook of optical constants of solids*. Academic Press, 1988.

[16] B. Hua, Q. Lin, Q. Zhang, and Z. Fan. Efficient photon management with nanostructures for photovoltaics. *Nanoscale*, 5:6627, 2013.

[17] Mei-Ling Kuo, David J. Poxson, Yong Sung Kim, Frank W. Mont, Jong Kyu Kim, E. Fred Schubert, and Shawn-Yu Lin. Realization of a near-perfect antireflection coating for silicon solar energy utilization. *Opt. Lett.*, 33(21):2527–2529, Nov 2008.

[18] E. Yablonovitch. Statistical ray optics. *J. Opt. Soc. Am.*, 72:899–907, 1982.

[19] Brendan M. Kayes. *Radial pn Junction, Wire Array Solar Cells*. PhD thesis, California Institute of Technology, 2008.

[20] B. M. Kayes, H. A. Atwater, and N. S. Lewis. Comparison of the device physics principles of planar and radial p-n junction nanorod solar cells. *J. App. Phys*, 97:114302, 2005.

[21] M. D. Kelzenberg, S. W. Boettcher, J. A. Petykiewicz, D. B. Turner-Evans, M. C. Putnam, E. L.Warren, J. M. Spurgeon, R. M. Briggs, N. S. Lewis, and H. A. Atwater. Enhanced absorption and carrier collection in si wire arrays for photovoltaic applications. *Nat. Mat.*, 9:239, 2010.

[22] Michael D. Kelzenberg. *Silicon Microwire Photovoltaics*. PhD thesis, California Institute of Technology, 2010.

[23] E. L. Warren, H. A. Atwater, and N. S. Lewis. Silicon microwire arrays for solar energy-conversion applications. *J. App. Phys. Chem.*, 118:747–759, 2014.

[24] E.D. Kosten, E.L. Warren, and H.A. Atwater. Ray optical light trapping in silicon microwires: exceeding the 2n2 intensity limit. *Optics Express*, 19(4), 2011.

[25] Michael D. Kelzenberg, Daniel B. Turner-Evans, Morgan C. Putnam, Shannon W. Boettcher, Ryan M. Briggs, Jae Yeon Baek, Nathan S. Lewis, and Harry A. Atwater. High-performance si microwire photovoltaics. *Energy Environ. Sci.*, 4:866–871, 2011.

[26] B. Tian, X. Zheng, T. J. Kempa, Y. Fang, N. Yu, J. Huang, and C. M. Lieber. Coaxial silicon nanowires as solar cells and nanoelectronic power sources. *Nature*, 2007.

[27] M. Gharghi, E. Fathi, B. Kante, S. Sivoththamam, and X. Zhang. Heterojunction silicon microwire solar cells. *Nano Letters*, 12:6278, 2012.

[28] R. He, T. Day, M. Krishanmurthi, J. Sparks, P. Sazio, V. Gopalan, and J. Badding. Silicon p-i-n junction fibers. *Adv. Mater.*, 25:1461, 2013.

[29] D. M. Callahan, J. N. Munday, and H. A. Atwater. Solar cell light trapping beyond the ray optic limit. .

[30] B. C. P. Sturmberg, K. B. Dossou, L. C. Botten, A. A. Asatryan, C. G. Poulton, C. M. de Sterke, and R. C. McPhedran. Modal analysis of enhanced absorption in silicon nanowire arrays. *Opt. Exp.*, 19:A1067, 2001.

[31] H. Alaeian, A. C. Atre, and J. A. Dionne. Optimized light absorption in Si wire array solar cells. *J. Opt.*, 14:024006, 2012.

[32] S. Eyderman, S. John, and A. Deinega. Solar light trapping in slanted conical-pore photonic crystals: Beyond statistical ray trapping. *J. App. Phys.*, 113:154315, 2013.

[33] X. Zhang, C. W. Pinion, J. D. Christesen, C. J. Flynn, T. A. Celano, and J. F. Cahoon. Horizontal silicon nanowires with radial p-n junctions: A platform for unconventional solar cells. *J. Phys. Chem. Lett.*, 4:2002, 2013.

[34] D. G. Goebel. Generalized integrating-sphere theory. *Appl. Opt.*, 6:125, 1967.

[35] M. W. Finkel. Integrating sphere theory. *Opt. Comm.*, 2:25, 1970.

[36] Labsphere. *Integrating Sphere Theory and Applications*. Technical Guide, Available: www.labsphere.com.

[37] B. G. Streetman and S. K. Banerjee. *Solid State Electronic Devices*. PHI Learning Private Limited, 6th edition, 2009.

[38] Brookdeal Electronics LTD. *Model 401A Lock-in Amplifier*. Manual.

[39] J. M. Gee. The effect of parasitic absorption losses on light trapping in thin silicon solar cells. In *20th IEEE Photovoltaic Specialists Conference*, Sept. 1988.

[40] N. Otsu. A threshold selection method from gray-level histograms. *IEE Trans. Sys., Man, Cyb.*, 9:62, 1979.

[41] S. C. Baker-Finch, K. R. McIntosh, D. Yan, K. C. Fong, and Teng C. Kho. Near-infrared free carrier absorption in heavily doped silicon. *J. App. Phys*, 116:063106, 2014.

[42] J. I. Pankove. *Optical Processes in Semiconductors*. Prentice-Hall Inc., Englewood Cliffs, New Jersey, 1971.

Appendix A: Paper I

This paper was published in Scientic Reports in September 2014: http://www.nature.com/srep/2014/140904/srep06283/full/srep06283.html

B.K.S. performed the optical ray modeling shown in Fig. 4, as well as being involved in the discussion.

SCIENTIFIC REPORTS

OPEN

SUBJECT AREAS:
SOLAR ENERGY AND PHOTOVOLTAIC TECHNOLOGY
SILICON PHOTONICS

Received
20 June 2014

Accepted
15 August 2014

Published
4 September 2014

Correspondence and requests for materials should be addressed to F.A.M. (fredrik.martinsen@ntnu.no)

Silicon-core glass fibres as microwire radial-junction solar cells

F. A. Martinsen[1], B. K. Smeltzer[1], M. Nord[1], T. Hawkins[2], J. Ballato[2] & U. J. Gibson[1]

[1]Department of Physics, Norwegian University of Science and Technology, N-7491, Trondheim, Norway, [2]The Center for Optical Materials Science and Engineering, Technologies (COMSET), Department of Material Science and Engineering, Clemson, SC, 29634, USA.

Vertically aligned radial-junction solar cell designs offer potential improvements over planar geometries, as carrier generation occurs close to the junction for all absorption depths, but most production methods still require a single crystal substrate. Here, we report on the fabrication of such solar cells from polycrystalline, low purity (99.98%) p-type silicon starting material, formed into silicon core, silica sheath fibres using bulk glass draw techniques. Short segments were cut from the fibres, and the silica was etched from one side, which exposed the core and formed a conical cavity around it. We then used vapour deposition techniques to create p-i-n junction solar cells. Prototype cells formed from single fibres have shown conversion efficiencies up to 3.6%, despite the low purity of the starting material. This fabrication method has the potential to reduce the energy cost and the silicon volume required for solar cell production. Simulations were performed to investigate the potential of the conical cavity around the silicon core for light collection. Absorption of over 90% of the incident light was predicted, over a wide range of wavelengths, using these structures in combination with a 10% volume fraction of silicon.

In the quest for greater utilisation of solar photovoltaic conversion, many avenues are being pursued to reduce costs, improve performance, or take advantage of abundant, low toxicity constituent materials. One approach to reduce the cost and improve the performance is the use of vertically aligned radial junction solar cells. Radial junctions increase absorption and decouple the carrier collection path from the optical absorption direction by aligning most of the junction with the direction of the impinging light. The design, usually consisting of a forest of free-standing wires, makes use of the natural light trapping of this geometry in order to increase the amount of light absorbed per semiconductor volume. Radial junction cells have been realized from a wide range of materials, including GaAs, InP, InGaAs and dye sensitized oxides, as well as organic and chalcogenide fibres[1–8]. However, silicon still dominates the solar cell market, and improvements within this established technology area are of interest.

Vertically aligned silicon radial junction solar cells are being investigated as an alternative to planar silicon wafers to reduce the cost of silicon solar cells while maintaining high efficiency[9–20]. The radius of the semiconductor microwire can be matched to the minority carrier diffusion length[21], allowing efficient modules to be fabricated from lower quality materials[16,22]. However, for very high aspect-ratio wires, surface recombination, and long distances for majority carrier extraction can be problematic. For optimum performance, microwire height should be on the order of 100–200 μm and the diameter should be close to the minority carrier recombination length[21], which may be up to tens or hundreds of microns depending on silicon quality. The desired scale is thus one that is readily accessible via the bulk, commercially-employed fibre-drawing technique used here. In addition, purification during drawing is possible, as the melting and recrystallization of the silicon during the drawing process leads to in-situ segregation of impurities -- on a timescale that is much less than that needed when bulk silicon is processed[23,24] due to the small diameter of the fibre core.

Radial-junction silicon solar cells have been successfully produced using the catalyst assisted vapour liquid solid (VLS) growth method[9–14] and deep reactive ion etching of silicon wafers[15–17]. Both methods have produced cells with efficiencies of ~10%, as well as significantly enhanced light absorption per unit of silicon compared to planar cells[9,16]. Nonetheless, the reliance on single-crystal substrates as well as introduction of detrimental impurities during production for both methods motivates the search for alternative approaches. One such route is the fabrication of silicon-core glass-clad fibres, with a subsequent assembly of a substrate-independent cell, which may also allow new flexible designs to be realized. The fibre cores are the only silicon in the design, potentially reducing the amounts of material and energy required for solar cell production.

Two known methods for fabrication of free-standing silicon fibres are high-pressure chemical vapour deposition (HPCVD) in capillary pores[25] and molten-core fibre drawing[26–28]. He, et al.[25] demonstrated the HPCVD approach for solar applications, where they made 15 μm diameter flexible coaxial in-fibre solar cells with conversion efficiencies of 0.5%. Early molten-core fibres were reported to suffer from mechanical stress as well as oxygen incorporation[26], and were not investigated earlier as a potential solar cell material. Recently, the use of alkaline earth oxide interface modifiers[29,30] to relieve mechanical stress and hinder oxygen in-diffusion during production of long silicon core fibres was demonstrated. This modification was used here in production of fibres from low purity silicon, and we report on their performance as radial junction solar cells. The drawing process improved the purity of the fibres, and etching of the interface layer also led to formation of a conical cavity in the silica cladding surrounding the silicon cores. The potential of this conical cavity for light trapping was investigated through simulations.

A heterojunction with intrinsic thin layer (HIT) design[31–34] was chosen for initial fabrication of fibre-based solar cells. The HIT-design, developed in the 1990s by Sanyo (now Panasonic), utilizes a layer of amorphous hydrogenated intrinsic silicon (a-i-Si:H), instead of the more common SiO_2[11] or Si_xN_y[14,35] for surface passivation, with an amorphous doped silicon layer on top acting as the emitter. The a-i-Si:H passivates dangling bonds at the surface of the crystalline core[20,36], and the higher bandgap of amorphous silicon results in the formation of a majority carrier mirror, enhancing carrier collection[36,37].

Results

Silicon-core fibres. The silicon-core fibres were produced with a range of diameters, varied by changing the preform feed rate (1–3 mm/min) and drawing speed (2–3 m/min). As shown in Fig. 1, the silicon fibre core was surrounded by an interfacial layer and a silica cladding, and analysis with electron dispersive x-ray spectroscopy (EDS) showed that the calcium oxide, pre-deposited on the inside of the silica preform, was confined to a thin interface layer. Calcium oxide is known for the bulk "slag-refining" of silicon where it serves as a sink for impurities, and in fibres the calcium oxide and silica also formed a eutectic structure that accommodated strain as it solidified. Segregation of transition metals and other impurities have been observed during rapid solidification of flakes made with 98% pure silicon[24], and a similar reduction of impurities in the fibres reported here was suggested by large bulk carrier diffusion lengths (see discussion). The p-type fibres had a resistivity of 0.3–0.9 Ω-cm, similar to the silicon starting material, and oxygen levels were measured to be 1.3×10^{17} and 2.1×10^{17} atoms/cm^3 for the starting material and the fibre respectively, demonstrating that the silicon is not significantly degraded by the drawing process. Without the interface layer, oxygen levels greater than 5×10^{21} atoms/cm^3 were reported[26]. The core of our fibres was crystalline silicon with typical grain lengths of several millimetres, as determined by x-ray and electron back scattered diffraction (EBSD). This was larger than the height of the solar cells made from the fibres, so grain boundaries were not incorporated into most cells, despite the rapid solidification of the silicon. Thus the drawing and recrystallization processes led to silicon that was sufficiently pure and had sufficiently large grains to be used for solar cell production, even when starting with a low-purity material.

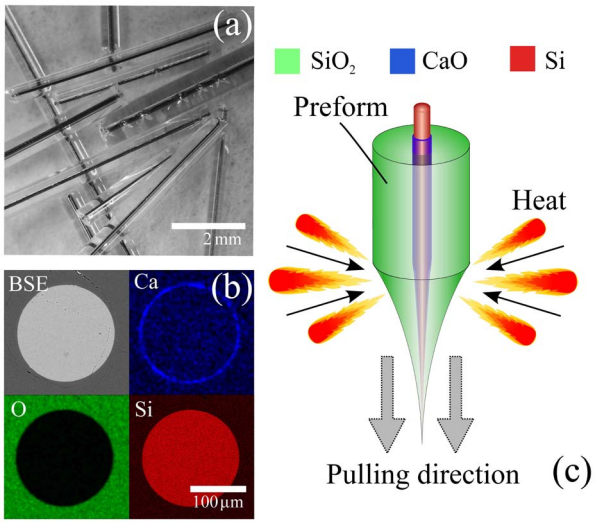

Figure 1 | The fibre product and fabrication method. (a) photograph of fibre pieces with various diameters, (b) a backscattered electron micrograph and energy dispersive x-ray spectroscopy maps for calcium, silicon and oxygen of a fibre cross-section, and (c) schematic of fibre structure during pulling. The silicon core and silica cladding are separated by a thin Ca-containing interface layer.

Single fibre solar cells. Single fibre radial junction solar cells with an open circuit voltage of 0.3 V, a short-circuit current density of 16.6 mA/cm^2, a fill factor of 0.52, and an overall efficiency (using the silicon cross- sectional area as the reference illuminated area) of 3.6% were fabricated. The silicon area was used as we were primarily interested in assessing the quality of the silicon made by fibre drawing. Including additional area would reduce the overall efficiency, but as we show in simulations below, the glass may contribute to performance in future devices. Fig. 2 presents the fabrication procedure, where fibres initially were cut into short segments (Fig. 2a) and one side of these segments was etched in hydrofluoric (HF) acid. The acid attacked the silica cladding and the interface modifier, and a conical cavity (etch cone) formed around the fibre due to rapid etching of the calcium-containing layer (Fig. 2b,f). A second etch was performed on the silicon core in order to remove some of the material damaged by the slicing process as well as to reduce the roughness of the fibre surface (Fig. 2g). Intrinsic and n-type amorphous silicon and electrical contacts were vapour deposited and the I-V characteristics were then measured. Fig. 2e presents the I-V curves of one of the cells under dark and illuminated conditions, both for an as-made cell (Fig. 2h) and for the same cell where the conical cavity surrounding the fibre core was filled with an opaque conductive paste (Fig. 2i). The filling was performed to assess the resistive losses incurred by the use of indium tin oxide (ITO) as the sole conducting path on the top surface, and the potentially poor contact at the bottom of the cavity. Measurement of the as-made cell resulted in similar open circuit voltage and short circuit current as for the filled case, but with a reduction of fill factor from 0.52 down to 0.43. For the filled case, the measured cell can be considered as a single free-standing silicon fibre where the incident light is absorbed only through the top cross section of the fibre.

Amorphous silicon layers. A planar witness cross section transmission electron microscopy (TEM)-sample was prepared in order to inspect a representative interface and the thicknesses of the amorphous layer. Scanning transmission electron microscopy (STEM), electron energy loss spectroscopy (EELS) and EDS were used to examine this sample. As shown in Fig. 3, the amorphous silicon layers had a total thickness of ~32 nm. The outer edge of the film was determined by increasing the brightness of the STEM image, but the original is presented here to allow visualization of the silicon lattice. The ratio of the deposition times for the intrinsic and doped layers was 2:7, in agreement with the measured phosphorus profile, giving layer thicknesses of ≈7 nm and ≈25 nm respectively. These represented the maximum thicknesses possible in the device, since reduced flow of reactants as well as reduced

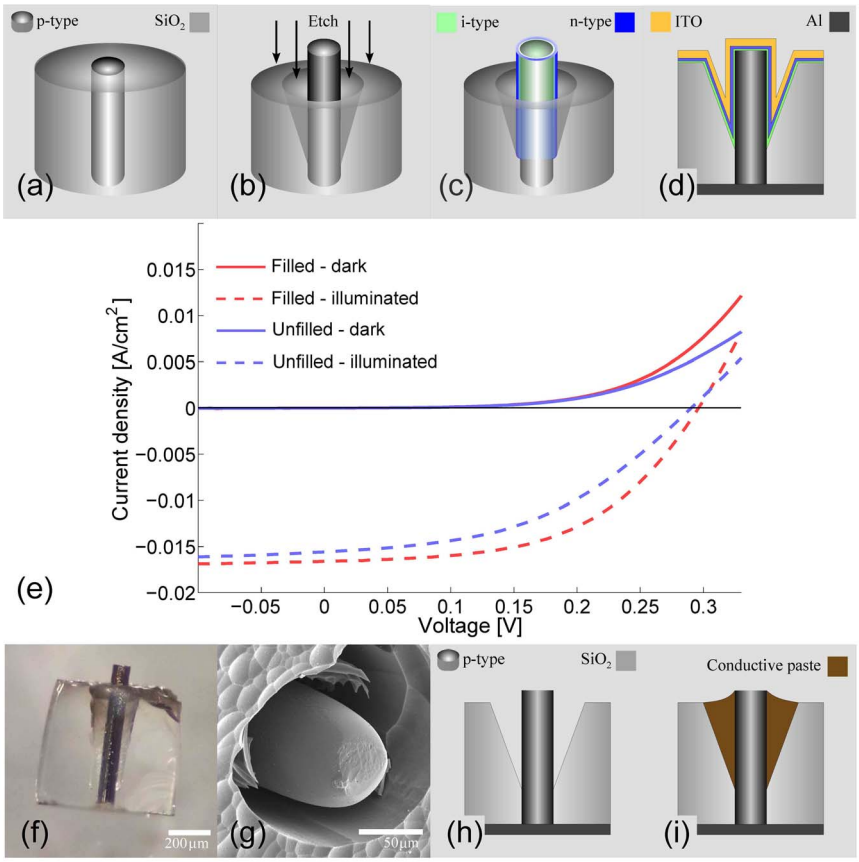

Figure 2 | Stepwise solar cell fabrication procedure and solar cell performance. Processing of a single fibre segment into a solar device: 450 µm segments (a) were selectively etched with HF from one side, resulting in the fibre core being mostly exposed (b) and (f) with a cavity around the fibre core due to the higher etch rate for CaO compared to SiO_2. Deposition of a-i-Si and a-n-Si layers on top of the exposed wire using PECVD formed the p-i-n junction (c). A schematic representation (d) and an SEM image (g) of a processed solar cell and the dark and illuminated I-V curves (e) for a silicon wire with a diameter of 113 µm are shown for both an as-made cell (h) and with the cavity filled with opaque conductive paste (i).

contact with the plasma likely resulted in thinner layers on the portions of the microwire within the etch cone around the fibre.

Light trapping simulations. The efficiency values measured above were based on an individual silicon fibre, using the cross-sectional area of the core in the efficiency calculation. However, in future devices, the silica surrounding the silicon core could contribute to absorption if the etch cone was coated with a reflective material and used as a light collector as shown in Fig. 4a. In order to investigate the light trapping potential, ray-tracing simulations were performed, using unpolarised light, the optical properties of pure silicon for the core, and assuming an opaque silver coating on the cone walls for enhanced reflectivity. The structure was investigated for dependences on incident wavelengths, angle of incidence, the silicon core diameter and the silicon fill fraction. The silicon fill fraction, F is equal to $(D/D_{tot})^2$, where D is the diameter of the core, and D_{tot} is the outer diameter of the silica cone. Although the simulations were performed for individual fibres with their cladding, hexagonal close packing of fibres would allow realization of similar absorption values for large arrays.

The spectral absorption characteristics for wavelengths between 400 nm and 1100 nm are shown in Fig. 4b for several sets of cell parameters, with the calculated absorption of planar silicon shown for comparison. The geometry for the largest structure is similar to the devices we fabricated and measured. All designs perform quite well across the solar spectrum. Due to the high absorption at short wavelengths, only the spectral region above 800 nm had a significant dependence on the design parameters. The angular dependence of the 900 nm absorption for the same structures are shown in Fig. 4c along with spatial maps of the absorption for two different incidence angles (φ) for the largest structure. Despite the simulation being performed for a poorly absorbed wavelength, it can be seen that the light trapping structure, with low silicon content, would have absorption superior to that of planar silicon over a wide range of angles. The smallest cores perform less well at large φ because of the shallower cone angle, θ_{SiO_2} and less absorption during each transmission pass through the silicon. The combination allows more light to escape the etch cone.

Fig. 4d shows the results as the diameter of the core was varied between 10 and 100 µm for several silicon fill fractions and fibre height equal 125 µm. A wavelength of 900 nm was used, as this is where the absorption length in silicon equals the height of the pillar, and conventional cells lose efficiency. For the lowest fill fractions, there is a rolloff in absorption for large diameters because the assumption of fixed height leads to a very shallow cone angle (large θ_{SiO_2}). Taller structures permit better light gathering for large cores at low fill fractions, but increase the total volume of silicon required. For a fill fraction greater than 15%, there was little change in the calculated absorption over the core diameter range of 30–120 µm.

Discussion

The dark and light current-voltage characteristics of the sample single-wire cell with the etch cone filled with opaque conductive paste, shown in Fig. 2, yield an overall conversion efficiency of 3.62%. Measurement of the same cell without the paste, (contacting the ITO on the glass), gave similar open-circuit voltage, V_{oc} and short-circuit current density J_{sc} values, but with a fill factor of 0.43 due to

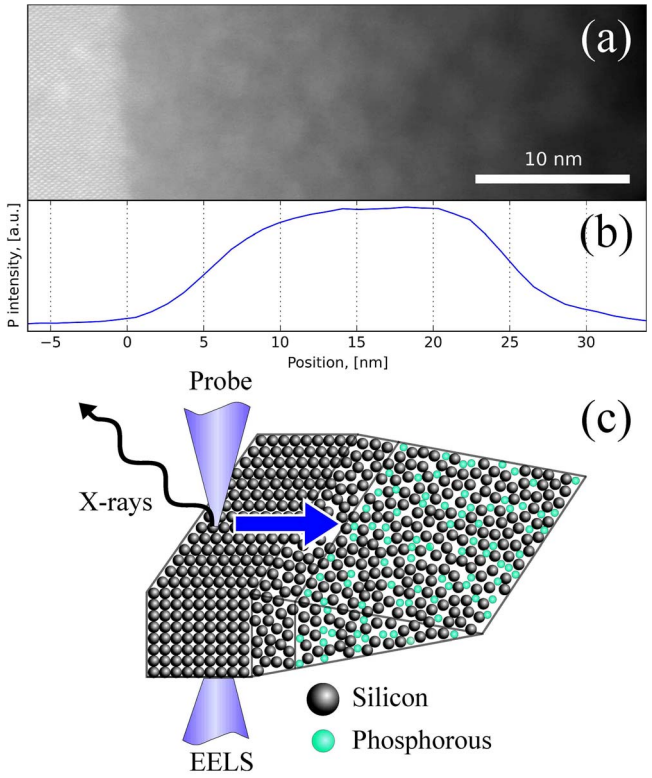

Figure 3 | TEM analysis of the amorphous thin film. A scanning transmission electron micrograph of the amorphous silicon film on a crystalline <100> silicon wafer with the viewing direction along the [011]-axis of the wafer. The film thickness can be observed to be ~32 nm with slight variations along the interface. The phosphorous signal (b) from EDS is offset from the crystalline interface, indicating the approximate thickness of the intrinsic and doped layers. Relative phosphorous content was found using EDS, normalized with respect to thickness using low loss electron energy loss spectroscopy. The loss of contrast and phosphorous signal towards the outer edge of the film is due to a thickness gradient from the specimen preparation, as shown schematically in (c).

reduced carrier extraction, because the indium tin oxide coating is thinner within the cavity. No reflective coating was applied inside the etch cone for these measurements, and it can be seen from comparing the short circuit current densities that the etch cone does not contribute to any increased light trapping for this cell. Optimization of the etched structure together with application of a reflective coating on the inside of the cone would be necessary to fully exploit the structure.

Fitting the dark characteristics of a single fibre cell (filled case) to the non- ideal diode equation

$$I = I_L - \left[exp\left(\frac{qV}{nkT}\right) - 1 \right], \qquad (1)$$

(where I_L is the light-generated current, and n is the ideality factor) between 0 and 0.35 V yields $n = 1.77 \pm 0.11$, indicating preferred recombination at the surface and at the junction rather than in the crystalline quasi-neutral region. This supports the suggestion that the purity of the crystalline silicon fibres is higher than that of the upgraded metallurgical grade (UMG) quality of the starting material, likely due to a segregation based purification during melting and drawing of silicon into the fibre[24]. Similar ideality factor values have been reported for other radial junction solar devices[9,14,15,17,25], typically attributed to their high surface to volume ratio.

The saturation current density was found to be 1200 nA cm^{-2}, which is high compared to reported values for similar designs[15,17]. This high surface recombination is likely to be the main reason for the low observed open circuit voltage and thus improvements in junction- and surface quality are expected to improve the overall performance of the cell. The high net carrier recombination rate of the device presented here may be due to surface damage near the top of the fibre from the slicing process (Fig. 2f). An improved cutting technique and surface etch together with an optimization of the device layer thicknesses would likely increase the performance of the cell. The fibre radius could also be tuned to better match the minority carrier diffusion length[21].

Simulations on the silver-coated reflective etch cone in the SiO_2 (Fig. 5a) indicate that light gathering by these structures would be highly effective, with >90% absorption for most geometries and wavelengths. This implies that device design could be optimized within wide limits based on the carrier diffusion length and surface recombination properties of the silicon cores. The spectrally averaged absorption of the cone plus fibre structure can be expected to exceed 90% at normal incidence, with little angular dependence up to ~20 degrees, for fill fractions of silicon ≤ 10%. This is close to the absorption coefficient achieved for antireflection-coated texturized planar solar cells (95–97%)[38] which incorporate 10 times as much silicon, and require purification, bulk recrystallization and wafering. The simulations above do not assume any treatment to reduce reflection from the top of the silicon core, but for 10% fill fraction of silicon, this is responsible for ~4% loss, or nearly half of the total reflection losses. Texturizing or antireflection coating of the top surface of the microwires would further increase the absorption.

A potential route for making practical large-scale devices is through assembly and slicing of bundles of fibres with subsequent processing of the entire slices into solar cells. This would result in the structure shown in Fig. 5b where the fibres are packed together hexagonally with a 0.91 packing factor. The imperfect packing would result in an additional loss over the simulated values, for which integration was carried out only to the edge of the cylindrical silica cladding. However, fusing the glass fibres, or fabricating multicore fibres in the drawing process would allow the etching process to be carried out until the etch cones merged, as shown in Fig. 5c, and absorption values would increase towards those for the simulated individual cladding-fibre structures. Future improvements in the junctions and single-wire conversion efficiency should carry over to array performance.

Potential fibre draw speeds of tens of meters per second are possible. With a 50-core parallel structure a 10% area fill fraction of silicon, and 125 μm thickness cells (allowing a 50 μm kerf loss during slicing), one tower could produce adequate material for ~60 square meters of solar cells per hour. This process would eliminate the time and energy consuming production of ingots, as the silicon is refined in situ as part of the drawing process, and would require only a tenth of the starting silicon material needed for a conventional cell, per unit area. It should be noted that, while an optical fibre tower was employed for these prototype fibres, there is no need for the high precision afforded by this equipment.

In conclusion we have demonstrated the feasibility of producing solar cells from low-grade silicon incorporated into glass-clad fibres made using the molten-core fibre drawing technique. The first single-fibre cells have efficiencies up to 3.62%, with junction quality rather than silicon quality being the limiting factor, leaving room for improvements over the presented prototype. Future directions may include improvement of the processing of the silicon cores, utilization of the etch cone for light gathering and fabrication of multicore fibres[28] for parallel production of cell arrays.

Methods

Fibre production. Glass preforms for the fibre-drawing process were prepared by coating the inside of a thick-walled silica tube with calcium hydroxide, drying the coating, then loading a solid silicon rod into the closed tube. The CaO coating was produced following the method of Nordstrand, et al.[29] For this work, a 2 mm

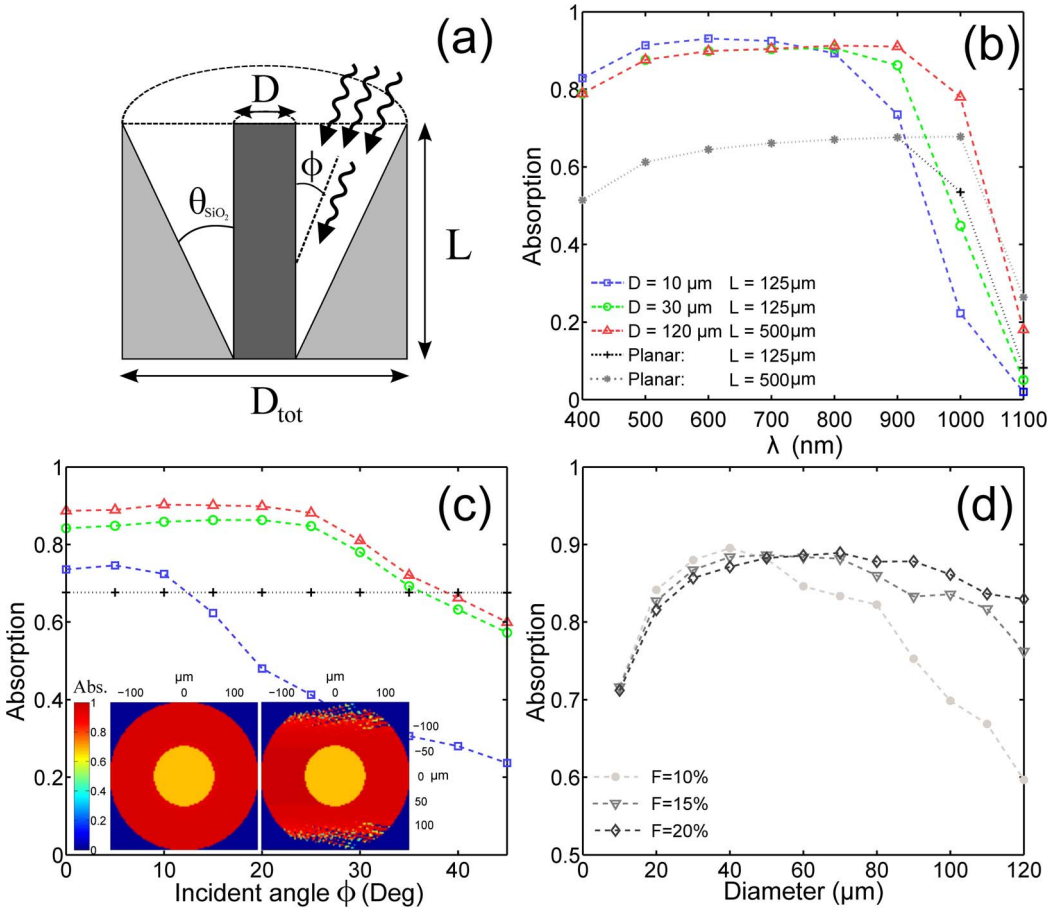

Figure 4 | Simulations of light gathering. (a) schematic of the light trapping structure, (b) absorption as a function of wavelength for three diameter and height combinations keeping $\theta_{SiO_2} = 10^{\circ}$. (c) absorption as a function of angle for $\lambda = 900$ nm and the same geometries used in (b) [the legend in (b) applies to (b) and (c)], and (d) absorption for three fill fractions as a function of diameter for $\lambda = 900$ nm and $L = 125$ μm. Inset in (c) shows a spatial map of the absorption at normal incidence ($\varphi = 0$) and $\varphi = 30$ degrees.

diameter p-type silicon rod of upgraded metallurgical grade (UMG ~ 99.98%) quality was inserted into a CaO (99.9%) coated 3 × 30 mm silica glass tube, which then was drawn in a Heathway draw tower at a feed rate of 3 mm/min and a draw rate of 2.7 m/min at 1950°C to form bulk lengths of fibre. Silicon core diameters between 50–200 μm were realized with the above parameters yielding an approximate 100 : 1 ratio of silica to silicon by volume.

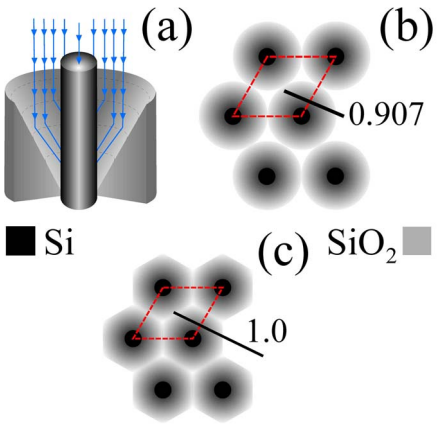

Figure 5 | Schematics illustrating utilization of the etch cone for scale-up purposes. (a) schematic of light gathering in a single etched silica-clad fibre and (b) top view of a bundle of fibres etched to gather light incident on the coated silica. There is a 9.3% loss due to air gaps for bundled cylinders, but fusing of the silica (c) would reduce or eliminate this loss. Packing factors are shown for cylinders and hexagonal columns.

Fibre characterization. For electrical characterization purposes, the silica cladding was etched away from the as-made fibres using an aqueous solution of 48% HF (27.6 M). The cores remained intact during this etch. The fibres were subsequently contacted with aluminium using a sputter coater and a shadow mask, and the resistivity was measured using the four-point probe technique. Crystallinity was confirmed by electron backscattered diffraction (EBSD) in a Hitachi SU-6600 field emission gun (FEG)-SEM operating at 20 keV. Grain lengths on the order of several mm were routinely observed. In order to investigate in-diffusion of oxygen during the fibre drawing process, the oxygen level of the source silicon was compared to that of an as-drawn fibre using secondary ion mass spectroscopy (SIMS). The investigation was conducted using a Cameca IMS 7 SIMS operating at 10 keV with a primary beam of Cs^+-ions, and the measured signals were averaged over a depth of 500 nm after sputtering through the surface contamination on the samples.

Device fabrication. The fabrication of the HIT structure and hence a functional solar cell was carried out by casting a bundle of the as-made fibres in epoxy for easier handling, and cutting this structure into 450 μm slices, resulting in slices containing fibre segments like the one schematically illustrated in Fig. 2a. All processing was performed on the multifibre slices, but these were disassembled at the end of the fabrication cycle and single fibres were measured as solar cells. The segments were, subsequent to cutting, selectively etched from one side in a 48% HF aqueous solution (27.6 M) for 20 min, revealing the front part of the fibre core and leaving the back untouched (Fig. 2b, f). This etch produces a conical cavity around the fibre due to the greater reactivity of the calcium- rich interface layer compared to that of SiO_2, as seen in Fig. 2b,f. The exposed silicon cores were then etched for up to one minute in a modified CP4 solution consisting of a 7 : 2 : 1 mixture of 65% HNO_3 in water (14.5 M), 48% HF in water (27.6 M) and 100% CH3COOH (17.4 M) in order to reduce surface irregularities as well as the saw-damaged areas of the fibre tips. The latter etch also resulted in the fibre core being shortened and rounded, as can be seen in Fig. 2g. The deposition of the amorphous silicon layers and hence the formation of the p-i-n junction was performed using an Oxford Instruments plasma enhanced chemical vapour deposition (PECVD) unit, operating at 150°C. The temperature was chosen in accordance with Wang, et al.[39], in order to minimize the formation of microcrystallites that are reported to cause disruptions in the localized band structure

of the amorphous silicon film and an associated reduction of the passivation effectiveness. Prior to deposition, the fibre slices were given a 2 minute etch in a 5% HF aqueous solution (2.9 M) to remove any native oxide that had formed after the CP4 etch, and to promote hydrogen termination of the fibres, enhancing surface passivation. The amorphous silicon was deposited at a rate of 0.36 nm/s with a gas pressure of 1000 mTorr, a flow rate of 25 sccm SiH_4 in 475 sccm Ar for the a-i-Si, and at 1000 mTorr with 25 sccm SiH_4 + 50 sccm 10% PH_4:Ar in 425 sccm Ar for the a-n-Si. Finally, the contacts were sputter-deposited, applying 200 nm indium tin oxide (ITO, $\rho \sim 1.7 \times 10^{-3}$ Ω-cm, 1.2 nm/s) as the front contact and 150 nm aluminium (1.3 nm/s) overcoated with 150 nm platinum (1.66 nm/s) as the back contact.

Transmission electron microscopy. The analysis of the amorphous silicon film cross section was performed with high angle annular dark field scanning transmission electron microscopy (HAADF-STEM) using a JEOL ARM 200F TEM, and the thickness of the combined amorphous layers was measured to be ~32 nm (Fig. 3a). The witness wafer was used due the challenge associated with TEM specimen preparation of fibres, but the film thicknesses on the wafer should be similar to that on the top surface of the fibre. Comparing the measured thickness with the deposition times used in the PECVD and assuming linear relationships between deposition time and thickness results in an a-i-Si layer of ≈7 nm and an a-n-Si layer of ≈25 nm. The latter was confirmed by conducting an EDS-scan for phosphorous across the film cross-section, with thickness normalization performed using the simultaneously acquired low loss electron energy loss spectroscopy signal (Fig. 3b). Comparing the EDS scan with the corresponding STEM image reveals the predicted a-i-Si layer between the crystalline phase and the a-n-Si layer. A drop in the phosphorous signal close to the edge of the amorphous film is believed to be caused by a very poor signal to noise ratio caused by the reduced thickness of the sample when approaching the sample edge, as illustrated schematically in Fig. 3c.

Device testing. After disassembly of the slices used in the fabrication process, the IV-characteristics for single fibre cells were measured under air mass 1.5 global (AM 1.5G) illumination at normal incidence, and the cross-sectional area of the fibre core was used as the reference illuminated area. In addition to measuring the as-made cell, a measurement was performed where external influences from the glass surrounding the fibre core were eliminated by filling the groove surrounding the fibre core, visible in Fig. 2, with opaque conductive paste.

Optical modelling. A ray-tracing model was used to calculate the absorption of the idealized structure visible in Fig. 4a, for a variety of parameters. Using unpolarised light, the optical constants of silicon for the core and of silver for the cone surface, incoming rays were modelled through multiple reflections and transmission passes through the silicon until they were either absorbed or escaped the cone. Because it is metallized in the solar cell structure, the bottom surface of the silicon core was assumed, for simplicity, to have R = 1; this represents less than a 1% error at a 900 nm wavelength. For non-normal incidence, the problem was solved three-dimensionally by approximating the cone with 64 trapezoids, calculating the incidence angle and the reflection and transmission coefficients at each interface. The absorption coefficient of silicon was used with Beer's Law to calculate the absorption within the silicon core.

1. Holm, J. V. *et al.* Surface-passivated GaAsP single-nanowire solar cells exceeding 10% efficiency grown on silicon. *Nat. Commun.* **4**, 1498 (2013).
2. Law, M., Greene, L. E., Johnson, J. C., Saykally, R. & Yang, P. Nanowire dye-sensitized solar cells. *Nat. Mater.* **4**, 455–459 (2005).
3. Wallentin, J. *et al.* InP nanowire array solar cells achieving 13.8% efficiency by exceeding the ray optics Limit. *Science* **339**, 1057–1060 (2013).
4. Mohseni, P. K. *et al.* Monolithic III-V nanowire solar cells on graphene via direct van der Waals epitaxy. *Adv. Mater.* **26**, 3755–3760 (2014).
5. Lee, M. R. *et al.* Solar power wires based on organic photovoltaic materials. *Science* **324**, 232–235 (2009).
6. Fan, X., Huang, L., Du, J., Liu, Z. & Tao, C. Role of interfacial strain in fiber-shaped solar cell based on TiO2 nanotube arrays. *J. Nanosci. Nanotechnol.* **14**, 7111–7116 (2014).
7. Orf, N. D. *et al.* Fiber draw synthesis. *Proc. Natl. Acad. Sci. U. S. A.* **108**, 4743–4747 (2011).
8. Toivola, M., Ferenets, M., Lund, P. & Harlin, A. Photovoltaic fiber. *Thin Solid Films* **517**, 2799–2802 (2009).
9. Kelzenberg, M. D. *et al.* Enhanced absorption and carrier collection in Si wire arrays for photovoltaic applications. *Nat. Mater.* **9**, 239–244 (2010).
10. Tian, B. *et al.* Coaxial silicon nanowires as solar cells and nanoelectronic power sources. *Nature* **449**, 885–889 (2007).
11. Seo, K. *et al.* Si microwire solar cells: improved efficiency with a conformal SiO2 layer. *ACS Nano* **7**, 5539–5545 (2013).
12. Kendrick, C. E. *et al.* Radial junction silicon wire array solar cells fabricated by gold-catalyzed vapor-liquid-solid growth. *Appl. Phys. Lett.* **97**, 143108 (2010).
13. Jia, G., Steglich, M., Sill, I. & Falk, F. Core-shell heterojunction solar cells on silicon nanowire arrays. *Sol. Energy Mater. Sol. Cells* **96**, 226–230 (2012).
14. Kelzenberg, M. D. *et al.* High-performance Si microwire photovoltaics. *Energy Environ. Sci.* **4**, 866–871 (2011).
15. Kim, D. R., Lee, C. H., Rao, P. M., Cho, I. S. & Zheng, X. Hybrid Si microwire and planar solar cells: Passivation and characterization. *Nano Lett.* **11**, 2704–2708 (2011).
16. Gharghi, M., Fathi, E., Kante, B., Sivoththaman, S. & Zhang, X. Heterojunction silicon microwire solar cells. *Nano Lett.* **12**, 6278–6282 (2012).
17. Yoon, H. P. *et al.* Enhanced conversion efficiencies for pillar array solar cells fabricated from crystalline silicon with short minority carrier diffusion lengths. *Appl. Phys. Lett.* **96**, 213503 (2010).
18. Guo, N. *et al.* Fabrication of silicon microwire arrays for photovoltaic applications. *Appl. Phys. A* **102**, 109–114 (2011).
19. Garnett, E. & Yang, P. Light Trapping in Silicon Nanowire Solar Cells. *Nano Lett.* **10**, 1082–1087 (2010).
20. Dan, Y. *et al.* Dramatic reduction of surface recombination by in situ surface passivation of silicon nanowires. *Nano Lett.* **11**, 2527–2532 (2011).
21. Kayes, B. M., Atwater, H. A. & Lewis, N. S. Comparison of the device physics principles of planar and radial p-n junction nanorod solar cells. *J. Appl. Phys.* **97**, 114302 (2005).
22. Gharghi, M. On the design and applicability of nanowire solar cells using low-grade semiconductors. *J. Appl. Phys.* **111**, 034501 (2012).
23. Levine, J. D. & Jensen, M. J. Texas Instruments Inc., Production of semiconductor grade silicon spheres from metallurgical grade silicon particles. United States patent US 5,069,740 A. 1991 Des 3.
24. Martinsen, F. A., Nordstrand, E. F. & Gibson, U. J. Purification of melt-spun metallurgical grade silicon micro-flakes through a multi-step segregation procedure. *J. Cryst. Growth* **363**, 33–39 (2013).
25. He, R. *et al.* Silicon p-i-n junction fibers. *Adv. Mater.* **25**, 1461–1467 (2013).
26. Ballato, J. *et al.* Silicon optical fiber. *Opt. Express* **16**, 18675–18683 (2008).
27. Scott, B. L., Wang, K. & Pickrell, G. Fabrication of n-type silicon optical fibers. *IEEE Photonics Technol. Lett.* **21**, 1798–1800 (2009).
28. Gumennik, A. *et al.* Silicon-in-silica spheres via axial thermal gradient in-fibre capillary instabilities. *Nat. Commun.* **4** (2013).
29. Nordstrand, E. F., Dibbs, A. N., Eraker, A. J. & Gibson, U. J. Alkaline oxide interface modifiers for silicon fiber production. *Opt. Mater. Express* **3**, 651–657 (2013).
30. Gibson, U. J., Dibbs, A., Eraker, A., Hawkins, T. & Ballato, J. Alkaline oxide modifiers for the production of semiconductor fibers. *Workshop Spec. Opt. Fibers Their Appl.* W1.3; DOI:10.1364/wsof.2013.w1.3 (2013)
31. Mishima, T., Taguchi, M., Sakata, H. & Maruyama, E. Development status of high-efficiency HIT solar cells. *Sol. Energy Mater. Sol. Cells* **95**, 18–21 (2011).
32. Taguchi, M., Terakawa, A., Maruyama, E. & Tanaka, M. Obtaining a higher V-oc in HIT cells. *Prog. Photovolt.* **13**, 481–488 (2005).
33. Wang, Q. *et al.* Efficient heterojunction solar cells on p-type crystal silicon wafers. *Appl. Phys. Lett.* **96**, 013507 (2010).
34. Dao, V. A. *et al.* Simulation and study of the influence of the buffer intrinsic layer, back-surface field, densities of interface defects, resistivity of p-type silicon substrate and transparent conductive oxide on heterojunction with intrinsic thin-layer (HIT) solar cell. *Sol. Energy* **84**, 777–783 (2010).
35. Putnam, M. C. *et al.* Si microwire-array solar cells. *Energy Environ. Sci.* **3**, 1037–1041 (2010).
36. Kanevce, A. & Metzger, W. K. The role of amorphous silicon and tunneling in heterojunction with intrinsic thin layer (HIT) solar cells. *J. Appl. Phys.* **105**, 094507 (2009).
37. Zhao, L., Zhou, C. L., Li, H. L., Diao, H. W. & Wang, W. J. Design optimization of bifacial HIT solar cells on p-type silicon substrates by simulation. *Sol. Energy Mater. Sol. Cells* **92**, 673–681 (2008).
38. Parretta, A. *et al.* Angle-dependent reflectance measurements on photovoltaic materials and solar cells. *Opt. Commun.* **172**, 139–151 (1999).
39. Wang, T. H. *et al.* Effect of emitter deposition temperature on surface passivation in hot-wire chemical vapor deposited silicon heterojunction solar cells. *Thin Solid Films* **501**, 284–287 (2006).

Acknowledgments

This work was financially supported by the Norwegian Research Council, the Norwegian Micro- and Nano-Fabrication Facility, NorFab (197411/V30), the infrastructure Grant 197405 (NORTEM) program of the Research Council of Norway, and the NTNU Discovery Program.

Author contributions

F.A.M. did all the experimental work with exception of the TEM-analysis conducted by M.N. and the fibre production conducted by T.H. and J.B.; B.K.S. performed the light trapping simulations. U.J.G. conceived and supervised the project. F.A.M. and U.J.G. organized and wrote the paper with all authors contributing to the analysis and discussion of the results.

Additional information

Competing financial interests: The authors declare no competing financial interests.

How to cite this article: Martinsen, F.A. *et al.* Silicon-core glass fibres as microwire radial-junction solar cells. *Sci. Rep.* **4**, 6283; DOI:10.1038/srep06283 (2014).

Appendix B: Paper II

B.K.S. performed the experimental absorption measurements, modeling, and analysis shown in Fig. 3, and Fig. 4 (f)-(g), and was involved in the discussion and writing of some sections of the manuscript.

To be submitted.

, , , , , ,

Horizontally aligned silicon microwires as solar cells

F.A. Martinsen,[1] B.K. Smeltzer,[1] J. Ballato,[2,3] T. Hawkins,[2,3] M. Jones,[2,3] and U.J. Gibson[1]
[1)] *Department of Physics, Norwegian University of Science and Technology, N-7491 Trondheim, Norway*[a)]
[2)] *The Centre for Optical Materials Science and Engineering Technologies (COMSET), School of Material Science and Engineering, Clemson, SC 29634, USA.*
[3)] *The Centre for Optical Materials Science and Engineering Technologies (COMSET), Holocomb Department of Electrical and Computer Engineering, Clemson, SC 29634, USA.*

In this study, we demonstrate a solar cell design based on horizontally aligned microwires fabricated from 99.98% pure silicon via the molten core fibre drawing method. A structure consisting of 50 µm diameter close packed wires ($\approx$ 0.97 packing density) on a Lambertian white back-reflector showed 86 % absorption for incident light with wavelengths up to 900 nm. A structure with a packing fraction of 0.35 showed an absorption of 58 % over the same range, demonstrating the potential for effective light trapping. Prototype solar cells were fabricated with a maximum conversion efficiency of 3.5 %, where absorption in the transparent electrode and lack of backside passivation limited the efficiency. Horizontal wire cells offer several advantages as they can be made flexible and partially transparent and they absorb light efficiently over a wide range of incident angles.

The continued interest in reducing the purity requirements, kerf losses and quantity of the base material for silicon solar cells has led to the investigation of a wide range of micro and nano-structured solar designs. One such design is the vertically aligned nanowire/microwire cell which has emerged as a promising candidate for achieving high conversion efficiencies at a low cost.[1–8] The majority of these solar cells consist of vertically aligned microwires with diameters D from $\sim$ 1 µm up to $\sim$ 30 µm. These are fabricated using vapour-liquid-solid growth ($D \sim 1$ µm),[5–7,9,10] deep reactive ion etching ($D \sim 10$ µm),[3,4] high pressure chemical vapour deposition ($D \sim 10$ µm),[11] and molten core fiber drawing ($D \sim 30$ µm), and utilize a radial junction on the cylindrical surface of wires.[2,12]

Two arguments are commonly used in favour of microwire radial junction devices. First, the design allows decoupling of the light incidence and carrier collection directions,[13] and second, arrays of vertically aligned wires with a large aspect ratio can achieve a high absorption per unit of silicon.[14] The former argument implies that radial junction devices can be made from a low purity material with short minority carrier diffusion lengths, while the latter implies the need for less silicon than conventional planar solar cells. For large diameter wires the collective area of the top surface becomes comparable to that of the sidewalls.[2–4] This surface then requires standard anti-reflection treatment in order to achieve high absorption and thus negates the light trapping advantages of the radial design. As it is favourable to fabricate radial junction solar cells from wires with a low surface to volume ratio and diameters comparable to the minority carrier diffusion length,[13] alternative wire based solar configurations that can successfully utilize $\sim$ 10 µm diameter micowires with a radial junction while maintaining high light absorption are of interest.

Horizontal assemblies of (>10 µm) microwires can be used to make solar cells, similar to the μ-cell design,[15] by fabricating radial junctions and placing electrodes periodically along the length of the wires (Fig. 1(a)-(b)). When made from wires produced in macroscopically long lengths, such a design would largely eliminate kerf and polishing losses, significantly reducing the amount of silicon used compared with conventional wafer-based cells. Minority carrier extraction lengths will still be short, and if adequate light absorption is possible, this design has distinct advantages. The horizontal wire design was earlier proposed by Kelzenberg, *et al.*,[14] and Zhang, *et al.*,[16] but the small diameter of the vapour-liquid-solid-grown wires imposed a fundamental limitation in terms of low absorption values. The advent of larger diameter high pressure chemical vapour deposition structures and bulk quantities of molten core drawn wires overcomes this limitation, making it timely to re-evaluate the design.

Here we present a horizontally aligned silicon radial junction design based on microwires produced using the molten core fiber drawing method. The light trapping possibility of the structure has been assessed through simulations and experiments and the potential for realizing large scale flexible and partially transparent solar cells has been investigated. Multi-wire prototype solar cells have been fabricated and their performance has been evaluated in the context of optical measurements.

A schematic of the horizontal silicon microwire solar cell design is shown in Fig. 1(a) where wires are placed on a substrate with a spacing of 1.5 times the diameter of the wires. The contacts to the pn-junction can be fabricated as shown in Fig. 1(b), where the dark region represents the p-type crystalline core and the lighter

[a)] Electronic mail: fredrik.martinsen@ntnu.no

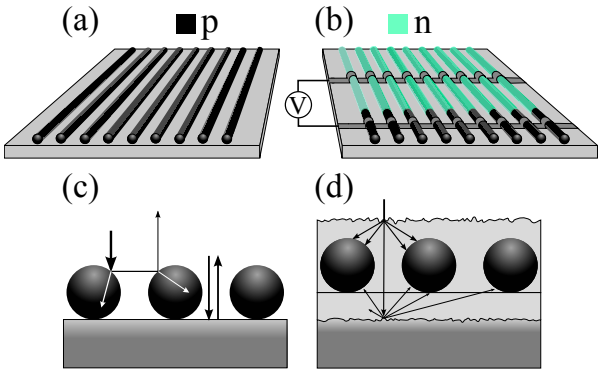

FIG. 1. An example of a solar design based on microwires placed in a horizontal array (a), where junctions and electrodes can then be fabricated periodically along the length of the microwire (b). The light trapping of the structure (c) can be improved using a scattering top surfaces and by placing the wires on or above a Lambertian reflector(d).

green region is an n-type emitter. For longer wires the electrode structure can be repeated with a periodicity determined by optimization of the device resistance, Auger recombination and other factors. For normally incident light on specular surfaces, some light will be lost to back reflection (Fig. 3(c)) or transmission, depending on the nature of the substrate, making the cell performance and transparency dependent on the packing fraction of the wires. As an avenue for increasing the light absorption in opaque designs, the wires can be placed on a Lambertian reflector so that light passing between the wires can be intercepted by a wire after reflection. This geometry can be further optimized by adding a small distance between the wires and the back reflector as well as embedding the structure in a transparent medium with a textured surface in order to scatter the light into the wires more efficiently (Fig. 3(d)).

Silica-clad silicon microwires were fabricated using the interface modifier described by Nordstrand, *et al.*,[17] via the molten core fiber drawing method[2,18–20] employing a conventional fiber tower. The silicon microwires were produced from upgraded metallurgical silicon (99.98% pure) and have been demonstrated to be of sufficient quality for solar cells due to segregation-based purification that occurs during fabrication.[2,12] For more details on the properties of the wires, the reader is referred to reference 12. Bulk quantities of wires with a silicon core to silica shell outer diameter ratio between 1:5-1:10 (Fig. 2(a)-(b)) were fabricated with core diameters between 10-200 µm (Fig. 2(c)). Microwires with sufficiently small diameter (typically $\lesssim$ 60-70 µm) are pliable as shown in Fig. 2(d) where a bend radius of $\approx$ 5 mm is demonstrated, suggesting the possibility of fabricating of flexible solar cells from these materials.

The optical absorption for the design was measured experimentally using assemblies of glass-coated silicon wires embedded in epoxy, as shown in Fig. 3(a). The samples were mounted inside an integrating sphere and irradiated by narrow bandwidth light. The portion of the light not absorbed by the structure − i.e. the reflected and transmitted components (R and T) − illuminated the sphere walls and was measured using a silicon detector mounted on a sphere port. The measured quantity $R+T$ was normalized to a Lambertian reference sample (Labsphere 6080 white reflectance coating on glass) with reflectivity between 95-98% over the measured spectral range, to account for any spurious losses. The sample absorption is thus approximately $1-R-T$. Samples were constructed by placing identical glass-clad silicon wires adjacent to each other, achieving constant centre-to-centre distance (d). The packing fraction of silicon was varied by etching the glass cladding with HF for different times. This approach was chosen instead of fully stripping the cladding and subsequently assembling a structure as it allowed for increased accuracy in controlling the distance between the wires. The wires were embedded in an optically transparent epoxy (EPO-TEK® 301), which has a refractive index similar to silica. The absorption of the samples with various d-values was measured both with and without a Lambertian back reflector (Labsphere 6080) for 0° and 45° incidence.

The sample absorption values ($1-R-T$) at a center wavelength of 750 nm are shown in Fig. 3b as a function of wire packing fraction F (wire diameter/centre-to-centre distance d). At normal incidence, without the back-reflector, the absorption scales roughly linearly with packing fraction below $F = 0.2$ with a decreasing slope as F approaches unity. Adding the back-reflector, the absorption shows a similar trend but with an overall increase of about 10-15% absolute and an asymptotic behaviour as F goes towards unity. This results in an ab-

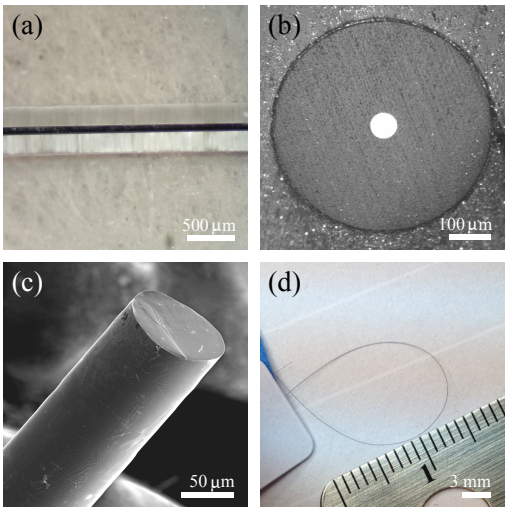

FIG. 2. Images of silica-clad silicon microwires produced using the molten core fiber drawing method. The silicon to glass ratio varies between 1:5 and 1:10 (a-b) with diameter of the silicon core measuring 10-200 µm (c). Small diameter wires can be bent through a radius of $\approx$ 5 mm (d).

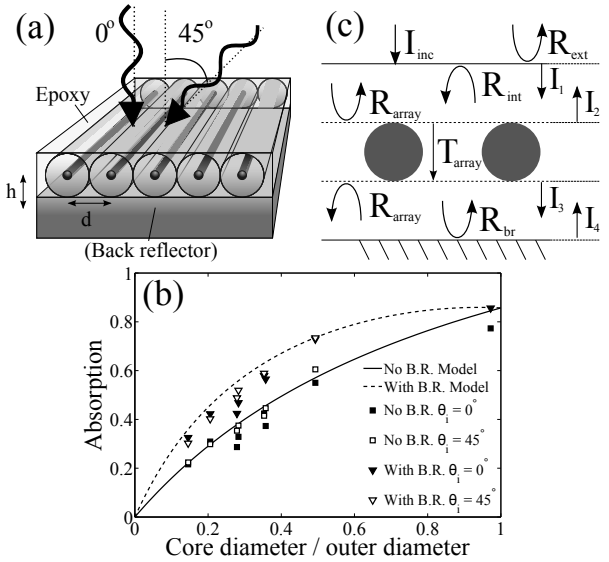

FIG. 3. Schematic of the geometry used for measuring the absorption (a) and the corresponding absorption data measured for 0° and 45° incident light with and without a Lambertian back reflector (b). The absorption was modelled as shown schematically in (c), taking into account the various reflection and transmission terms in the samples.

sorption of ≈ 86% for $F = 0.97$, while a reduction in F to 0.35 only reduced the absorption to ≈ 58%. The small reduction in absorption between $F = 0.97$ and $F = 0.35$ suggests efficient light trapping in our structures, compared to for example μ-cells, where the light absorption scales approximately linearly with packing fraction.[15] For an incidence angle of 45° without the back-reflector, a slight increase in absorption is seen over the normal incidence case, mainly because the array presents an effectively higher packing fraction. With the back-reflector in place, the light is more effectively coupled into the silicon even at normal incidence, and little change is seen when the incidence angle is changed. The measurements were repeatable to within ±2 %, re-inserting and aligning the same sample. For the $F = 0.97$ case (fully-stripped wires) the beam overfilled the sample at 45° incidence, thus this data point is omitted.

A self-consistent approach similar to that described by Gee[21] was used to model the performance of the wire arrays at 0° incidence as a function of F. The array reflection and transmission coefficients shown in Fig. 3(c) were calculated using the optical constants of Si, assuming the wires were embedded in a medium of refractive index $n = 1.5$. Direct wire-to-wire coupling of light was neglected for simplicity, such that $R_{\rm array} = R_{\rm Si}F$, and $T_{\rm array} = 1 - F$, where $R_{\rm Si}$ is the weighted angular average of Si reflectance. The reflectance of the outer epoxy-glass surface $R_{\rm ext}$ was assumed to be 4% and the internal surface reflectance $R_{\rm int} = 0.57$ was calculated assuming the reflected light from the silicon (and back-reflector) is isotropic, following Gee.[21] The back-surface reflectance was 97% for the Lambertian coating, and 57% ($R_{\rm int}$) without the back-reflector. As the structures are too large to give interference effects, the intensities I_{1-4} shown in Fig. 3 (c) can be expressed as:

$$I_1 = (1 - R_{\rm ext})I_{\rm inc} + R_{\rm int}I_2, \quad (1a)$$

$$I_2 = R_{\rm array}I_1 + T_{\rm array}I_4, \quad (1b)$$

$$I_3 = T_{\rm array}I_1 + R_{\rm array}I_4, \quad (1c)$$

$$I_4 = R_{\rm br}I_3. \quad (1d)$$

For visible wavelengths where the light is fully absorbed in one pass through the wires, the array absorption is $A_{\rm array} = (1 - R_{\rm array} - T_{\rm array})(I_1 + I_4)$. This curve is plotted with and without a back-reflector in Fig. 3(b). The model reproduces the behaviour of the experimental data, and provides a reasonable fit although it overestimates the absorption at small packing fractions.

Prototype multi-wire solar cells ≈ 2 mm long, based on the intrinsic thin layer (HIT) design were fabricated from 6-8 wires with diameters of ≈ 50 µm (Fig. 4(a)-(d)). Wires were mounted with epoxy close packed on a silicon nitride coated glass substrate (Fig. 4(c)) and then cleaned using a piranha solution (3:1 H_2SO_4:H_2O_2) followed by 5% HF before the contact to the p-type core was applied through e-beam evaporation of 500 nm aluminium under a vacuum better than 10^{-7} torr. The piranha etch was kept short (∼ 2 s) in order to clean the exposed parts of the wires, illustrated in Fig. 4(c), without over-etching the epoxy and removing the wires from the substrate. To fabricate the junction, the area of the wires contacted with aluminium was masked using photoresist followed by an HF dip (5 % HF) and subsequent deposition of ≈ 7 nm of intrinsic amorphous silicon, overcoated with ≈ 25 nm of phosphorous-doped amorphous silicon at 150° C (Fig.4(c)-(d)) using plasma enhanced chemical vapour deposition (PECVD). A relatively thick amorphous layer compared with that used in standard planar HIT-cells[22,23] was applied to ensure full coating of the areas of the silicon surface close to the wire edges. The amorphous emitter was subsequently contacted using 80 nm of sputter deposited indium-tin oxide (ITO ρ = $1.7{\cdot}10^{-3}$ Ω·cm) deposited in an 5 mTorr ambient consisting of 2% oxygen in argon at a substrate temperature of 100° C. Lift-off of the photoresist and ITO from the aluminium contact regions was then performed and the solar cells were measured at room temperature under AM 1.5G illumination using an indium-gallium eutectic for a contact to the ITO. The resulting I-V curves from the ≈ 2 mm long 6 wire champion cell taken under dark and illuminated conditions are shown in Fig. 4(e). Normalized to the illuminated area, the cell showed a V_{oc} of 400 mV, a J_{sc} of 17.4 mA·cm^{-2} and a 0.51 fill factor, resulting in a 3.5% conversion efficiency. While the cells were fabricated on a rigid glass substrate, it is worth noting that the low temperature processes and pliable wires (Figure 2d)are compatible with a polymer substrate. Extension of this fabrication method to formation of flexible solar cells may thus be possible.

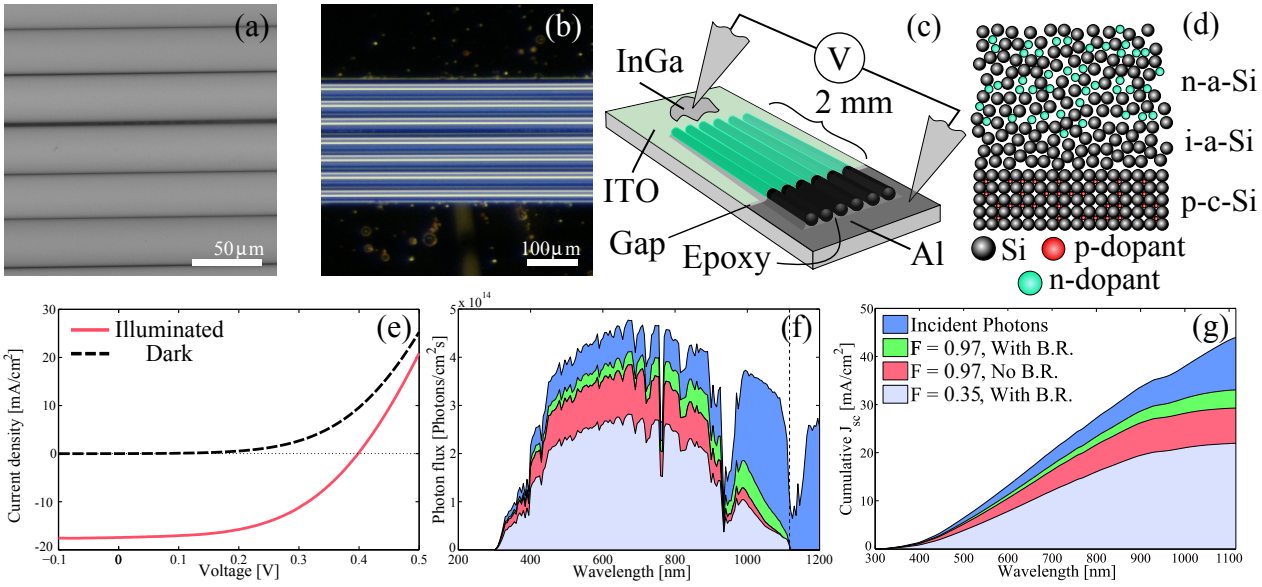

FIG. 4. Scanning electron (a) and optical micrograph (b) of a wire assembly. Schematic of the cell structure (c) and the junction formed by PECVD deposition of amorphous silicon (d). I-V characteristics of a cell made from 6 wires with an average diameter of 50 µm(e). The spectral absorption of a $F = 0.97$ and $F = 0.35$ sample are presented in (f); without a back reflector this was found to absorb 67 % of the light in the relevant part of the solar spectrum (g).

In the demonstrated solar device structure the wires were mounted close-packed onto a glass substrate using epoxy (illustrated schematically in Fig 4(c)), resulting in the pn-junction, and thus surface passivation, only being applied to approximately half of the wire surface. Earlier measurements of the recombination velocity on similar wires showed a reduction from $\sim$ 10000 cm·s^{-1} for non-passivated surfaces to $\sim$ 500 cm·s^{-1} for surfaces passivated with intrinsic amorphous silicon.[12] This is believed to be the main cause of the low observed V_{oc}. The fill factor of 0.51 is indicative of a high series resistance together with the presence of non-infinite shunt, with the former partly caused by the relatively resistant ITO layer ($\sim$ 1 Ω·cm^2 per mm) and the contact resistance (measured to $\approx$ 0.5 Ω·cm^2). With a wire resistivity of 0.3-0.9 Ω·cm,[12] the series resistance contribution from the wires themselves is between 0.06 and 0.18 Ω·cm^2, and thus negligible compared with the other values in this device.

In order to interpret the observed J_{sc}, the absorption performance of the $F = 0.97$ structure presented in Fig. 3(b) was measured as a function of wavelength at 0° incidence without a Lambertian back reflector (red curve in Fig. 4(f)). Assuming a 100% internal quantum efficiency (IQE), the measured absorption was weighted by the solar spectral photon flux density in order to obtain the upper bound on the J_{sc} for this geometry. The resulting value for the cumulative J_{sc} as a function of wavelength is shown in Fig. 4(g). Based on the measured absorption, the calculated maximum J_{sc} for the $F = 0.97$ structure without a back-reflector was $\approx$ 29 mA·cm^{-2} (external quantum efficiency (EQE) of $\approx$ 67 %), a value comparable to that obtained for ultra-thin planar silicon wafers.[24] The measured value of 17.4 mA·cm^{-2}, which includes parasitic absorption of light in the ITO and amorphous layers, then gives a lower bound of 0.6 for the IQE in our prototype device.

A similar measurement performed with a back-reflector (assuming an IQE = 1) for $F = 0.35$ and $F = 0.97$ resulted in J_{sc}-limits of 22 mA·cm^{-2} and 33 mA·cm^{-2} respectively. These corresponds to an EQE of 0.5 and 0.75 respectively, indicating that a reduction in silicon of $\approx$ 64 % only reduces the integrated light absorption by $\approx$ 33 %. Fig. 4(f) shows that the single wavelength absorption values presented in Fig. 3(c) agree well with the spectral absorption up to around 900 nm, but from 900 nm to the band gap ($\approx$ 1100 nm) the absorption drops off for both configurations. The addition of an anti-reflective coating, together with improved randomization of the light inside the structure from more Lambertian-like front and back surfaces, or the introduction of scattering centres in the host matrix may be expected to further increase the overall light absorption of the structure.

In conclusion we have shown that horizontally aligned silicon microwires produced via the molten core fiber pulling method have the potential to be employed as viable solar cells. The efficiency of the presented prototype was low due to the lack of process optimization, with surface recombination and series resistance believed to be the main limiting factors. The close packed array was shown to absorb $\approx$ 86 % of the light for wavelengths up to about 900 nm while a reduction of the packing fraction to 0.35 only reduced this absorption to 58 %. The horizontal structure shows similar absorptions both for 0° and 45° incidence, suggesting that the light absorp-

tion in this design is largely independent of the incident angle.

This work was financially supported by the Norwegian Research Council, the Norwegian Micro- and Nano-Fabrication Facility, NorFab (197411/V30), and the NTNU Discovery Program.

[1] N. Guo, J. Wei, Q. Shu, Y. Jia, Z. Li, K.Zhang, H. Zhu, K. Wang, S. Song, Y. Xu, and D. Wu, Appl. Phys. A **102**, 109 (2011).
[2] F. Martinsen, B. K. Smeltzer, M. Nord, T. Hawkins, J. Ballato, and U. Gibson, Sci. Rep. **4**, 6283 (2014).
[3] M. Gharghi, E. Fathi, B. Kante, S. Sivoththaman, and X. Zhang, Nano Lett. **20**, 6278 (2012).
[4] H. Yoon, Y. Yuwen, C. Kendrick, G. Barber, N. Podraza, J. Redwing, T. Mallouk, C. Wronski, and T. Mayer, Appl. Phys. Lett. **96**, 213503 (2010).
[5] M. D. Kelzenberg, D. B. Turner-Evans, M. C. Putnam, S. W. Boettcher, R. M. Briggs, R. Briggs, J. Baek, N. S. Lewis, and H. A. Atwater, Energy Environ. Sci. **4**, 866 (2011).
[6] M. Kelzenberg, D. Turner-Evans, B. Kayes, M. Filler, M. Putnam, N. Lewis, and H. Atwater, Nano Lett. **8**, 710 (2008).
[7] M. C. Putnam, S. W. Boettcher, M. D. Kelzenberg, D. B. Turner-Evans, J. Spurgeon, E. L. Warren, R. M. Briggs, N. S. lewis, and H. A. Atwater, Energy Environ. Sci. **3**, 1037 (2010).
[8] D. R. Kim, C. H. Lee, P. M. Rao, I. S. Cho, and X. Zheng, Nano Lett. **11**, 2704 (2011).
[9] O. Gunawan and S. Guha, Sol. Energy Mater. Sol. Cells **93**, 1388 (2009).
[10] B. Tian, X. Zheng, T. J. Kempa, Y. Fang, N. Yu, J. Huang, and C. M. Lieber, Nature **449**, 885 (2007).
[11] R. He, T. Day, M.Krishnamurthi, J. Sparks, P. Sazio, V. Gopalan, and J. Badding, Adv. Mater. **25**, 1461 (2013).
[12] F. Martinsen, T. Hawkins, J. Ballato, and U. Gibson, APL Mat. **2**, 116108 (2014).
[13] B. Kayes, H. Atwater, and N. Lewis, J. Appl. Phys. **97**, 114302 (2005).
[14] M. D. Kelzenberg, S. W. Boettcher, J. A. Petykiewicz, D. B. Turner-Evans, M. C. Putnam, E. L. Warren, J. M. Spurgeon, R. M. Briggs, N. S. Lewis, and H. A. Atwater, Nat. Mater. **9**, 239 (2010).
[15] J. Y. et al., Nature Mat. **7**, 907 (2008).
[16] X. Zhang, C. W. Pinion, J. D. Christesen, C. J. Flynn, T. A. Celano, and J. F. Cahoon, J. Phys. Chem. Lett. **4**, 2002 (2013).
[17] E. Nordstrand, A. N. Dibbs, A. J. Eraker, and U. Gibson, Opt. Mater. Express **3**, 651 (2013).
[18] J. Ballato, T. Hawkins, P. Foy, R. Stolen, B. Kokouz, M. Ellison, C. McMillen, J. Reppert, A. Rao, M. Daw, S. Sharma, R. Shori, O. Stafsudd, R. R. Rice, and D. Powers, Opt. Express **16**, 18675 (2008).
[19] B. L. Scott, K. Wang, and G. Pickrell, IEEE Photonics Technol. Lett. **21**, 1798 (2009).
[20] C. Hou, X. Jia, L. Wei, S. Tan, X. Zhao, J. D. Joannopoulos, and Y. Fink, Nat. Commun. **6**, 6248 (2015).
[21] J. Gee, Proc. of the 20th IEEE Photovoltaic Spec. Conf. **1**, 549 (1988).
[22] T. Wang, E. Iwaniczko, M. Page, D. Levi, Y. Yan, H. Branz, and Q. Wang, Thin Solid Films **501**, 284 (2006).
[23] V. Dao, J. Heo, H. Choi, Y. Kim, S. Park, S. Jung, N. Lakshminarayan, and J. Yi, Sol. Energy **84**, 777 (2010).
[24] M. Hilali, S. Saha, E. Onyegam, R. Rao, L. Mathew, and S. Banerjee, Appl. Opt. **53**, 6140 (2014).

Appendix C

The 2D and 3D ray tracing code written in MATLAB is included here.

```
function [Ray_R, Ray_T, tMax, Abs, DiffR] = ...
    ray_iteration(B,Ray,n0,verbose)

if ¬exist('verbose','var')
    verbose = 1;
end

%Set the default polarization:
if ¬isfield(Ray,'Pol')
    Ray.Pol = 'S';
end

if ¬isfield(Ray,'Lambda')
    fprintf('WARNING: Wavelength not set, absorption coefficient ...
        will be set to zero.\n')
    Ray.Lambda = Inf;
end

DiffR = [];

delR = 1e-9;%Tolerance used to offset generated reflected and ...
    transitted rays from material boundary.

R0 = Ray.R0;
dR0 = Ray.dR0;


tMin = Inf; %Set an initial value of the miniumun ray ...
    parametrization variable
iInt = NaN; %Initial value of the index into the boundary line ...
    segments.
jMin = NaN;
flag = 0;
%%%%%%%%%%%%%%%%%%%%%%%%%%%%%%%%%%%%%%%%%%%%%%%%%%%%%%%%%%%%%%%
%Find the intersection points with all boundaries.
for j = 1:numel(B)
    P = B(j).P;

```

```
34      dP = P(:,2:end) - P(:,1:end-1);
35      dP(:,end+1) = P(:,1) - P(:,end);
36
37      %Calculate the unit vector normal to the surface (pointing out).
38      nHat = [dP(2,:); -dP(1,:)];
39      nHat = nHat ./ repmat(sqrt(sum(nHat.^2,1)),[2 1]);
40
41      R1 = reshape(P,[2 1 size(P,2)]);
42      dR1 = reshape(dP,[2 1 size(P,2)]);
43
44      R0p = repmat(R0,[1 1 size(R1,3)]);
45      dR0p = repmat(dR0,[1 1 size(dR1,3)]);
46
47      A = [dR0p(1,:,:) -dR1(1,:,:); dR0p(2,:,:) -dR1(2,:,:)];
48
49      detA = 1 ./ ( -dR0(1).*dR1(2,:,:) + dR1(1,:,:).*dR0(2) ) ;
50      invA = repmat(detA,[2 2]) .* [-dR1(2,:,:) dR1(1,:,:); ...
           -dR0p(2,:,:) dR0p(1,:,:)];
51
52
53      b = [R1(1,:,:) - R0p(1,:,:); R1(2,:,:) - R0p(2,:,:)];
54
55      t = [...
56          b(1,:,:).*invA(1,1,:) + b(2,:,:).*invA(1,2,:);...
57          b(1,:,:).*invA(2,1,:) + b(2,:,:).*invA(2,2,:)];
58
59
60
61      IntR0j = squeeze(R0p + repmat(t(1,:,:),[2 1]).*dR0p);
62      IntR1 = squeeze(R1 +  repmat(t(2,:,:),[2 1]).*dR1);
63
64      IntR0j(2,squeeze(t(2,:,:) <0 | t(2,:,:) > 1)) = NaN;
65      t(1,isnan(IntR0j(2,:))) = NaN;
66      t(1,t(1,:,:) < 0) = NaN;
67      [tMinj,iIntj] = min(t(1,:));
68
69      if tMinj < tMin
70          tMin = tMinj;
71          iInt = iIntj;
72          IntR0 = IntR0j;
73          jMin = j;
74      elseif tMin == tMinj
75          flag = 1;%Raise a flag if the ray intersects two line ...
               segments at the same point (abutting boundaries)
76          j2 = j;
77      end
78
79
80  end
81
82  if ¬isfinite(tMin)
83      Ray_R = [];
84      Ray_T = [];
```

```
85      tMax = NaN;
86      Abs = NaN;
87      return;
88  end
89
90  P = B(jMin).P;
91  nP = B(jMin).n; %The material index of refraction
92
93  dP = P(:,2:end) - P(:,1:end-1);
94  dP(:,end+1) = P(:,1) - P(:,end);
95  nHat = [dP(2,:); -dP(1,:)];
96  nHat = nHat ./ repmat(sqrt(sum(nHat.^2,1)),[2 1]);
97  %%%%%%%%%%%%%%%%%%%%%%%%%%%%%%%%%%%%%%%%%%%%%%%%%%%%%%%%%%%%%%%%%%%%%%%%%%%%%%%
98  %Using the boundary that the ray intersects first, build the ...
        appropriate
99  %reflected and transmitted rays.
100
101 if flag
102     n0 = B(j2).n;
103 end
104
105 %Now calculate the reflected ray.
106 di = -dR0 / norm(dR0);
107 dn = nHat(:,iInt);
108
109 %Determine whether the ray is entering or leaving the material.
110 dl = dP(:,iInt);
111 cs = dl(1)*dR0(2) - dl(2)*dR0(1);
112
113 dn = dn * cs / abs(cs);
114
115 if cs > 0
116     %The ray is entering:
117     ni = n0;
118     nt = nP;
119     alpha = imag(ni)*4*pi/Ray.Lambda;
120
121 else
122     %The ray is leaving:
123     ni = nP;
124     nt = n0;
125     alpha = imag(ni)*4*pi/Ray.Lambda;
126
127     if isfield(B(jMin),'alpha')
128         if numel(B(jMin).alpha) > 0
129             alpha = B(jMin).alpha;
130         end
131     end
132
133
134 end
135
136
```

```
137 %Unit vector pointing in the direction of the reflected ray.
138 dr = 2*(dot(dn,di))*dn - di;
139 Rref = IntR0(:,iInt);
140 dRref = dr * norm(dR0);
141
142 %Unit vector pointing in the direction of the transmitted ray.
143 cos1 = dot(dn,di);
144 cos2 = sqrt(1 - abs(ni/nt)^2*(1-cos1^2));
145
146 dtr = -real(ni/nt)*di + (real(ni/nt)*cos1 - cos2)*dn;
147 Rtran = IntR0(:,iInt);
148 dRtran = dtr * norm(dR0);
149
150
151 %Calculate the reflection coefficients:
152 cosTh_i = abs(dot(di,dn))/(norm(dn)*norm(di));
153 Th_i = acos(cosTh_i);
154 Th_t = asin(sin(Th_i)*ni/nt);
155 cosTh_t = cos(Th_t);
156
157 %cosTh_t = abs(dot(dtr,dn))/(norm(dn)*norm(dtr));
158
159 rS = (ni*cosTh_i - nt*cosTh_t) / (ni*cosTh_i + ...
       nt*cosTh_t);%S-polarization
160 rP = (ni*cosTh_t - nt*cosTh_i) / (ni*cosTh_t + ...
       nt*cosTh_i);%P-polarization
161
162 switch Ray.Pol
163     case 'S'
164         r = rS;
165     case 'P'
166         r = rP;
167     case 'Unpol'
168         r = sqrt( (abs(rS).^2 + abs(rP).^2) / 2.0 );
169 end
170
171
172 %If the user has entered a reflection coefficient manually, use ...
       that one.
173 if isfield(B(jMin),'Reflection')
174
175     if ~isnan(B(jMin).Reflection(iInt))
176         r = sqrt(B(jMin).Reflection(iInt));
177     end
178
179     %Furthermore, if the user has entered a negative value for the
180     %reflection coefficient, send back diffuse reflected rays.
181
182     if B(jMin).Reflection(iInt) < 0
183         nDiff = 7;
184         dphiDiff = pi / (nDiff + 1);
185         theta_vals = (dphiDiff:dphiDiff:pi-dphiDiff) - pi/2;
186
```

```
187         %normConst = sum(cos(theta_vals));
188         normConst = numel(theta_vals);
189
190         for jj = 1:nDiff
191
192             rayDir = [dn(1)*cos(theta_vals(jj)) - ...
                    dn(2)*sin(theta_vals(jj));...
193                  dn(1)*sin(theta_vals(jj)) + ...
                        dn(2)*cos(theta_vals(jj))];
194
195             DiffR(end+1).R0 = Rref + delR*dn;
196             %DiffR(end).dR0 = ...
                    norm(dR0)*cos(theta_vals(jj))/normConst*rayDir;
197             DiffR(end).dR0 = norm(dR0)/normConst*rayDir;
198             DiffR(end).Lambda = Ray.Lambda;
199             DiffR(end).Pol = Ray.Pol;
200         end
201
202         Ray_R.R0 = Rref + delR*dn;
203         Ray_R.dR0 = dRref*0;
204         Ray_R.Lambda = Ray.Lambda;
205         Ray_R.Pol = Ray.Pol;
206
207         Ray_T.R0 = Rtran - delR*dn;
208         Ray_T.dR0 = dRtran*0;
209         Ray_T.Lambda = Ray.Lambda;
210         Ray_T.Pol = Ray.Pol;
211         tMax = tMin;
212         Abs = 0;%NEED TO CHANGE AT SOME POINT ...
                ************************
213
214         return;
215     end
216
217
218
219 end
220
221
222
223 %Apply the reflection and transmission coefficients, and the ...
       absorption:
224 tMax = tMin;
225 d = norm(Ray.dR0 * tMax);
226 Abs = 1 - exp(-alpha*d);
227
228 dRref = dRref * abs(r)^2 * exp(-alpha*d);
229 dRtran = dRtran * (1 - abs(r)^2) * exp(-alpha*d);
230
231 if imag(dot(dRtran,dn)) > 0
232     dRtran = 0 * dRtran;
233     dRref = dr * norm(dR0) * exp(-alpha*d);
234 end
```

```
235
236 Ray_R.R0 = Rref + delR*dn;
237 Ray_R.dR0 = dRref;
238 Ray_R.Lambda = Ray.Lambda;
239 Ray_R.Pol = Ray.Pol;
240
241 Ray_T.R0 = Rtran - delR*dn;
242 Ray_T.dR0 = dRtran;
243 Ray_T.Lambda = Ray.Lambda;
244 Ray_T.Pol = Ray.Pol;
245
246 svec = [0 tMax];
247
248 %Plot the results.
249 if verbose
250     figure(1);plot(...
251         [P(1,:) P(1,1)],[P(2,:) P(2,1)],...
252         R0(1,:) + svec*dR0(1,:), R0(2,:) + svec*dR0(2,:),'-g',...
253         Rref(1,:) + svec*dRref(1,:), Rref(2,:) + ...
                svec*dRref(2,:),'-k',...
254         Rtran(1,:) + svec*dRtran(1,:), Rtran(2,:) + ...
                svec*dRtran(2,:),'-r',...
255         IntR0(1,iInt),IntR0(2,iInt),'xr');
256     legend('Material Boundary','Incident Ray','Reflected ...
            Ray','Transmitted Ray');
257     axis equal;
258 end
259
260
261 end
```

```
1  function allRays = ray_propagation(B,Ray,n0,nSteps,Limits)
2
3  if ~exist('Limits','var')
4      Limits = [-Inf Inf -Inf Inf];
5  end;
6
7
8  %Set the default polarization:
9  if ~isfield(Ray,'Pol')
10     Ray.Pol = 'S';
11 end
12
13 %Run some checks and prepare the input B structure.
14
15 for i = 1:numel(B)
16    if isfield(B(i),'Reflection')
17       if numel(B(i).Reflection) == 0
18           B(i).Reflection = NaN * ones(1,size(B(i).P,2));
19       end
20
```

```
21      end
22  end
23
24
25  threshold = 1e-3;
26
27  allRays = Ray;
28  allRays.tMax = NaN;
29  allRays.Abs = NaN;
30  allRays.Pol = '';
31  currRays = Ray;
32
33  for i = 1:nSteps
34      %Intialize the structure.
35      newRays = [];
36      newRays.R0 = 0;
37      newRays.dR0 = 0;
38      newRays.Lambda = 0;
39      newRays.Pol = '';
40
41      %tic;
42      %numel(currRays)
43      for j = 1:numel(currRays)
44          [Rj, Tj, tMax, Abs, diffR] = ...
                ray_iteration(B,currRays(j),n0,0);
45          currRays(j).tMax = tMax;
46          currRays(j).Abs = Abs * norm(currRays(j).dR0);
47
48
49          if ¬isnan(tMax) && limits_test(Rj,Limits)
50              if norm(Rj.dR0)≥threshold
51                  newRays(end+1) = Rj;
52              end
53
54              if norm(Tj.dR0)≥threshold
55                  newRays(end+1) = Tj;
56              end
57
58              if numel(diffR) > 0
59                  for ii = 1:numel(diffR)
60                      if norm(diffR(ii).dR0)≥threshold
61                          newRays(end+1) = diffR(ii);
62                      end
63
64
65                  end
66
67
68
69              end
70
71
72          end
```

```
73
74      end
75
76
77
78      newRays = newRays(2:end);
79      allRays = [allRays, currRays];
80
81      if numel(newRays) ==0
82          break;
83      end
84
85      currRays = newRays;
86      %toc;
87   %plotRays(B,allRays);
88   %pause(0.3);
89  end
90
91  allRays = allRays(2:end);
92  plotRays(B,allRays);
93
94  end
95
96
97  function tf = limits_test(Ray,Limits)
98
99  tol = 1e-9;%Hardcoded parameter in 'ray_iteration' should be ...
        changed accordingly.
100 tf = 1;
101
102 xTest = abs(Ray.R0(1) - Limits(1))<=tol || abs(Ray.R0(1) - ...
        Limits(2))<=tol;
103 yTest = abs(Ray.R0(2) - Limits(3))<=tol || abs(Ray.R0(2) - ...
        Limits(4))<=tol;
104
105 if xTest || yTest
106     tf = 0;
107 end
108
109
110 end
111
112
113 function plotRays(B,Rays)
114
115
116 cmap = colormap;
117 nc = size(cmap,1);
118
119 for j = 1:numel(B)
120     figure(2);plot(...
121         [B(j).P(1,:) B(j).P(1,1)],[B(j).P(2,:) B(j).P(2,1)],'k');
122     hold on;
```

```
123 end
124
125 for i = 1:numel(Rays);
126 %     if isnan(Rays(i).Abs)
127 %         continue;
128 %     elseif norm(Rays(i).dR0) < 20e-3
129 %         continue;
130 %     end
131 if norm(Rays(i).dR0) < 20e-3
132     continue;
133 elseif isnan(Rays(i).Abs)
134     Rays(i).tMax = 1/norm(Rays(i).dR0)*50;
135 end
136     X = [Rays(i).R0(1), Rays(i).R0(1) + Rays(i).tMax * ...
            Rays(i).dR0(1)];
137     Y = [Rays(i).R0(2), Rays(i).R0(2) + Rays(i).tMax * ...
            Rays(i).dR0(2)];
138     dn = 0.03;
139     nhat = [-diff(Y) diff(X)];
140     nhat = nhat / norm(nhat);
141
142     %Parameters for the arrow heads
143     arrowAngle = 15;%Deg.
144     arrowL = 5;%Length of arrow in plot units.
145
146     Mrot = @(theta) [cos(theta) -sin(theta); sin(theta) cos(theta)];
147
148     R1 = Mrot(arrowAngle*pi/180) * [-diff(X); -diff(Y)];R1 = ...
            R1/norm(R1)*arrowL;
149     R2 = Mrot(-arrowAngle*pi/180) * [-diff(X); -diff(Y)];R2 = ...
            R2/norm(R2)*arrowL;
150
151     iclr = max(1,round(norm(Rays(i).dR0) * nc));
152     rayColor = cmap(iclr,:);
153     plot(X,Y,'Color',rayColor);
154     %Now make arrowheads.
155
156     plot(X(2)+[0 R1(1)],Y(2)+[0 R1(2)],'Color',rayColor);
157     plot(X(2)+[0 R2(1)],Y(2)+[0 R2(2)],'Color',rayColor);
158
159
160 %     if Rays(i).Abs > 0
161 %         text(mean(X) + dn*nhat(1),mean(Y) + dn*nhat(2),...
162 %             sprintf('%.3f',Rays(i).Abs),'Color','g');
163 %         text(X(1) + dn*nhat(1),Y(1) + dn*nhat(2),...
164 %             sprintf('%.3f',norm(Rays(i).dR0)),'Color','k');
165 %     end
166 end
167 hold off;
168 xlabel('X');ylabel('Z');
169 drawnow;
170
171 end
```

```
function [Ray_R, Ray_T, tMax, Abs, DiffR] = ...
    ray_iteration_3D(B,Ray,n0,verbose)

if ¬exist('verbose','var')
    verbose = 1;
end

%Set the default polarization:
if ¬isfield(Ray,'Pol')
    Ray.Pol = 'S';
end

if ¬isfield(Ray,'Lambda')
    fprintf('WARNING: Wavelength not set, absorption coefficient ...
       will be set to zero.\n')
    Ray.Lambda = Inf;
end

DiffR = [];

delR = 1e-9;%Tolerance used to offset generated reflected and ...
    transitted rays from material boundary.

R0 = Ray.R0;
dR0 = Ray.dR0;


tMin = Inf; %Set an initial value of the miniumun ray ...
    parametrization variable
iInt = NaN; %Initial value of the index into the boundary line ...
    segments.
jMin = NaN;
flag = 0;
%%%%%%%%%%%%%%%%%%%%%%%%%%%%%%%%%%%%%%%%%%%%%%%%%%%%%%%%%%%%%%%%
%Find the intersection points with all boundaries.
for j = 1:numel(B)

    A = [-dR0, B(j).a1, B(j).a2];
    b = R0 - B(j).p0;

    if isfinite(cond(A))

        tt = A^(-1)*b;
    else
        tt = NaN*[1;1;1];
    end
    tMinj = tt(1);
    IntR0j = R0 + tMinj * dR0;

    %Now we check if the intersection with the plane is within ...
       limits.
    if ¬all(B(j).c_i*tt(3) ≤ B(j).m_i*tt(2) + B(j).b_i)
        tMinj = NaN;
```

```
    end

    if tMinj < 0;
        tMinj = NaN;
    end

    if tMinj < tMin
        tMin = tMinj;
        %iInt = iIntj;
        IntR0 = IntR0j;
        jMin = j;
    elseif tMin == tMinj
        flag = 1;%Raise a flag if the ray intersects two line ...
           segments at the same point (abutting boundaries)
        j2 = j;
    end


end

if ¬isfinite(tMin)
    Ray_R = [];
    Ray_T = [];
    tMax = NaN;
    Abs = NaN;
    return;
end


a1 = B(jMin).a1;
a2 = B(jMin).a2;
p0 = B(jMin).p0;
dn = cross(a1,a2);dn = dn/norm(dn);
nP = B(jMin).n;

%%%%%%%%%%%%%%%%%%%%%%%%%%%%%%%%%%%%%%%%%%%%%%%%%%%%%%%%%%%%%%%%%%%%%%%%%%%
%Using the boundary that the ray intersects first, build the ...
   appropriate
%reflected and transmitted rays.

if flag
    n0 = B(j2).n;
end

%Now calculate the reflected ray.
di = -dR0 / norm(dR0);

%Determine whether the ray is entering or leaving the material.
%dl = dP(:,iInt);
%cs = dl(1)*dR0(2) - dl(2)*dR0(1);
cs = dot(dn,di);

dn = dn * cs / abs(cs);
```

```
99
100 if cs > 0
101     %The ray is entering:
102     ni = n0;
103     nt = nP;
104     alpha = imag(ni)*4*pi/Ray.Lambda;
105
106 else
107     %The ray is leaving:
108     ni = nP;
109     nt = n0;
110     alpha = imag(ni)*4*pi/Ray.Lambda;
111
112     if isfield(B(jMin),'alpha')
113         if numel(B(jMin).alpha) > 0
114             alpha = B(jMin).alpha;
115         end
116     end
117
118
119 end
120
121
122 %Unit vector pointing in the direction of the reflected ray.
123 dr = 2*(dot(dn,di))*dn - di;
124 Rref = IntR0;
125 dRref = dr * norm(dR0);
126
127 %Unit vector pointing in the direction of the transmitted ray.
128 cos1 = dot(dn,di);
129 cos2 = sqrt(1 - abs(ni/nt)^2*(1-cos1^2));
130
131 dtr = -real(ni/nt)*di + (real(ni/nt)*cos1 - cos2)*dn;
132 Rtran = IntR0;
133 dRtran = dtr * norm(dR0);
134
135
136 %Calculate the reflection coefficients:
137 cosTh_i = abs(dot(di,dn))/(norm(dn)*norm(di));
138
139 Th_i = acos(cosTh_i);
140 Th_t = asin(sin(Th_i)*ni/nt);
141 cosTh_t = cos(Th_t);
142
143 %cosTh_t = abs(dot(dtr,dn))/(norm(dn)*norm(dtr));
144
145 rS = (ni*cosTh_i - nt*cosTh_t) / (ni*cosTh_i + ...
       nt*cosTh_t);%S-polarization
146 rP = (ni*cosTh_t - nt*cosTh_i) / (ni*cosTh_t + ...
       nt*cosTh_i);%P-polarization
147
148 switch Ray.Pol
149     case 'S'
```

```
150         r = rS;
151     case 'P'
152         r = rP;
153     case 'Unpol'
154         r = sqrt( (abs(rS).^2 + abs(rP).^2) / 2.0 );
155 end
156
157 %If the user has entered a reflection coefficient manually, use ...
       that one.
158 if isfield(B(jMin),'Reflection')
159
160     if ¬isnan(B(jMin).Reflection)
161         r = sqrt(B(jMin).Reflection);
162     end
163
164     if B(jMin).Reflection < 0
165
166
167
168         DiffR = lambertian_3D_rays(B(jMin),Ray,Rref + delR*dn);
169
170
171         Ray_R.R0 = Rref + delR*dn;
172         Ray_R.dR0 = dRref*0;
173         Ray_R.Lambda = Ray.Lambda;
174         Ray_R.Pol = Ray.Pol;
175
176         Ray_T.R0 = Rtran - delR*dn;
177         Ray_T.dR0 = dRtran*0;
178         Ray_T.Lambda = Ray.Lambda;
179         Ray_T.Pol = Ray.Pol;
180         tMax = tMin;
181         Abs = 0;%NEED TO CHANGE AT SOME POINT ...
               ************************
182
183         return;
184
185
186     end
187
188 end
189
190 %Apply the reflection and transmission coefficients, and the ...
       absorption:
191 tMax = tMin;
192 d = norm(Ray.dR0 * tMax);
193 Abs = 1 - exp(-alpha*d);
194
195 dRref = dRref * abs(r)^2 * exp(-alpha*d);
196 dRtran = dRtran * (1 - abs(r)^2) * exp(-alpha*d);
197
198 if imag(dot(dRtran,dn)) > 0
199     dRtran = 0 * dRtran;
```

```
200     dRref = dr * norm(dR0) * exp(-alpha*d);
201 end
202
203 Ray_R.R0 = Rref + delR*dn;
204 Ray_R.dR0 = dRref;
205 Ray_R.Lambda = Ray.Lambda;
206 Ray_R.Pol = Ray.Pol;
207
208 Ray_T.R0 = Rtran - delR*dn;
209 Ray_T.dR0 = dRtran;
210 Ray_T.Lambda = Ray.Lambda;
211 Ray_T.Pol = Ray.Pol;
212
213 svec = [0 tMax];
214
215 %Plot the results.
216 if verbose
217     figure(1);plot(...
218         [P(1,:) P(1,1)],[P(2,:) P(2,1)],...
219         R0(1,:) + svec*dR0(1,:), R0(2,:) + svec*dR0(2,:),'-g',...
220         Rref(1,:) + svec*dRref(1,:), Rref(2,:) + ...
                svec*dRref(2,:),'-k',...
221         Rtran(1,:) + svec*dRtran(1,:), Rtran(2,:) + ...
                svec*dRtran(2,:),'-r',...
222         IntR0(1,iInt),IntR0(2,iInt),'xr');
223     legend('Material Boundary','Incident Ray','Reflected ...
            Ray','Transmitted Ray');
224     axis equal;
225 end
226
227
228 end
```

```
1  function allRays = ray_propagation_3D(B,Ray,n0,nSteps,Limits)
2  %
3  % if ~exist('Limits','var')
4  %     Limits = [-Inf Inf -Inf Inf];
5  % end;
6
7  warning('off','MATLAB:singularMatrix');
8  warning('off','MATLAB:nearlySingularMatrix');
9
10 diffR = [];
11 %Set the default polarization:
12 if ~isfield(Ray,'Pol')
13     Ray.Pol = 'S';
14 end
15
16 %Run some checks and prepare the input B structure.
17
18 for i = 1:numel(B)
```

```
19      if isfield(B(i),'Reflection')
20          if numel(B(i).Reflection) == 0
21              B(i).Reflection = NaN;% * ones(1,size(B(i).P,2));
22          end
23
24      end
25  end
26
27
28  threshold = 1e-3;
29
30  allRays = Ray;
31  allRays.tMax = NaN;
32  allRays.Abs = NaN;
33  allRays.Pol = '';
34  currRays = Ray;
35
36  for i = 1:nSteps
37      %Intialize the structure.
38      newRays = [];
39      newRays.R0 = 0;
40      newRays.dR0 = 0;
41      newRays.Lambda = 0;
42      newRays.Pol = '';
43
44      %tic;
45      %numel(currRays)
46      for j = 1:numel(currRays)
47          [Rj, Tj, tMax, Abs,diffR] = ...
                ray_iteration_3D(B,currRays(j),n0,0);
48          currRays(j).tMax = tMax;
49          currRays(j).Abs = Abs * norm(currRays(j).dR0);
50
51
52          if ¬isnan(tMax) %&& limits_test(Rj,Limits)
53              if norm(Rj.dR0)≥threshold
54                  newRays(end+1) = Rj;
55              end
56
57              if norm(Tj.dR0)≥threshold
58                  newRays(end+1) = Tj;
59              end
60
61              if numel(diffR) > 0
62                  for ii = 1:numel(diffR)
63                      if norm(diffR(ii).dR0)≥threshold
64                          newRays(end+1) = diffR(ii);
65                      end
66
67
68                  end
69
70
```

```
71
72              end
73
74          end
75
76      end
77
78
79
80      newRays = newRays(2:end);
81      allRays = [allRays, currRays];
82
83      if numel(newRays) ==0
84          break;
85      end
86
87      currRays = newRays;
88      %toc;
89   %plotRays(B,allRays);
90   %pause(0.3);
91  end
92
93  allRays = allRays(2:end);
94  plotRays(B,allRays);
95
96  end
97
98
99  function tf = limits_test(Ray,Limits)
100
101 tol = 1e-9;%Hardcoded parameter in 'ray_iteration' should be ...
        changed accordingly.
102 tf = 1;
103
104 xTest = abs(Ray.R0(1) - Limits(1))<tol || abs(Ray.R0(1) - ...
        Limits(2))<tol;
105 yTest = abs(Ray.R0(2) - Limits(3))<tol || abs(Ray.R0(2) - ...
        Limits(4))<tol;
106
107 if xTest || yTest
108     tf = 0;
109 end
110
111
112 end
113
114
115 function plotRays(B,Rays)
116
117
118 cmap = colormap;
119 nc = size(cmap,1);
120
```

```
121 %for j = 1:numel(B)
122 %    figure(3);plot(...
123 %        [B(j).P(1,:) B(j).P(1,1)],[B(j).P(2,:) B(j).P(2,1)],'k');
124 %    hold on;
125 %end
126 figure(3);
127 for i = 1:numel(Rays);
128     if isnan(Rays(i).Abs)
129         continue;
130     elseif norm(Rays(i).dR0) < 20e-3
131         continue;
132     end
133     X = [Rays(i).R0(1), Rays(i).R0(1) + Rays(i).tMax * ...
            Rays(i).dR0(1)];
134     Y = [Rays(i).R0(3), Rays(i).R0(3) + Rays(i).tMax * ...
            Rays(i).dR0(3)];
135     dn = 0.03;
136     nhat = [-diff(Y) diff(X)];
137     nhat = nhat / norm(nhat);
138
139     %Parameters for the arrow heads
140     arrowAngle = 15;%Deg.
141     arrowL = 5;%Length of arrow in plot units.
142
143     Mrot = @(theta) [cos(theta) -sin(theta); sin(theta) cos(theta)];
144
145     R1 = Mrot(arrowAngle*pi/180) * [-diff(X); -diff(Y)];R1 = ...
            R1/norm(R1)*arrowL;
146     R2 = Mrot(-arrowAngle*pi/180) * [-diff(X); -diff(Y)];R2 = ...
            R2/norm(R2)*arrowL;
147
148     iclr = max(1,round(norm(Rays(i).dR0) * nc));
149     rayColor = cmap(iclr,:);
150     plot(X,Y,'Color',rayColor);hold on;
151     %Now make arrowheads.
152
153     plot(X(2)+[0 R1(1)],Y(2)+[0 R1(2)],'Color',rayColor);
154     plot(X(2)+[0 R2(1)],Y(2)+[0 R2(2)],'Color',rayColor);
155
156
157 %     if Rays(i).Abs > 0
158 %         text(mean(X) + dn*nhat(1),mean(Y) + dn*nhat(2),...
159 %             sprintf('%.3f',Rays(i).Abs),'Color','g');
160 %         text(X(1) + dn*nhat(1),Y(1) + dn*nhat(2),...
161 %             sprintf('%.3f',norm(Rays(i).dR0)),'Color','k');
162 %     end
163 end
164 hold off;
165 xlabel('X');ylabel('Z');
166 drawnow;
167
168 end
```